Morten Smedsrud Wigen

4D ultrasound vector flow imaging for intraventricular flow assessment

Thesis for the degree of Philosophiae Doctor

Trondheim, January 2019

Norwegian University of Science and Technology
Faculty of Medicine
Department of Circulation and Medical Imaging

NTNU
Norwegian University of
Science and Technology

4D ultralyd *vector flow* avbildning for evaluering av blodstrøm i hjertet

Ultralyd er den mest utbredte modaliteten for evaluering av hjertefunksjon grunnet tilgjengelighet, lav kostnad og sanntidsvisning. Ekkokardiografi (ultralyd av hjertet) blir brukt for både anatomisk avbildning og målinger av blodstrøm og vevshastigheter. Konvensjonelle, Dopplerbaserte blodstrømsmålinger har iboende begrensninger blant annet ved å være avhengig av vinkelen mellom ultralydstrålen og blodstrømsretningen. Den eneste tilgjengelige metoden for tidsoppløst volumetriske vektor-målinger er i dag fasekontrast magnetisk resonansavbildning (PC-MRI), som er en tidskonsumerende og dyr modalitet med begrenset tilgjengelighet. Arbeidet i denne avhandlingen tar for seg *vector flow imaging* (VFI), som i motsetning til Dopplermetodene er en *vinkeluavhengig* metode, og demonstrere VFI for tredimensjonal (3D) ekkokardiografi.

Teknologiske fremskritt i moderne ultralydsystemer muliggjør større prosesseringsmuligheter, som har gitt nye og forbedrede avbildningsmetoder. Dette arbeidet utnytter at ultralydsystemene nå kan generere mange bildelinjer samtidig som sammen med matrisetransdusere gir tredimensjonal avbildning med høy bilderate.

Målet med denne avhandlingen var å utvikle og validere en 4D (3D+tid) VFI-metode anvendt på hjertets venstre ventrikkel, ved å utnytte mulighetene til moderne kliniske ultralydsystem. Den kliniske motivasjonen for å måle kompleks blodstrøm er å forhindre eller begrense utvikling av hjertesvikt ved å tidlig detektere patologiske endringer i strømningsmønstret i hjertet.

En tilpasset metode ble utviklet i så henseende, som en hybrid mellom konvensjonell Dopplerbasert estimering for hastighetskomponenten langs ultralydstrålen, i kombinasjon med en beregningstung mønstergjenkjenningsmetode (speckle tracking) for de to andre hastighetskomponentene. Metoden ble validert ved hjelp av datasimuleringer og et eksperimentelt oppsett på ultralydlaboratoriet, og sammenlignet med PC- MRI for en frisk frivillig. Metoden viste seg å prestere bra under gode avbildningsforhold, men er fortsatt begrenset av filtrering nødvendig for ultralydbaserte blodstrømsmålinger. I tillegg gjenstår generelle ultralydutfordringer relatert til pasient- og operatørvariabilitet. Videre valideringsstudier er derfor nødvendig for å kartlegge den kliniske nytten av metoden. Oppsummert er resultatene lovende for at ultralyd i fremtiden kan brukes som en modalitet for 4D avbildning av kompleks blodstrøm i hjertet.

Morten Smedsrud Wigen
Institutt for Sirkulasjon og Bildediagnostikk, NTNU
Hovedveileder: Lasse Løvstakken
Biveiledere: Solveig Fadnes og Hans Torp
Finansieringskilde: Norges forskningsråd

Ovennevnte avhandling er funnet verdig til å forsvares offentlig for graden Philosophiae Doctor (PhD) i medisinsk teknologi. Disputas finner sted i auditorium ØHA11, Øya Helsehus, fredag 18. januar 2019 kl 12:15.

Abstract

Ultrasound is the most used modality for cardiac assessment due to its availability, low cost and real-time display. It is widely used for both anatomical imaging and for quantification of blood flow and tissue velocities. Intracardiac blood flow measurements are, however, limited by the intrinsic properties of Doppler-based estimation. This work investigates *vector flow imaging* (VFI) which aim to resolve the angle-dependencies inherent in conventional blood flow estimation, applied in three dimensional echocardiography. The only available option today for time-resolved volumetric three-directional blood flow imaging of the heart, is phase-contrast magnetic resonance imaging (PC-MRI), which is a time demanding and expensive modality with limited accessibility.

Technological advancements in modern ultrasound systems have allowed more processing capabilities, and enabled new and improved imaging strategies. In this work, so-called multiple line acquisition and matrix-array transducers, have been technological enablers, by allowing acquisition in three dimensions and processing of high data rates.

The aim of this thesis is to develop and validate a 4D VFI method applied on the adult left ventricle, utilizing the capabilities of state-of-the-art clinical ultrasound systems. The clinical aim of measuring complex blood flow is to prevent or slow development of congestive heart failure, by early detection of pathological changes in the intraventricular flow circulation.

An adapted speckle tracking method was developed for this purpose, as a hybrid between conventional Doppler-based estimation for radial estimates, in combination with a more computational demanding block-matching approach for the lateral directional estimates. The method was validated using simulations, an *in-vitro* setup and with PC-MRI. The proposed method proved to work well under good imaging conditions, but is still limited by challenges especially related to filtering, needed for ultrasound blood flow estimation. This is in addition to general ultrasound imaging challenges related to patient and operator variability. Hence, further validation studies are needed to map the clinical utility of the method. Nonetheless, the results contained in this work was promising for ultrasound as a future modality to assess complex 4D intracardiac blood flow.

Preface

This thesis is submitted in partial fulfillment of the requirements for the degree of *Philosophiae Doctor* (Ph.D.) at the Faculty of Medicine of the Norwegian University of Science and Technology (NTNU). The research was funded by the *Norwegian Research Council*, and was carried out at the Department of Circulation and Medical Imaging. The main supervisor has been Professor Lasse Løvstakken, and co-supervisor has been Solveig Fadnes and Professor Hans Torp, all from the Department of Circulation and Medical Imaging, NTNU.

Acknowledgements

Sincere gratitude can be directed towards numerous people who have contributed in one way or another through the years I've been working on my PhD. First of all, I want to thank my supervisor, Lasse, who welcomed me at the department for my master degree project in 2012. You have the best traits a supervisor can have; knowledgeable, motivator, pragmatic and patient. I'm glad to continue our collaboration in future projects. Solveig, you have been a great supervisor and also a highly valued social contributor for me and the group during my time at the department. Also, thank you, Hans, for always being available for questions and insight, when needed.

The most important part of the daily work life the last years has been the ultrasound-group as a whole. Thank you to everyone who has contributed socially or professionally, in Trondheim and on conferences around the world. I miss being a part of your daily life at ISB, but I'm glad we're still colleagues and I look forward to continued collaborations.

Big appreciations are also directed towards friends and family, for support and interest in my work (especially curious for when I will finish my studies). Finally, Anne, you have been a key player in my life the last couple of years, keeping me motivated to both work and not to work. Coming home to you have always been a joy. Thank you so much for your love, support and patience through this period.

Table of Contents

Abbreviations and nomenclature

4D	3D + time
B-mode	Brightness mode
c_0	Speed of sound
CFI	Color flow imaging
CHF	Congestive heart failure
CW	Continuous wave
DCM	Dilated cardiomyopathy
echo-PIV	Echo particle imaging velocemitry
EL	Energy loss
$F_\#$	F-number
f_0	Pulse center frequency
fps	Frames per second
GPU	Graphical processing unit
HR	Heart rate
IIR	Infinite impulse response
IPG	Intraventricular pressure gradient
IQ	In-phase Quadrature
KE	Kinetic energy
LA	Left atrium
LV	Left ventricle
LVOT	Left ventricular outflow tract
MLA	Multiple line acquisition
M-mode	Motion mode
MV	Mitral valve
MWM	Mechanical wave mapping
PC-MRI	Phase-contrast magnetic resonance imaging
PRF	Pulse repetition frequency
PSF	Point spread function
PW	Pulsed wave
RA	Right atrium
RF	Radio frequency
RMS	Root-mean-sqaure
ROI	Region of interest
RV	Right ventricle
Rx	Receive
SAP	Sub-aperture
SNR	Signal-to-noise ratio
SSD	Sum-of-squared-differences
ST	Speckle tracking
TO	Transverse oscillations
TVI	Tissue velocity imaging
Tx	Transmit
UHFR	Ultra-high frame rate
US	Ultrasound
VD	Vector Doppler
VFI	Vector flow imaging
VFM	Vector flow mapping
V_{Nq}	Nyquist velocity

Chapter 1

Introduction

From the early demonstrations by Edler and Hertz in the mid 1950s, medical ultrasound imaging technology quickly matured to provide live images of the heart, which has revolutionized clinical cardiology. In the late 1950s, Satomura in Japan utilized the Doppler principle to detect heart valve and wall motion and, shortly after, blood motion using ultrasound [1]. Doppler echocardiography, initially using continuous wave (CW) and pulsed wave (PW) Doppler, enabled quantification of blood flow velocities using spectral analysis. Filling patterns could be characterized and valve insufficiencies detected, where also calculation of pressure drops over valves [2] was found useful for diagnosis of valvular disease. Shunts and ductus patency could also more easily be detected in fetal and pediatric cardiology. Real-time color flow imaging (CFI) was introduced on clinical systems in the mid 1980s, based on the autocorrelation method [3]. With CFI, blood velocities are visualized as a color image on top of the B-mode image, visualizing both heart anatomy and blood velocity images simultaneously. Technological advancements have further been expanding the acquisition and computation capabilities of ultrasound imaging, and today 4D (3D+time) CFI is available on state-of-the-art clinical cardiac scanners.

Using the Doppler principle for velocity estimation, however, has intrinsic limitations when imaging complex three-dimensional flow patterns. Doppler methods can only measure the velocity component along the radial direction (the direction of pulse propagation), meaning it can only tell if the blood flow is moving toward or away from the probe, not laterally (across the pulse propagation).

To resolve this issue, several vector flow imaging (VFI) methods have been proposed to also estimate lateral motion. See Fig. 1.1 for an example of intracardiac flow representation with CFI and VFI. This work proposes a 4D VFI method for cardiac applications, using a clinical ultrasound system with a matrix array probe for volumetric data acquisition. The method is based on blood speckle tracking using a high frame rate acquisition technique, and feasibility has been demonstrated to capture complex three-dimensional flow dynamics, such as vortex formation, in the adult heart from a single recording. This has not previously been demonstrated using ultrasound imaging.

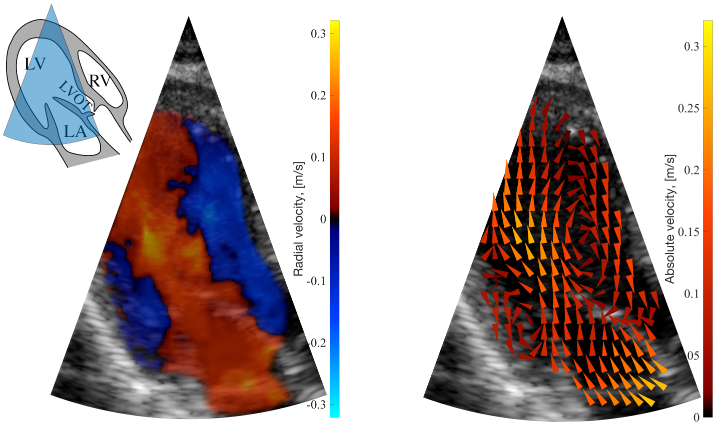

(a) Color flow imaging (b) Vector flow imaging

Figure 1.1: Comparison between conventional color flow imaging (CFI) and vector flow imaging (VFI). CFI shows radial velocities of the blood color coded with red and blue, for velocities moving toward or away from the probe. VFI is here color coded with the velocity magnitude, while the arrows represent the flow direction.

1.1 Cardiovascular blood velocity estimation using ultrasound

Standard clinical blood velocity measurements in echocardiography includes PW- and CW-Doppler, which provide spectral representation of velocities, and CFI to provide a 2D or 3D image of the mean blood velocity. Spectral analysis is conventionally calculated using the Fourier transform on the received Doppler signal. CW-Doppler transmits and receives continuously, which is beneficial when measuring very high velocities ($>\sim 2$ m/s), as no practical limit on the measurable velocity is imposed. The drawback, however, is no depth localization of the scattering source(s), as velocities from the entire illuminated sound field is acquired. PW-Doppler, however, uses range gating to estimate velocities within a limited sample volume, which consequently also gives a maximum measurable velocity without aliasing, V_{Nq}, due to the sampling of the Doppler signal at the pulse repetition frequency (PRF). For most cases PW-Doppler allows measurements of the normal velocities present in the cardiovascular system ($< 1-2$ m/s). For very high jet velocities related to pathology such as valve stenosis or leakage, CW-Doppler is typically used to quantify the peak velocities. PW- and CW-Doppler are spectral methods where manual or automatic tracing of the power spectrum is needed for velocity quantification.

CFI was developed for regional anatomic imaging of blood velocities. CFI acquires a small ensemble of consecutive Doppler signal samples at the PRF, called *packet acquisition*, from each spatial position in a region-of-interest. Further, one average velocity estimate is calculated from each ensemble or *packet*, typically using the autocorrelation method [4], resulting in a spatial map of mean velocities. Even though CFI obtains quantitative velocity estimates, the mode is mostly used for qualitative assessment, due to measurement inaccuracies, missing angle-correction, low temporal resolution and more. Despite the limited quantitative use of CFI, it is useful for detection of e.g. stenosis, abnormal flow, valve insufficiencies and turbulent jets in cardiovascular applications (heart and large vessels). Interpreting CFI images does, however, require training, as the mode cannot measure or visualize the true trajectories of the blood, only the movement towards and away from the probe. In addition, all velocities above V_{Nq} are estimated incorrectly giving aliasing artifacts in the image.

From the late 1980s new methods have been investigated to also estimate lateral blood velocities, which is now often termed vector flow imaging (VFI). Vector Doppler (VD) uses triangulation of Doppler estimates from multiple axes, either by dividing the probe aperture for multiple transmit/receive angles [5] or from multiple recordings from different views [6]. VD has mainly been demonstrated on vascular applications, where linear probes are typically used, but recently also using a high frequency matrix phased-array probe for volumetric imaging of the carotid artery [7]. Mindray ultrasounds V-flow is a VD implementation for VFI using linear probes, commercially available from 2015. Another VFI method is called transverse oscillations (TO) [8, 9], where a lateral modulation is extracted from the received signal, making it possible to use the Doppler principle also in the lateral/transverse directions. TO has mostly been applied on vascular applications, but also recently on cardiac imaging using a phased-array probe [10]. TO was made commercially available in 2012 with BK Ultrasounds VFI for vascular applications using linear probes. A third method is blood speckle tracking (BST) [11], which tracks the bloods signal-signature, called a speckle pattern, between consecutive frames, using algorithms similar to optical tracking methods, e.g. block-matching [12] and optical flow [13]. BST has been applied both on linear probes for vascular [14] and pediatric cardiac applications [15]. Based on the work carried out at NTNU, GE Vingmed Ultrasound has had a BST implementation available for pediatric cardiology, called Blood Speckle Imaging (BSI), from 2017. Echo particle imaging velocimetry (echo-PIV) [16] is a method using the same principle as for BST, however, with injected contrast agents to receive an enhanced blood signal. Echo-PIV is also less sensitive to temporal resolution as individual bubbles maintain longer correlation times than blood speckle, and has conventionally been acquired with B-mode images processed with available PIV software. Lastly, vector flow mapping (VFM) [17] is a VFI method incorporating Doppler measurements in combination with heart wall endocardial boundary to predict the true blood trajectories, on the assumption of planar flow in the imaging plane. The VFM method is clinically available on Hitatchi-Aloka scanners. A comprehensive overview of the different methods and applications is presented in the papers [18, 19].

While most of the listed methods are "old" concepts, they have benefited from possibilities of new and more powerful technology, which is why many recently have become clinically available on commercial scanners. The foundation of software beamforming in combination with high performance processors or modern GPUs, has allowed more flexible transmit/receive schemes by utilizing unfocused or defocused wave transmission with multiple line acquisition (MLA). Broad beam transmission sacrifice signal-to-noise ratio (SNR) and resolution for higher frame rates, but can also be used to increase velocity estimation quality, while maintaining a frame rate equivalent or higher to what is achieved with focused transmission. Continuous frame acquisition has also been enabled by broad beam transmission, by emitting one, or a few interleaved, beam(s) to cover an imaging sector. Continuous acquisition enables full flexibility for designing filters used to separate blood from clutter signal (clutter filtering), and a frame rate only limited by the PRF, which enables detection and measurements of rapid physiological events in the heart.

1.2 Intracardiac 4D VFI

Currently, Phase-Contrast Magnetic Resonance Imaging (PC-MRI) is the gold standard for quantitative blood flow imaging and the only modality supporting volumetric intracardiac three-directional blood velocity measurements. PC-MRI allows full flexibility of observation window, and does not have angle-dependencies as found with ultrasound. Also, no clutter filtering is needed, making it more sensitive for low velocities, compared to ultrasound. See Chapter 2 for more details regarding acquisition and estimation. PC-MRI has demonstrated clinical potential using 4D flow estimation [20], but has not yet reached routine practice. Despite unique opportunities, the modality has several drawbacks compared to ultrasound imaging, where the main downside is the acquisition time for one recording, which can last up to ~ 25 minutes for a full 4D cardiac scan [21]. Not only is this a cost-related limitation, but it can also cause loss of estimation sensitivity due to change in time-varying flow features over the acquisition time [22]. Some patients also have problems laying still for long time periods, such as claustrophobic patients and children (who often must be sedated). Availability is another limitation, by not having the imaging equipment available bedside for immobile patients e.g. after or during surgery. The price and space requirements for an ultrasound scanner is also minimal compared to an MRI scanner.

Despite numerous examples of ultrasound VFI methods, few have demonstrated to work robustly for cardiac applications, and none are bedside available for 4D imaging of the adult heart. Several factors could be the reasons for this:

- Low spatial resolution due to the limited aperture on cardiac probes.
- Low spatial resolution due to low frequencies needed for deep imaging.
- Challenging clutter filtering with presence of valve and heart wall motion.
- Restricted frame rates related to deep and volumetric imaging.
- Few available ultrasound systems for 2D-matrix array probes.

4D VFI has, however, been demonstrated for vascular imaging using a matrix-array probe [7], but only for shallow depths with higher frequencies than what is applicable for cardiac imaging. A reconstruction-based VD approach, using multiple volumetric CFI recordings from different cardiac views, has demonstrated 4D VFI on pediatric patients with congenital heart disease [6]. This could potentially also be applied on adults, but is a complex approach with many limiting factors including mismatch in view alignment, assumption of flow periodicity across multiple independent acquisitions and CFI aliasing, in addition to the above listed factors. On adult hearts an approach using echo-PIV with multiple 2D slices has been suggested, which could potentially be reconstructed to 4D VFI using an underlying physical model [23].

1.3 Clinical applications using VFI

For blood flow examination both quantitative measures, using CW- or PW-Doppler, and qualitative analysis, using CFI, are based on the Doppler principle with its intrinsic limitations. Three-directional velocity components make the measurements less[1] angle-dependent, and could hence improve already existing measurements for velocity traces and volume flow. Qualitative visualization can also be more intuitively displayed by using e.g. pathlines or streamlines [24]. From PC-MRI, and with the advent of ultrasound VFI, also new measures are investigated as potential indices for cardiac function. One example is quantification of vortex formation [25, 26], which is hypothesized to link diastolic and systolic function by preserving the kinetic energy between the phases [27]. Energy loss calculation is an alternative measure of loss of such preservation [24]. Pressure gradient measurements have been used to investigate flow mechanics during diastolic filling, where relations have been found between pressure drops and relaxation times during initialization and progression of congestive heart failure (CHF) [28]. Estimates of pressure gradients require sufficient temporal resolution, and have been demonstrated with conventional color M-mode approximations using ultrasound [29], and with special high frame rate (45 fps) acquisitions using PC-MRI [24].

Echocardiography is the most used modality for cardiac assessment, due to its availability, real-time display and low-cost. The last decade, several 2D VFI methods have been implemented on commercial scanners, making them more available, which hopefully will increase clinical research and map clinical relevance.

1.4 Aims of study

The main aim of this thesis is to demonstrate feasibility of high frame rate 4D VFI for cardiac applications without the need of contrast agents, using a high-end clinical ultrasound system and a 2D matrix phased-array transducer. This can be further divided into four subaims.

- Implement acquisition schemes suitable for 4D VFI on a clinical scanner

---

[1] The measurements should in principle have no angle dependency with three-directional estimates. However, the performance of the estimator will still depend on the beam-to-flow angle due to resolution differences in the axial and lateral directions and clutter filtering causing signal drop-outs for regions with low axial velocities.

- Develop a fast

  and accurate 3D blood velocity estimator
- Develop an *in vitro* setup for validating 4D VFI
- Provide initial *in vivo* feasibility of 4D VFI

1.5 Thesis outline

This chapter is followed by discussion in Sec. 5.4 and conclusions in Sec. 1.8. Further, Chapter 2 contains relevant background material to the subjects in the thesis. The scientific contributions included in the thesis are found in Chapters 3, 4 and 5.

1.6 Summary of contributions

The following section contains motivation and outcome of the three scientific contributions in the thesis.

1.6.1 *In vivo* Intracardiac Vector Flow Imaging Using Phased Array Transducers for Pediatric Cardiology

Vector flow imaging using speckle tracking with linear probes provides good spatial resolution compared to phased-array probes, due to higher center frequencies and larger aperture. However, the depth and field of view is limited and the probe is too large to fit between the ribs, which is why phased-array transducers are preferred in cardiology.

The work presented in this paper focused on adaption to and validation of blood speckle tracking using phased-array transducers. In addition, previously described bias effects using speckle tracking [30] were studied to find the source and solution to the problem. Simulations of straight tubes with parabolic flow at different depths were used to validate the performance of the method, revealing accurate tracking performance under good imaging conditions. As expected, the variance of the velocity estimates increased in depth and with higher steering angles. The method was tested *in vivo* for two patients; one newborn with pulmonary stenosis, and an 11-year-old with dilated cardiomyopathy. Patient recordings were made both with linear and phased-array probes for comparison.

Between 40-80 frames-per-second were achieved using plane waves with a duplex setup. Whereas fully diverging beams could have increased the frame rate further for the phased-array probes, estimation quality would have been negatively influenced by the lower signal-to-noise ratio. However, measured beam profiles showed that slightly diverging (focus located 9 cm behind transducer) would have an advantageous beam profile in depth for parallel receive beams. With phased-array compared to linear array probes, the tracking quality is reduced because of the depth-dependent resolution. Still, for the depths investigated in this paper (< 10 cm), promising *in* *vivo* results were obtained where the vector flow images revealed similar flow features such as vortex formation for both probe types. Further, independent of the probe, the proposed forward-backward tracking approach robustly canceled biases in transitional regions between blood and clutter/noise regions.

This paper has been published in IEEE Transactions on Ultrasonics, Ferroelectrics and Frequency Control (2017 Sep;64(9):1318-1326), and is presented here in its original form. The candidate was the second author for the publication, and contributed to the development of the estimation method used, including the forward-backward approach and beam profile simulations, and in addition, contributed to the drafting of the manuscript.

1.6.2 4D Intracardiac Ultrasound Vector Flow Imaging - Feasibility and Comparison to Phase-Contrast MRI

Vector flow imaging has mainly been demonstrated for 2D applications. This paper presents a methodology with the potential of making 4D VFI available from a routine ultrasound cardiac examination for the first time. A new combination of Doppler estimation and speckle tracking is used to estimate the 3D velocity vector from blood. The method was validated *in vitro*, using a rotating tissue-mimicking phantom, and compared with PC-MRI *in vivo*.

Transmission of plane waves was utilized by using a 2D matrix array probe where the insonification was distributed both in azimuth and lateral directions. Using plane waves in 3D comes at a cost of reduced SNR, compared to 2D, due to more spread of the transmitted energy, as elevational focusing is no longer applicable. Acquiring volumetric data further significantly reduces frame rate, compared to 2D scanning. To compensate for this loss, ECG-gating was utilized and resulted in a frame rate of 50 fps for the full volumetric acquisition covering a sector of $\sim 45^\circ \times 45^\circ$ to 12 cm depth. An additional thick-slice setup was developed, with an acquired volume sector of $\sim 45^\circ \times 10^\circ$, enabling through-plane velocity estimation and a continuous acquisition for retrospective PW-Doppler estimation.

The estimation method used in this work was based on the method described in Chapter 3, however, with modifications for 3D estimation. 3D kernels were here used for speckle tracking in both lateral directions, while the axial component was obtained with Color Flow measurements with added dealiasing. Exploitation of phase information for axial estimates was applied for two reasons; firstly to reduce processing time, and secondly to improve performance. The first was an important step to adapt the speckle tracking method for 3D applications. The second was to reduce the estimator variance, as using the autocorrelation method has been found beneficial to use, compared to speckle tracking, for the radial component [14].

The rotating tissue-mimicking phantom, revealed that the developed estimator could robustly measure 3D motion with velocity amplitudes in accordance with what expected from intraventricular blood flow, higher than V_{Nq}. Clutter filtering, however, causes drop-out regions where low Doppler shifts are present, or disrupted signals in regions where clutter filtering is not sufficiently suppressing conflicting signals. As seen in Chapter 3, this can give corrupted or biased velocity estimates. With lower SNR, as a consequence of using plane waves in 3D, velocity estimation is more challenging than for 2D. Despite these challenges, comparing ultrasound 4D VFI with PC-MRI revealed comparable results, with qualitative and quantitative evaluation, for healthy volunteers, under good ultrasound imaging conditions.

This paper has been accepted for publishing in IEEE Transactions on Medical Imaging (T-MI)(2018 Dec; 37(12), 2619-2629). The paper is presented here in its original form. The candidate was the main contributor to all aspects of the work, except acquisition of MRI data.

1.6.3 Ultra-high frame rate cardiac imaging for simultaneous quantification of tissue and flow velocities

The development of the thick slice acquisition setup in Chapter 4 had a greater potential than what was shown in the article. The ultra-high frame rate (UHFR) setup was in this work used to obtain both tissue and blood flow measurements from one acquisition, for both clinically established modes as well as new experimental measurements.

A conventional clinical setup was used to acquire reference data, which was compared with the same modes processed from the UHFR setup. This included blood and tissue PW-spectra, CFI, tissue velocity imaging (TVI) and color M-mode. New measurements demonstrated in the manuscript were VFI, intraventricular pressure gradients (IPG) and mechanical wave mapping (MPM).

The comparison with a default clinical setup showed similar quality between the clinical and the experimental setups, but with a frame rate only limited by the PRF for the UHFR setup. The comparison was, however, done on healthy volunteers, and can be expected to show more deviation, in the clinical setups favor, under more challenging imaging conditions, due to reduced penetration when using plane waves in 3D.

VFI data were estimated with the setup and used for both qualitative visualization of blood flow, and for IPG calculation. The latter was found to benefit from frame rates up to 100 Hz, which is lower than what earlier used with color M-mode, but higher than what is obtained with conventional CFI. MWM relied on the full time resolution available with the setup, as velocities between 2 and 10 m/s were estimated, in compliance with earlier reported findings [31].

The work presented in this manuscript was meant as a pre-clinical study, and future studies will include patients to further investigate potential couplings between tissue and flow measurements.

This paper has been submitted to IEEE Transactions on Medical Imaging, and is presented here in its current form. The candidate was the main contributor to all aspects of the work, except application to ethical committee and acquisition of data.

1.7 Discussion of results

The work carried out in this thesis initially involved the development and improvement of a speckle tracking algorithm for 2D phased-array imaging, and further the development and evaluation for 4D vector flow imaging (VFI). Several advancements of the speckle tracking estimator were developed; cancellation of spatial bias using a forward-backward tracking approach; using a depth-dependent tracking kernel due to the depth decreasing resolution with phased-array scanning; utilization of phase information for the radial velocity component. The latter was also applied to reduce processing time, which scales significantly when transition from two- to three-dimensional block matching, however, loosing computational gain as increased kernel sizes were found beneficial for dealiasing. Feasibility was demonstrated for phased-array probes in pediatric applications in 2D, as well as for 4D on adult hearts. In relation to 4D VFI, a thick slice application was developed to demonstrate VFI with a continuous acquisition, providing more flexibility during postprocessing, and an ultra-high frame rate. We showed that such an ultra-high frame rate acquisition can be beneficial for both conventional imaging modes and experimental methods, for flow and also tissue motion estimation.

Acquisition

For volumetric cardiac imaging on adults, 2D matrix phased-array probes with small footprints are the only available probe alternative, due the limited acoustic window available between the ribs. Availability of research systems with support for such probes are limited, as the number of transducer elements quickly exceed the number of channels available on most systems, and consequently complex hardware design is needed for in-probe channel reduction utilizing sub-aperture (SAP) beamforming. Through collaboration with GE Vingmed Ultrasound (Horten, Norway), a modifiable E95 scanner was at our disposal, and used in this work, with state-of-the-art technology used for 3D echocardiography. As a clinical scanner, it also supports a streamlined acquisition environment for viewing and exporting data. This was found to be an important aspect when working with cardiologists, as they could acquire data with a familiar interface and display, resulting in good quality recordings.

Expanding a 2D scanning setup to volumetric scanning reduces the effective frame rate significantly. To compensate for this large difference in frame rate, one option is to reduce the number of transmit pulses by utilizing broader transmit beams in combination with more MLAs. SAP beamforming, however, limited the receive-steering angle and hence the maximum opening angle that can be received around a given pulse direction. The acquisition setup used in the presented work was therefore restricted to plane wave transmission. While utilizing broader beams could have reduced the number of transmit pulses, image quality is negatively affected by the degree of broadness with volumetric imaging, compared to 2D imaging, due to the lack of focusing in elevation direction. For this reason, using fully diverging beams for 4D VFI acquisition might be challenging, however, with new 1024 channel systems [32–34] supporting fully connected matrix-array probes, this is can be further investigated, and has already been demonstrated for other imaging modes [35, 36] than VFI.

As for now, with limited receive-opening angles, ECG-gating was unavoidable to maintain similar frame rates as with 2D imaging. For the volumetric acquisition, 50 volumes per second was achieved with a packet size of 14, resulting in a total of 700 acquisition volumes per second. By limiting the number of scan planes in elevation to one, similar to a 2D scan, a continuous acquisition of 3500-4000 volumes per second was achieved. Having a continuous acquisition was beneficial in many ways, e.g. ultra-high frame rate to capture short-lived events, improved clutter filter flexibility for better separation of blood, tissue and noise signals, and retrospective PW-Doppler measurements from any position in the slice volume.

Blood speckle tracking

Phased-array transducers have limited flexibility for transmit/receive schemes compared to linear arrays, because of their limited aperture size. Vector Doppler (VD) using aperture separation, and transverse oscillations (TO) with bi-lobed apodization, can only be utilized by sacrificing resolution when using phased-array transducers. From previous experience in our group at NTNU, blood speckle tracking (BST) has been found compatible with clinical systems by plane wave acquisition of CFI packet data in combination with MLA for lateral tracking [37]. Velocity estimation with BST can also exceed V_{Nq}, contrary to VD and TO, but is still dependent on acquisition at PRF rate to track the blood speckle pattern, due to fast decorrelation times and for adequate clutter filtering.

An extension to 3D was implemented in this work, with MLAs in both azimuth and elevation direction. To reduce processing time, utilization of the radial phase information was applied followed by a dealiasing step, in combination with 2D lateral block-matching, rather than a full 3D block-matching approach. In addition, using the phase information for the radial estimates was also found to reduce variance. Two other improvements were applied for the BST method; forward-backward tracking to resolve estimation bias, and a resolution adapted kernel size for phased-array imaging.

However, other methods have also demonstrated feasibility using phased-array probes without contrast agents [7, 10, 17] and could potentially also be adapted to 4D cardiac VFI in the future, but these have not been investigated in this work.

Validation and measurements

The resulting 4D VFI setup used and validated in Chapter 4, proved to work well under good imaging conditions with a rotating phantom on a wide range of velocities, $0 - 1$ m/s. As expected, though, a reduction in performance in relation to depth and steering was present. This was also consistent with tube flow simulations in Chapter 3, used for validation of the 2D imaging setup. Robust validation of 4D VFI *in vivo* data is, however, more challenging. PC-MRI is currently the only available alternative, but equal flow fields can not necessarily be expected between the modalities for several reasons; differences in the actual flow fields due to independent recordings taken at different time/locations with heart rate variations; cross-modality image registration errors; PC-MRI data are acquired over > 1000 heart beats, which will cause loss of beat-to-beat variations [22]; modality dependent artifacts. Despite sources of error, comparable flow fields were obtained between the modalities, both by qualitative inspection and from quantitative measurements including velocity traces and integrated measurements (kinetic energy (KE) and energy loss (EL)). Without reference measurements, intraventricular pressure gradient (IPG) calculations were also applied on the VFI data from the thick-slice setup in Chapter 5, and showed comparable trends as from the literature [38], and in accordance with a physiological interpretation. From qualitative observations, secondary flow features could be identified and visualized, such as a large vortex formation in the central lumen and a smaller vortex behind the mitral leaflet during diastole, in addition to primary flow features during filling and ejection. Such 4D VFI images have not been previously shown using ultrasound.

The validation and acquisition of 4D VFI *in vivo* data has in this work been limited to transthoracic apical views of the heart for imaging depths of $<\sim 12$ cm. The apex view is beneficial for intracardiac blood-flow imaging as the primary velocity components are along the beam axis, making clutter filtering more efficient than for parasternal views.

Chapter 5 addresses other usage of the ultra-high frame rate (UHFR) acquisition obtained with the thick-slice acquisition than VFI imaging. Comparable quality, as with conventional clinical setups, was obtained for PW-Doppler, CFI, TVI and anatomic M-modes. The frame rates were only limited by the PRF, making detection of rapid physiological events in the heart possible, such as mechanical wave propagation. An acquisition scheme able to capture both tissue and flow dynamics has potential to be used for combined flow and tissue measurements in future work.

Challenges and future work

As demonstrated also here, accurate blood flow estimation relies heavily on sufficient removal of clutter, without sacrificing blood signal. During the cardiac cycle, presence of clutter changes with the motion of the heart valves and myocardium. Spatiotemporal adaptive clutter filtering could hence be an advantage for the method, by dynamically distinguishing blood signal from both noise and clutter. Spatiotemporal clutter filtering has shown potential in a number of applications [39], however, it has yet to prove efficient for cardiac applications. The continuous thick-slice acquisition can be a useful setup for further investigation due to its continuous frame acquisition.

Due to high estimation variance, smoothing of the velocity measurements has been a necessity to obtain useful data. In the presented work simple convolution based kernel smoothing was used. The addition of divergence free regularization, or another combination with a physical model for velocity predictions, might be an alternative approach to minimize loss of details while reconstructing the velocity field. This could be an important step for quantification of secondary flow features, as many of those measures are highly dependent on accurate velocity fields.

As the acquisition schemes developed rely on ECG-gating, patients with an unsteady heart rate or arrhythmia will be challenging to image. This could, however, be overcome by setting a valid heart rate interval to exclude irregular beats during a longer acquisition. This is used for MRI acquisitions, where also respiratory gating is used, as acquisitions last longer than what is applicable with breath holding. Respiratory gating and very long acquisition times are, however, more challenging with ultrasound due to the manual handling of the ultrasound probe. Echocardiography has other patient specific challenges, such as variable spacing between the ribs, and the need for extra imaging depths in large subjects, which may result in too poor image quality to obtain useful VFI results. While these limitations have always been present using ultrasound, VFI is more sensitive to noise and clutter than conventional Doppler-based methods. In the presented work, this has not been thoroughly validated, and patient feasibility studies are the next step towards proving the method suitable for clinical use. Contrast agents can be an alternative for extra challenging patients, which is believed to be compatible with the described setup, however, with a lower mechanical index (MI), to prevent bubble rapture. This can also possibly resolve/reduce challenges related to clutter filtering.

1.8 Concluding remarks

This thesis has focused on the technical aspects of 4D VFI, including the acquisition and estimation, but also demonstrated recent experimental measurements enabled by the technological advancements. Initial demonstration for 4D VFI has been provided, and give optimism for future directions of ultrasound as a modality for complex blood flow measurements, potentially providing a bedside alternative to what can be achieved with PC-MRI today.

1.9 List of publications

In addition to published and unpublished manuscripts included in this thesis, written and oral contributions have been made to national and international conferences. A list of the material to which the candidate has contributed is included in the following.

Papers included in the thesis

1. Solveig Fadnes, **Morten S. Wigen**, Siri Ann Nyrnes, and Lasse Løvstakken, "*In vivo* intracardiac vector flow imaging using phased array transducers for pediatric cardiology", *Published in IEEE Transactions on Ultrasonics, Ferroelectrics, and Frequency Control 64, no. 9(2017): 1318 - 1326.*

2. **Morten S. Wigen**, Solveig Fadnes, Alfonso Rodriguez-Molares, Tore Bjåstad, Marius Eriksen, Knut Haakon Stensæth, Asbjørn Støylen, and Lasse Løvstakken, "4D Intracardiac Ultrasound Vector Flow Imaging -Feasibility and Comparison to Phase-Contrast MRI", *Published in IEEE Transactions on Medical Imaging (Early Access) (2018).*

3. **Morten S. Wigen**, Solveig Fadnes, Seb, Annichen, Asbjørn Støylen, and Lasse Løvstakken, "Ultrafast imaging for simultaneous cardiac tissue and flow velocity measurements", submitted to *Submitted to IEEE Transactions on Medical Imaging(Aug. 2018).*

Conference proceedings

1. **Morten S. Wigen**, and Lasse Løvstakken, "*In vivo* three-dimensional intracardiac vector flow imaging using a 2D matrix array transducer", *Proceedings - IEEE International Ultrasonics Symposium, 2016.*
2. Jakob Høgenes, **Morten S. Wigen**, Siri Ann Nyrnes, Patrick Segers, Abigail Swillens, and Lasse Løvstakken, "Model-based estimation of intra-cardiac blood flow velocities using an unscented Kalman filter", *Proceedings - IEEE Ultrasonics Symposium, 2016.*
3. Solveig Fadnes, Siri Ann Nyrnes, **Morten S. Wigen**, Eva Tegnander, and Lasse Løvstakken, "Detailed flow visualization in fetal and neonatal hearts using 2-D speckle tracking", *Proceedings - IEEE Ultrasonics Symposium, 2016.*

Oral presentations

1. **Morten S. Wigen**, Solveig Fadnes and Lasse Løvstakken, "3D vector flow imaging", *The Artimino Conference on Medical Ultrasound Technology, Helsinborg, 2015.*
2. **Morten S. Wigen**, and Lasse Løvstakken, "*In vivo* three-dimensional intracardiac vector flow imaging using a 2D matrix array transducer", *IEEE International Ultrasonics Symposium, Tours, 2016.*
3. Jakob Høgenes, **Morten S. Wigen**, Siri Ann Nyrnes, Patrick Segers, Abigail Swillens, and Lasse Løvstakken, "Model-based estimation of intra-cardiac blood flow velocities using an unscented Kalman filter", *IEEE International Ultrasonics Symposium, Taipei, 2015.*
4. Solveig Fadnes, Siri Ann Nyrnes, **Morten S. Wigen**, Eva Tegnander, and Lasse Løvstakken, "Detailed flow visualization in fetal and neonatal hearts using 2-D speckle tracking", *IEEE International Ultrasonics Symposium, Taipei, 2015.*
5. **Morten S. Wigen**, Alfonso Rodriguez-Molares, Tore Bjåstad, Marius Eriksen, Knut Haakon Stensæth, and Lasse Løvstakken, "In-Vivo 3D Cardiac Vector Flow Imaging âĂŞ a Comparison Between Ultrasound and Phase-Contrast MRI", *IEEE International Ultrasonics Symposium, Tours, 2016.*
6. **Morten S. Wigen**, Alfonso Rodriguez-Molares, Tore B,åstad, Marius Eriksen, Knut Haakon Stensæth, and Lasse Løvstakken, "IIn-Vivo 3D Cardiac Vector Flow Imaging âĂŞ a Comparison Between Ultrasound and Phase-Contrast MRI", *IEEE International Ultrasonics Symposium, Washington D.C., 2017.*

7. **Morten S. Wigen**, and Lasse Løvstakken, “4D cardiac vector flow imaging”, *The Artimino Conference on Medical Ultrasound Technology, Artimino, 2017.*
8. Solveig Fadnes, **Morten S. Wigen**, Thomas Grø nli, Siri Ann Nynes, and Lasse Løvstakken, “Cardiac vector flow imaging”, *Myocardial Velocity & Deformation Imaging, Leuven, 2017.*

Poster presentations

1. **Morten S. Wigen**, Jakob Høgenes, Joris Cauwenberge, Sten Roar Snare, Patrick Segers, Solveig Fadnes, Abigail Swillens, Lasse Løvstakken ”High frame rate 3D blood speckle tracking of intracardiac flow”, *IEEE International Ultrasonics Symposium, Taipei, 2015.*

References

[1] I. Edler and K. Lindström, “The history of echocardiography,” *Ultrasound in Medicine and Biology*, vol. 30, no. 12, pp. 1565–1644, 2004.

[2] L. Hatle, A. Brubakk, A. Tromsdal, and B. Angelsen, “Noninvasive assessment of pressure drop in mitral stenosis by Doppler ultrasound.,” *Heart*, vol. 40, no. 2, pp. 131–140, 1978.

[3] R. Omoto, R. Omoto, Y. Yokote, S. Takamoto, S. Kyo, K. Ueda, H. Asano, K. Namekawa, C. Kasai, Y. Kondo, and A. Koyano, “The development of Real-Time Two-Dimensional Doppler Echocardiography and Its Clinical Significance in Acquired Valvular Diseases,” *Japanese Heart Journal*, no. April 1983, pp. 325–340, 1984.

[4] C. Kasai, K. Namekawa, A. Koyano, and R. Omoto, “Real-Time Two-Dimensional Blood Flow Imaging Using an Autocorrelation Technique,” *IEEE Transactions on Sonics and Ultrasonics*, vol. 32, no. 3, pp. 458–464, 1985.

[5] B. Dunmire, K. W. Beach, K. H. Labs, M. Plett, and D. E. Strandness, “Cross-beam vector Doppler ultrasound for angle-independent velocity measurements,” *Ultrasound in Medicine and Biology*, vol. 26, no. 8, pp. 1213–1235, 2000.

[6] A. Gomez, A. De Vecchi, M. Jantsch, W. Shi, K. Pushparajah, J. M. Simpson, N. P. Smith, D. Rueckert, T. Schaeffter, G. P. Penney, A. de Vecchi, M. Jantsch, W. Shi, K. Pushparajah, J. M. Simpson, N. P. Smith, D. Rueckert, T. Schaeffter, and G. P. Penney, “4D Blood Flow Reconstruction Over the Entire Ventricle From Wall Motion and Blood Velocity Derived From Ultrasound Data,” *IEEE Transactions on Medical Imaging*, vol. 34, no. 11, pp. 2298–2308, 2015.

[7] M. Correia, J. Provost, M. Tanter, and M. Pernot, “4D ultrafast ultrasound flow imaging: In vivo quantification of arterial volumetric flow rate in a single heartbeat,” *Physics in Medicine and Biology*, vol. 61, no. 23, pp. L48–L61, 2016.

[8] M. Anderson, “Spatial quadrature: a novel technique for multi-dimensional velocity estimation,” *1997 IEEE Ultrasonics Symposium Proceedings. An International Symposium (Cat. No.97CH36118)*, vol. 2, pp. 1233–1238, 1997.

[9] J. A. Jensen and P. Munk, “A new method for estimation of velocity vectors,” *IEEE Transactions on Ultrasonics, Ferroelectrics, and Frequency Control*, vol. 45, no. 3, pp. 837–851, 1998.

[10] S. Holbek, K. L. Hansen, N. Fogh, R. Moshavegh, J. B. Olesen, M. B. Nielsen, and J. A. Jensen, “Real-time 2-D Phased Array Vector Flow Imaging,” *IEEE Transactions on Ultrasonics, Ferroelectrics, and Frequency Control*, vol. 65, no. 7, pp. 1205–1213, 2018.

[11] L. N. Bohs, B. J. Geiman, M. E. Anderson, S. C. Gebhart, and G. E. Trahey, “Speckle tracking for multi-dimensional flow estimation,” *Ultrasonics*, vol. 38, no. 1-8, pp. 369–375, 2000.

[12] A. Barjatya, “Block Matching Algorithms For Motion Estimation,” *IEEE Transactions Evolution Computation*, vol. 8, no. 3, pp. 225–229, 2004.

[13] D. Patel and U. Saurahb, “Optical flow measurement using Lucas Kanade method,” *Int J Comput Appl*, vol. 61, no. 10, pp. 6–10, 2013.

[14] S. Fadnes, I. K. Ekroll, S. A. Nyrnes, H. Torp, and L. Lovstakken, “Robust angle-independent blood velocity estimation based on dual-angle plane wave imaging,” *IEEE Transactions on Ultrasonics, Ferroelectrics, and Frequency Control*, vol. 62, no. 10, pp. 1757–1767, 2015.

[15] S. Fadnes, S. A. Nyrnes, H. Torp, and L. Lovstakken, “Shunt Flow Evaluation in Congenital Heart Disease Based on Two-Dimensional Speckle Tracking.,” *Ultrasound in medicine {&} biology*, vol. 40, no. 10, pp. 1–13, 2014.

[16] H. B. Kim, J. R. Hertzberg, and R. Shandas, “Development and validation of echo PIV,” *Experiments in Fluids*, vol. 36, no. 3, pp. 455–462, 2004.

[17] K. C. Assi, E. Gay, C. Chnafa, S. Mendez, F. Nicoud, J. F. Abascal, P. Lantelme, F. Tournoux, and D. Garcia, “Intraventricular vector flow mapping - A Doppler-based regularized problem with automatic model selection,” *Physics in Medicine and Biology*, vol. 62, no. 17, pp. 7131–7147, 2017.

[18] J. Jensen, S. Nikolov, A. C. H. Yu, and D. Garcia, “Ultrasound Vector Flow Imaging: II: Parallel Systems,” *IEEE Transactions on Ultrasonics, Ferroelectrics, and Frequency Control*, vol. 3010, no. c, pp. 1–1, 2016.

[19] J. A. Jensen, S. I. Nikolov, A. C. Yu, and D. Garcia, “Ultrasound Vector Flow Imaging-Part II: Parallel Systems,” *IEEE Transactions on Ultrasonics, Ferroelectrics, and Frequency Control*, vol. 63, no. 11, pp. 1722–1732, 2016.

[20] P. Dyverfeldt, M. Bissell, A. J. Barker, A. F. Bolger, C.-J. Carlhäll, T. Ebbers, C. J. Francios, A. Frydrychowicz, J. Geiger, D. Giese, M. D. Hope, P. J. Kilner, S. Kozerke, S. Myerson, S. Neubauer, O. Wieben, and M. Markl, “4D flow cardiovascular magnetic resonance consensus statement,” *Journal of Cardiovascular Magnetic Resonance*, vol. 17, no. 1, p. 72, 2015.

[21] M. Markl, A. Frydrychowicz, S. Kozerke, M. Hope, and O. Wieben, “4D Flow MRI,” vol. 1036, pp. 1015–1036, 2012.

[22] C. Chnafa, S. Mendez, and F. Nicoud, “Image-Based Simulations Show Important Flow Fluctuations in a Normal Left Ventricle: What Could be the Implications?,” *Annals of Biomedical Engineering*, vol. 44, no. 11, pp. 3346–3358, 2016.

[23] A. Falahatpisheh, G. Pedrizzetti, and A. Kheradvar, “Three-dimensional reconstruction of cardiac flows based on multi-planar velocity fields,” *Experiments in Fluids*, vol. 55, no. 11, 2014.

[24] P. P. Sengupta, G. Pedrizzetti, P. J. Kilner, A. Kheradvar, T. Ebbers, G. Tonti, A. G. Fraser, and J. Narula, “Emerging trends in CV flow visualization,” *JACC Cardiovasc Imaging*, vol. 5, no. 3, pp. 305–316, 2012.

[25] J. Faurie, M. Baudet, K. C. Assi, D. Auger, G. Gilbert, F. Tournoux, and D. Garcia, “Intracardiac Vortex dynamics by high-frame-rate doppler vortography-in vivo comparison with vector flow mapping and 4-d flow mri,” *IEEE Transactions on Ultrasonics, Ferroelectrics, and Frequency Control*, vol. 64, no. 2, pp. 424–432, 2017.

[26] G. R. Hong, G. Pedrizzetti, G. Tonti, P. Li, Z. Wei, J. K. Kim, A. Baweja, S. Liu, N. Chung, H. Houle, J. Narula, and M. A. Vannan, “Characterization and quantification of vortex flow in the human left ventricle by contrast echocardiography using vector particle image velocimetry,” *JACC Cardiovasc Imaging*, vol. 1, no. 6, pp. 705–717, 2008.

[27] P. J. Kilner, G.-Z. Yang, A. John Wilkes, R. H. Mohiaddin, D. N. Firmin, and M. H. Yacoub, “Asymmetric redirection of Âŕow through the heart,” *NATURE www.nature.com*, vol. 404, no. 13, pp. 759–761, 2000.

[28] M. Ohno, C. P. Cheng, and W. C. Little, “Mechanism of altered patterns of left ventricular filling during the development of congestive heart failure,” *Circulation*, vol. 89, no. 5, pp. 2241–2250, 1994.

[29] M. J. Garcia, J. D. Thomas, and A. L. Klein, “New doppler echocardiographic applications for the study of diastolic function,” *Journal of the American College of Cardiology*, vol. 32, no. 4, pp. 865–875, 1998.

[30] J. Van Cauwenberge, L. Lovstakken, S. Fadnes, A. Rodriguez-Molares, J. Vierendeels, P. Segers, and A. Swillens, “Assessing the performance of ultrafast vector flow imaging in the neonatal heart via multiphysics modeling and in-vitro experiments,” *IEEE Transactions on Ultrasonics, Ferroelectrics, and Frequency Control*, vol. 3010, no. c, pp. 1–1, 2016.

[31] H. Kanai, “Propagation of Vibration Caused by Electrical Excitation in the Normal Human Heart,” *Ultrasound in Medicine and Biology*, vol. 35, no. 6, pp. 936–948, 2009.

[32] A. Ortega, D. Lines, J. Pedrosa, B. Chakraborty, V. Komini, H. Gassert, and J. D'Hooge, "HD-PULSE: High channel Density Programmable ULtrasound System based on consumer Electronics," *2015 IEEE International Ultrasonics Symposium, IUS 2015*, pp. 31–33, 2015.

[33] J. A. Jensen, H. Holten-Lund, R. T. Nilsson, M. Hansen, U. D. Larsen, R. P. Domsten, B. G. Tomov, M. B. Stuart, S. I. Nikolov, M. J. Pihl, Y. Du, J. H. Rasmussen, and M. F. Rasmussen, "SARUS: A synthetic aperture real-time ultrasound system," *IEEE Transactions on Ultrasonics, Ferroelectrics, and Frequency Control*, vol. 60, no. 9, pp. 1838–1852, 2013.

[34] J. Provost, C. Papadacci, J. E. Arango, M. Imbault, M. Fink, J. L. Gennisson, M. Tanter, and M. Pernot, "3D ultrafast ultrasound imaging in vivo," *Physics in Medicine and Biology*, vol. 59, no. 19, pp. L1–L13, 2014.

[35] B. F. Osmanski, D. Maresca, E. Messas, M. Tanter, and M. Pernot, "Transthoracic ultrafast Doppler imaging of human left ventricular hemodynamic function," *IEEE Transactions on Ultrasonics, Ferroelectrics, and Frequency Control*, vol. 61, no. 8, pp. 1268–1275, 2014.

[36] C. Papadacci, M. Pernot, M. Couade, M. Fink, and M. Tanter, "High-contrast ultrafast imaging of the heart," *IEEE Transactions on Ultrasonics, Ferroelectrics, and Frequency Control*, vol. 61, no. 2, pp. 288–301, 2014.

[37] L. Lovstakken, S. A. Nyrnes, B. O. Haugen, and H. Torp, "Angle-independent quantification of complex flow patterns in congenital heart disease," in *Ultrasonics Symposium (IUS), 2011 IEEE International*, pp. 1246–1249, 2011.

[38] R. B. Thompson and E. R. McVeigh, "Fast measurement of intracardiac pressure differences with 2D breath-hold phase-contrast MRI," *Magnetic Resonance in Medicine*, vol. 49, no. 6, pp. 1056–1066, 2003.

[39] C. Demené, T. Deffieux, M. Pernot, B. F. Osmanski, V. Biran, J. L. Gennisson, L. A. Sieu, A. Bergel, S. Franqui, J. M. Correas, I. Cohen, O. Baud, and M. Tanter, "Spatiotemporal Clutter Filtering of Ultrafast Ultrasound Data Highly Increases Doppler and fUltrasound Sensitivity," *IEEE Transactions on Medical Imaging*, vol. 34, no. 11, pp. 2271–2285, 2015.

Chapter 2

Background

Ultrasound is characterized as sound waves with frequencies higher than what is audible for the human ear. While echo location has been used by animals, as bats and dolphins, for presumably millions of years for orientation and detecting prey, it was first in 1917 that the first technological ultrasound device was invented by Paul Langevin for detection of submarines. The technology is today used in a number of fields; seabed mapping and fish detection with sonar, oil and gas pipe inspection, proximity sensors in autonomous vehicles, medical imaging and much more.

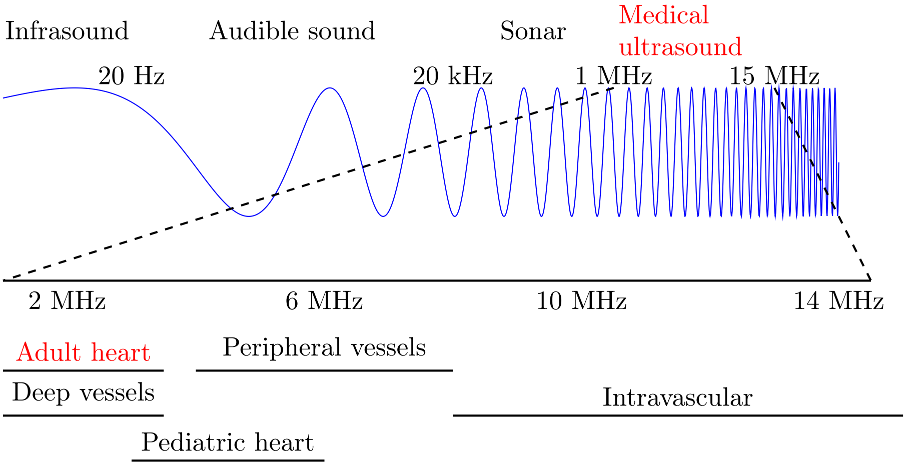

Figure 2.1: Acoustic frequency spectrum. Ultrasound frequencies for Doppler measurements below

As a medical imaging modality, ultrasound is considered safe within the power levels defined by the FDA/IEC, and is a cheap and available equipment compared to many other modalities such as MRI, X-ray, CT and PET, which are either/or time consuming, invasive, uses ionizing radiation, non-portable or expensive. The applications for medical ultrasound covers a great variety of fields including cardiology, gynecology, obstetrics, breast, vascular, musculoskeletal, brain and more. This thesis is related to echocardiography, which involves ultrasound imaging of the heart.

The following chapter covers principles for understanding the basics of ultrasound imaging, with emphasis on concepts relevant to the thesis.

2.1 Acoustic wave propagation and reflection

Piezoelectricity is used in most ultrasound transducers to produce sound waves, by utilizing certain material's ability to convert electric charge to mechanical deformation, and vice versa. By stimulating such piezo elements with an alternating electric field, mechanical waves are produced. The frequency of these waves are between $\sim 1-15$ MHz for most medical applications, see Fig. 2.1 for frequencies used for Doppler imaging applications [1]. Higher frequencies are beneficial for resolution, but are also attenuated faster than low frequency waves as they propagate in a medium. Higher frequencies are hence used for shallow depths, while low frequencies for deep imaging.

Acoustic waves propagate at the speed of sound, c_0, which is determined by the density and compressibility in the medium. Further, reflections of the transmitted wave will be produced if these mechanical properties change in the propagation direction. With a known speed of sound and by timing the transmitted wave, the distance, d, to the reflector/scatterer is known by the relation

$$d = \frac{c_o \cdot t}{2} \tag{2.1}$$

where t is the time from transmission to reception. In soft tissue in the body the speed of sound is approximately $c_o = 1540\frac{m}{s}$. The two-way travel time to a desired imaging depth, defines the minimum time before a new pulse can be emitted. The rate between successive transmit events is called the pulse repetition frequency (PRF), where

$$PRF_{max} = \frac{c_o}{2 \cdot d_{max}} \tag{2.2}$$

2.2 Ultrasound imaging

Today, an array of piezo elements are used on most medical ultrasound probes, where two main probe categories are used for cardiovascular applications. Linear probes shifts a subset of its active elements in the azimuth direction of the probe to build up an image line-by-line in a horizontal direction, while phased-array probes have a smaller aperture size and scans a region by utilizing delays the individual elements to steer the transmitted beam in a desired direction, and obtains an image with spherical coordinates. Matrix array probes have a 2D array of elements for steering in both azimuth and elevation direction for volumetric scanning. Fig. 2.2 illustrates these two scan-types, and also two different scanning modes. Motion mode (M-mode) obtains a spatiotemporal image by scanning in only one direction over time, and is useful to examine movement and thickness variation over time with high temporal resolution. Brightness mode (B-mode) utilizes spatial scanning, as described above, to obtain a cine-loop of images. B-mode can also be obtained with 3D scanning for volume rendering or flexible arbitrary slicing.

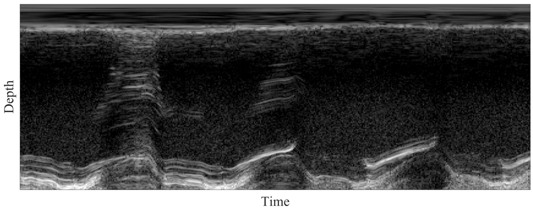

(a) Motion mode (M-mode) of the hearts basal wall movement

(b) Linear scan - with brightness mode (B-mode) of common carotid artery

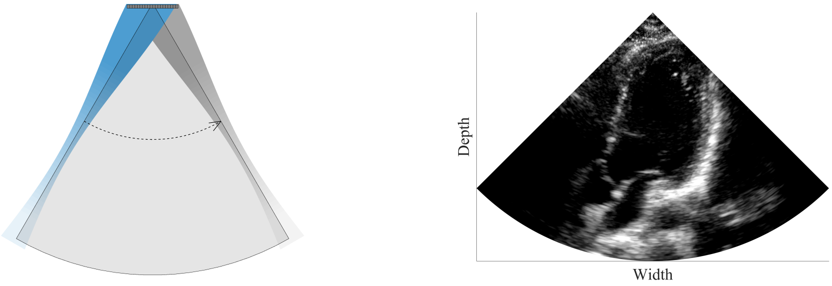

(c) Sector scan - with B-mode of a long axis view of the left ventricle

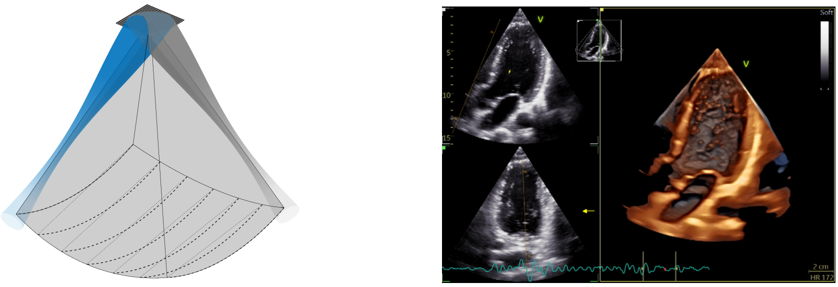

(d) Volumetric sector scan - with 3D rendering to the right-most image, with two corresponding orthogonal slices

Figure 2.2: Cardiovascular imaging modes

2.2.1 Resolution, focusing and beamforming

The spatial resolution in an ultrasound image is defined by the three-dimensional point spread function (PSF). The radial resolution is effectively half the received pulse length, while the lateral resolutions are decided by the aperture widths (D), focus depth (F) and receive center frequency (f_0) of the received signal, according to

$$D_f \propto \frac{c_0 F}{f_0 D} \tag{2.3}$$

The two-way transmit/receive resolution becomes

$$D_{f,txrx} \propto \frac{c_0}{f_0(\frac{D_{tx}}{F_{tx}} + \frac{D_{rx}}{F_{rx}})} \tag{2.4}$$

A fine spatial resolution increases the image quality, but also require denser sampling and hence more scan lines for an image, which decreases the frame rate. Transmit focusing and steering can be manipulated by applying timed delays on the individual transducer elements, see Fig. 2.3a. To increase frame rate, broad beam transmission can be utilized in combination with multiple line acquisition (MLA), where multiple receive lines are constructed in parallel for each transmit shot, see Fig. 2.4.

Receive beamforming is conventionally achieved by the delay-and-sum method by calculating the time of arrival from a point in the imaging sector to each probe element, which are coherently summed, see Fig. 2.3b. For 1D array probes (used for 2D imaging) beamforming is processed in the front-end on the ultrasound scanner (moved to the back-end with the advent of software beamforming), by wiring each element as separate channels through the probe cable. The number of elements used in a 2D matrix array probe(used for 3D imaging), however, exceeds the number of channels on most systems. Sub-aperture (SAP) beamforming (also called pre beamforming) is then applied in special purpose electronics in the probe to reduce the number of channels from the probe to the scanner. Further, conventional beamforming is applied on the scanner from the reduced number of channels. A consequence of using SAPs is a limitation on the maximum steering angle for a given transmit direction, when using MLAs, to avoid grating lobes. This is due to the increased effective pitch between the SAP elements as seen from the system side [2].

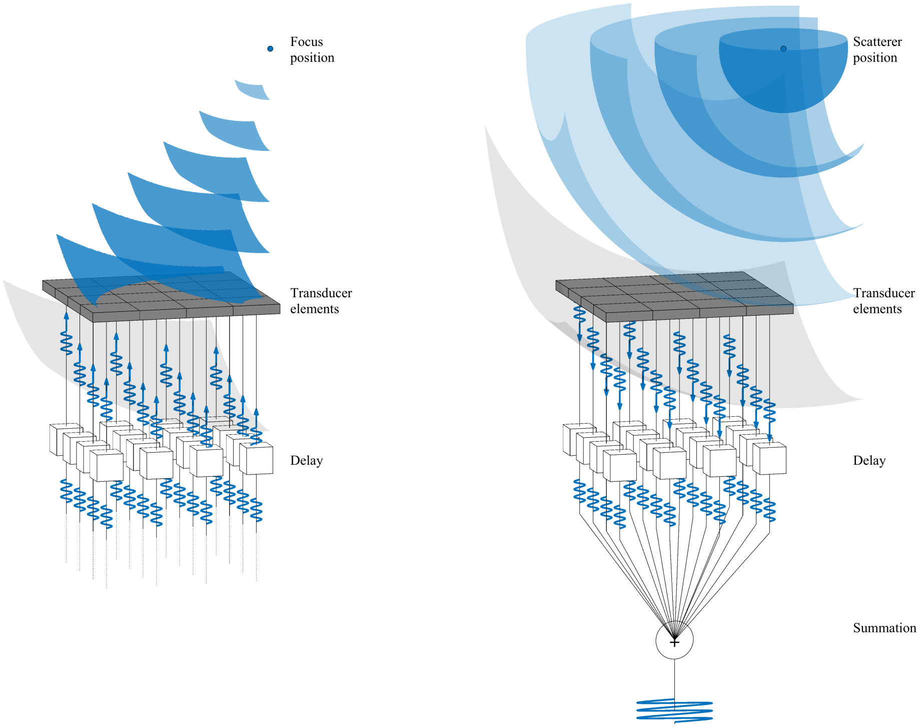

(a) Transmit beamforming (b) Receive beamforming

Figure 2.3: Beamforming for transmission (left) and reception (right) are achieved by applying delays on the individual transducer elements.

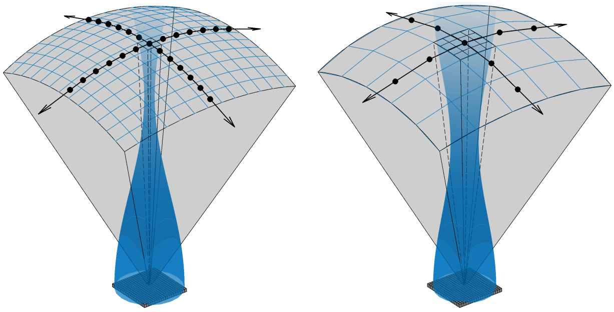

(a) Focused (b) Unfocused with MLA

Figure 2.4: Illustration of transmit focusing. Focused transmission (left) resulting in many transmit direction for a fully acquired volume. Unfocused transmission (right) in combination with MLAs (black grid) needs fewer transmit directions to cover the imaging volume, and achieves higher frame rates.

2.3 Ultrasound Doppler imaging

The Doppler effect is a fundamental principle utilized for both motion estimation and blood detection with ultrasound, and describes the phenomenon where the observed frequency is different between a moving object and an observer. As ultrasound is based on frequency modulated wave transmission, the received frequency will be changed if a scatterer is in motion relative to the probe. Further, a frequency shift, f_D can be related to the object's velocity, by

$$f_D = \frac{2f_0}{c_0} \cdot V cos\theta \tag{2.5}$$

where V is the scatterers velocity and θ is the angle between the velocity direction and the ultrasound beam axis. From the equation it follows that Doppler velocity measurements are angle dependent, which is an inherent property of the method.

According to the Nyquist-Shannon theorem, representing a signals frequency content requires sampling at least two times the highest frequency in a signal. This is relevant for range gated velocity estimation as sampling is limited by the PRF. The Nyquist velocity, V_{Nq}, is the highest measurable Doppler velocity without aliasing and is defined as

$$V_{Nq} = \frac{c_0 \cdot PRF}{4f_0} \tag{2.6}$$

2.3.1 Clutter filtering

Clutter is unwanted signal components from multiple-reflections, off-axis sources and noise. Due to the weak scattering from blood, compared to tissue, signals from blood scatters are dominated by clutter, see Fig. 2.5. Conventionally, clutter filtering is a high-pass filter approach, which attenuates signal from sources of low-velocities. Consequently, blood velocities below the filter cut-off will be attenuated, and are referred to as drop-out regions. In echocardiography, clutter filtering is challenging due to heart wall and valve motion, which make signal separation of blood and tissue difficult [3].

There are four main approaches for blood clutter filtering. Finite impulse response (FIR) filters, infinite impulse response (IIR) filters, polynomial regression filters (polyreg) and singular-value decomposition (SVD) filters, also called eigen-based filters. The three first filters are frequency based filters, and can be characterized by their frequency respons, where several factors affect the choice of filter-type, such as stop-, transition- and pass-band characteristics, phase-linearity, cut-off flexibility, initialization time and also whether the filter is time-variant/invariant [4]. With conventional color flow imaging (described in next section), a limited number of samples are available for velocity estimation, which reduces the flexibility for filter design and making polyreg and FIR filters of low order frequently used. IIR filters can also be used for short ensembles sizes, but depend on initialization [3]. IIR filters (e.g. Butterworth) are more commonly used with continuous data acquisition where the initialization period can be discarded. SVD filters are another category of filters, which attempt to recognize blood from the orthogonal basis of a decomposed raw signal [5], rather than on the frequency shift directly. These filters have recently showed increased efficiency with the use of ultra-high frame rates [6], not yet however, applied for intraventricular blood flow estimation.

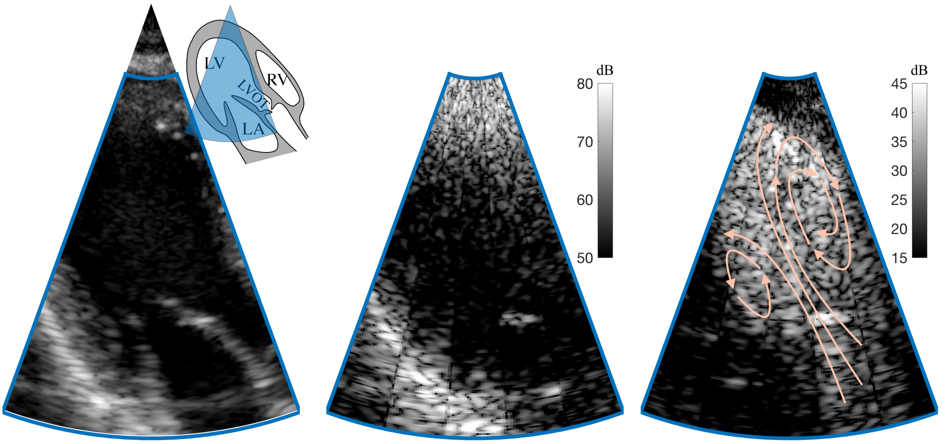

(a) Reference B-mode

(b) Raw IQ

(c) Filtered IQ revealing blood speckle

Figure 2.5: Raw image data as used for speckle tracking seen before(center) and after(right) clutter filtering. Corresponding B-mode image to the left.

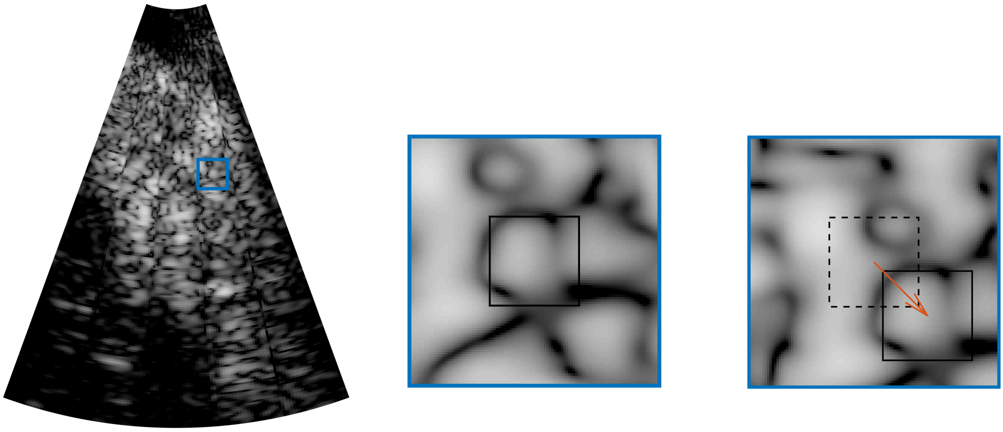

(a) Blood speckle after applied clutter filtering.

(b) Time frame 1

(c) Time frame 2

Figure 2.6: Illustration of speckle tracking based on block-matching. Search region for one velocity estimate in blue. Tracking Kernel in black. The estimated shift corresponding to best match is represented by red arrow.

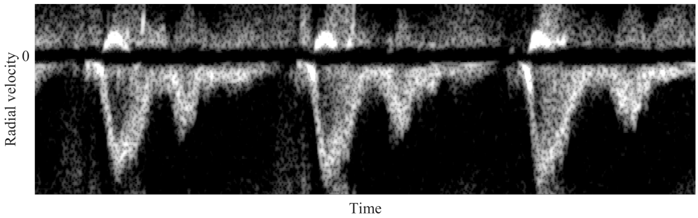

(a) PW-Doppler spectrum from the mitral valve

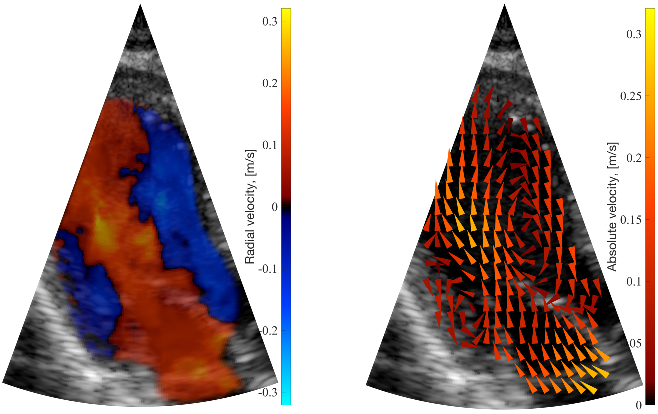

(b) Color flow imaging

(c) Vector flow imaging

Figure 2.7: Blood flow velocity modes

2.3.2 Conventional ultrasound blood flow imaging

There are multiple imaging modes for Doppler velocity measurements. Continuous wave (CW) and pulsed wave (PW) Doppler are both spectrum representations of velocities, see Fig. 2.7a. For CW-Doppler the probe aperture is divided in two, where one side is continuously transmitting and the other continuously receiving, resulting in a V_{Nq} only limited by the sampling rate of the analogue-to-digital converters. The consequence is depth ambiguities as all velocities along the imaging line are included in the spectrum. PW-Doppler, however, acquires a range gated sample volume, and will hence have a V_{Nq} limited by the PRF.

Doppler spectrum methods does not give regional information, which is why color flow imaging (CFI) was developed to image blood flow velocities over a spatial region, see Fig. 2.7b. To achieve this, a short ensemble of samples ($\sim 8 - 16$) are acquired consecutively from each image pixel to estimate the mean Doppler shift. Clutter filtering is important for sufficient attenuation of clutter to avoid underestimation.

In addition to be an angle dependent method, several factors cause artifacts in CFI [7], e.g. aliasing caused be a limited V_{Nq}, overmuch or insufficient clutter filtering. For this reason, experience is important for interpretation of CFI.

2.3.3 Vector flow imaging

To resolve the angle dependency of CFI, and for some of the methods enable velocities estimation above the V_{Nq}, multiple vector flow imaging (VFI) methods have been proposed to estimate also lateral blood motion, see Fig. 2.7c. They can be categorized into the five principles listed under. See papers [8, 9] for a comprehensive overview.

- Vector Doppler (VD) [10, 11]: Estimates a Doppler estimate from multiple directions, and performs triangulation to form two or three dimensional velocity estimates. This can be achieved by splitting up the transmit or receive aperture, or by imaging from multiple directions.

- Transverse oscillations (TO) [12, 13]: Constructs lateral modulation on the received signal to utilize the Doppler principle also laterally. This can be constructed by applying a bi-lobed apodization function on the received signal or in spatial frequency domain.

- Speckle tracking (ST) [14–16]: Blood signal has a coherent speckle signature, which follow the blood motion. By using pattern matching techniques, velocity estimation can be applied for every pixel in the image, for instance by using methods such as block matching and optical flow. This is the principle used for VFI in this work, and is illustrated in Fig. 2.6.

- Vector flow mapping (VFM) [17, 18]: Incorporation of heart wall motion together with blood Doppler measurements, the VFM method estimates the lateral blood motion in 2D, by assuming planar flow and mass conservation (zero divergence).

- Echo particle image velocemitry (echo-PIV) [19, 20]: Similar to speckle tracking, echo-PIV methods track the blood signal between frames, however, with injected contrast agents for enhanced blood signal. Due to longer correlation times with contrast agents, lower frame rates can be used for tracking, and has conventionally been achieved with B-mode acquisition.

2.4 Phase-contrast magnetic resonance imaging

For medical applications, magnetic resonance imaging (MRI) utilizes the bodies proton content(in the Hydrogen nucleus) to obtain signal, and local variations and conditions for contrast. With phase-contrast MRI (PC-MRI), however, a bipolar magnetic gradient is applied to obtain contrast from motion in the gradient direction, see Fig. 2.8. Similar to the Doppler principle, only one velocity direction can be measured at a time. In contrast to ultrasound, however, MRI has no view limitation, and these gradients can be applied in arbitrary directions to obtain three orthogonal velocity components, with e.g. the four-point method [21, 22]. The magnitude and duration of the gradient affects sensitivity to flow with low and high velocities, and is adjusted with the velocity encoding parameter, V_{enc}, which becomes the highest measurable velocity without aliasing. An image is constructed with PC-MRI in the same way as with MRI, by building up k-space, where each image line is acquired per echo time (TE), and each sequence of consecutive echoes is repeated at the rate defined by the repetition time (TR). TE and TR are affected by the imaging mediums physical properties and traded off between acquisition time and SNR. For time resolved 3D imaging, specialized sequences are used to reduce acquisition time, but a full recording can still take 30 minutes. When imaging moving objects (e.g. the heart) ECG-gating is needed to retrospectively or prospectively collect data from separated time segments of the cardiac cycles. The distinct recordings from each time segment is further combined to construct an image frame/volume. However, due to patient movement or beat-to-beat variations averaging effects can occur [23].

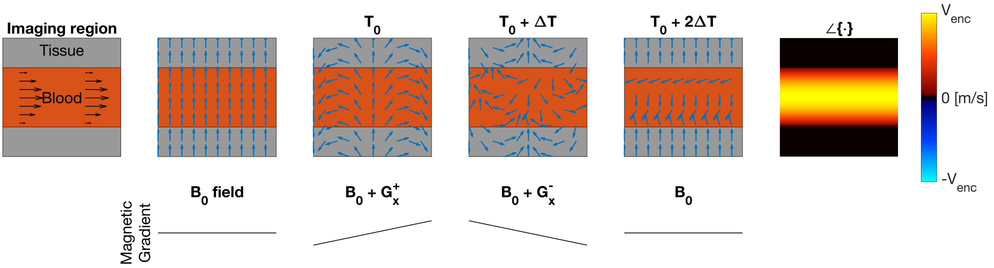

Figure 2.8: Simplified illustration of phase-contrast MRI for one velocity direction. A bipolar gradient, G^+ followed by G^-, is applied to obtain a phase deviation within voxels with moving substance, which can be related to velocities in the gradient direction. For 4D PC-MRI multiple consecutive bipolar gradients are applied for each velocity encoding direction.

2.5 Heart anatomy and the cardiac cycle

The heart is the main driving force for the bloods circulation in the body and has two basic functions; redistributing oxygenated blood from the lungs to the body, and redistributing deoxygenated blood from the body to the lungs. For these functions the heart is divided in a left and a right section, respectively, where each section has a ventricle and an atrium, see Fig. 2.9 for a schematic representation. The atrium's functions are to receive blood entering the heart and pump it into its respective ventricle, where the ventricle function is to pump blood out from the heart. These mechanisms works in synchronicity throughout the cardiac cycle, separated into two parts, systole and diastole, associated with ejection and filling of blood, respectively. Fig. 2.10 shows PW-spectra of the blood flow through the aortic outlet and the mitral valve in the left ventricle, and tissue velocities in the basal heart wall. The systolic phase is initiated by isovolumetric muscle contraction causing an increased intraventricular pressure. When the pressure in the left ventricle exceeds the aortic pressure the aortic valve opens, causing blood ejection through the aorta and contraction of the heart. This can be seen as high negative blood flow velocities in the PW-spectrum at the aortic outlet, and positive velocities in the basal heart wall as the intraventricular volume is reduced. This is followed by relaxation of the myocardium, causing the aortic valve to close, ending of the systolic phase and initiation of the diastolic phase. Rapid inflow, through the mitral valve, happens as the pressure drops in the left ventricle to a level below the left atrium. The first filling of the diastolic phase is called the e-wave, and is seen in both the PW-spectra of the mitral inlet and tissue wall, showing blood flowing into the left ventricle with a positive Doppler shift, and a negative shift of the basal wall enlarging the ventricle volume. Later, in the end of the diastolic phase, a secondary filling is triggered by atrial contraction, called the a-wave, before the cycle repeats.

During the last decade, the interaction between blood flow and heart wall mechanics has gained interest and attention, with emphasis on vortex formation in the left ventricle, enabled by PC-MRI measurements [24–27], but also using echo-PIV [28–30] and VFM [31, 32]. The main vortex in the left ventricle is believed to preserve kinetic energy between diastolic and systolic phase, by maintaing and redirection of flow momentum towards the LVOT after filling. A disturbed vortex is further hypothesized to potentially cause higher load on the heart for it to maintain cardiac output, which can lead to ventricular remodeling [29, 33]. Reasons for disturbances in the flow can be caused by changes in geometry, muscle stiffness, the vascular load, blood pressure, heart valve disorders, or changes in electromechanical activation. Much of the current knowledge in this field are still research questions, and a complete understanding of both function and pathophysiology is yet to be established.

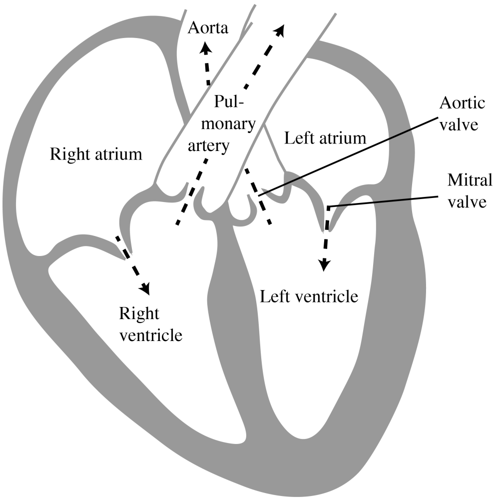

Figure 2.9: Schematic illustration of the human heart, showing the heart's four chambers and the two outlets, the aorta and the pulmonary artery, supplying the lungs and the body with oxygenated and deoxygenated blood, respectively.

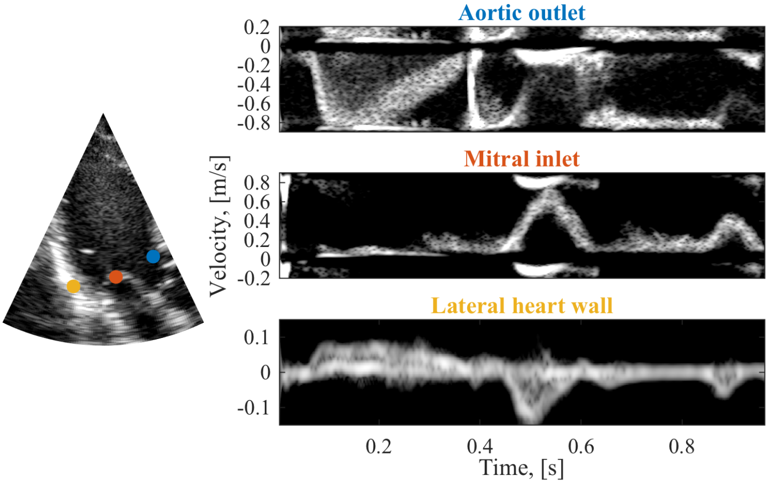

Figure 2.10: Events in the cardiac cycle, as seen with PW-Doppler spectrums of the respective positions.

References

[1] B. Angelsen and H. Torp, "Principles of medical ultrasound imaging and measurements," in *Ultrasound Imaging Vol.1*, 2000.

[2] P. Santos, G. Haugen, L. Løvstakken, E. Samset, and J. D'hooge, "Diverging Wave Volumetric Imaging Using Subaperture Beamforming," *Ultrason. Ferroelectr. Freq. Control. IEEE Trans.*, vol. 63, no. 12, pp. 2114–2124, 2016.

[3] S. Bjaerum, H. Torp, and K. Kirstoffersen, "Clutter filter design for ultrasound color flow imaging," *Ieee Transactions on Ultrasonics Ferroelectrics and Frequency Control*, vol. 49, no. 2, pp. 204–216, 2002.

[4] S. Fadnes, S. Bjaerum, H. Torp, and L. Lovstakken, "Clutter filtering influence on blood velocity estimation using speckle tracking," 2015.

[5] A. Yu and L. Lovstakken, "Eigen-Based Clutter Filter Design for Ultrasound Color Flow Imaging: A Review," *Ieee Transactions on Ultrasonics Ferroelectrics and Frequency Control*, vol. 57, no. 5, pp. 1096–1111, 2010.

[6] J. Baranger, B. Arnal, F. Perren, O. Baud, M. Tanter, and C. Demene, "Adaptive Spatiotemporal SVD Clutter Filtering for Ultrafast Doppler Imaging Using Similarity of Spatial Singular Vectors," *IEEE Transactions on Medical Imaging*, vol. 37, no. 7, pp. 1574–1586, 2018.

[7] M. a. Pozniak, J. a. Zagzebski, and K. a. Scanlan, "Spectral and color Doppler artifacts.," *Radiographics : a review publication of the Radiological Society of North America, Inc*, vol. 12, no. 1, pp. 35–44, 1992.

[8] J. Jensen, S. Nikolov, A. C. H. Yu, and D. Garcia, "Ultrasound Vector Flow Imaging: II: Parallel Systems," *IEEE Transactions on Ultrasonics, Ferroelectrics, and Frequency Control*, vol. 3010, no. c, pp. 1–1, 2016.

[9] J. A. Jensen, S. I. Nikolov, A. C. Yu, and D. Garcia, "Ultrasound Vector Flow Imaging-Part II: Parallel Systems," *IEEE Transactions on Ultrasonics, Ferroelectrics, and Frequency Control*, vol. 63, no. 11, pp. 1722–1732, 2016.

[10] B. Dunmire, K. W. Beach, K. H. Labs, M. Plett, and D. E. Strandness, "Cross-beam vector Doppler ultrasound for angle-independent velocity measurements," *Ultrasound in Medicine and Biology*, vol. 26, no. 8, pp. 1213–1235, 2000.

[11] M. Correia, J. Provost, M. Tanter, and M. Pernot, “4D ultrafast ultrasound flow imaging: In vivo quantification of arterial volumetric flow rate in a single heartbeat,” *Physics in Medicine and Biology*, vol. 61, no. 23, pp. L48–L61, 2016.

[12] J. A. Jensen and P. Munk, “A new method for estimation of velocity vectors,” *IEEE Transactions on Ultrasonics, Ferroelectrics, and Frequency Control*, vol. 45, no. 3, pp. 837–851, 1998.

[13] S. Holbek, K. L. Hansen, N. Fogh, R. Moshavegh, J. B. Olesen, M. B. Nielsen, and J. A. Jensen, “Real-time 2-D Phased Array Vector Flow Imaging,” *IEEE Transactions on Ultrasonics, Ferroelectrics, and Frequency Control*, vol. 65, no. 7, pp. 1205–1213, 2018.

[14] L. N. Bohs, B. J. Geiman, M. E. Anderson, S. C. Gebhart, and G. E. Trahey, “Speckle tracking for multi-dimensional flow estimation,” *Ultrasonics*, vol. 38, no. 1-8, pp. 369–375, 2000.

[15] H. Takahashi, H. Hasegawa, and H. Kanai, “Echo speckle imaging of blood particles with high-frame-rate echocardiography,” *Japanese Journal of Applied Physics*, vol. 53, no. 7 SPEC. ISSUE, pp. 1–7, 2014.

[16] S. Fadnes, S. A. Nyrnes, H. Torp, and L. Lovstakken, “Shunt Flow Evaluation in Congenital Heart Disease Based on Two-Dimensional Speckle Tracking.,” *Ultrasound in medicine {&} biology*, vol. 40, no. 10, pp. 1–13, 2014.

[17] D. Garcia, J. C. del Álamo, D. Tanné, R. Yotti, C. Cortina, É. Bertrand, J. C. Antoranz, E. Pérez-David, R. Rieu, F. Fernández-Avilés, and J. Bermejo, “Two-Dimensional Intraventricular Flow Mapping by Digital Processing Conventional Color-Doppler Echocardiography Images,” *IEEE Transactions on Medical Imaging*, vol. 29, pp. 1701–1713, oct 2010.

[18] K. C. Assi, E. Gay, C. Chnafa, S. Mendez, F. Nicoud, J. F. Abascal, P. Lantelme, F. Tournoux, and D. Garcia, “Intraventricular vector flow mapping - A Doppler-based regularized problem with automatic model selection,” *Physics in Medicine and Biology*, vol. 62, no. 17, pp. 7131–7147, 2017.

[19] H. B. Kim, J. R. Hertzberg, and R. Shandas, “Development and validation of echo PIV,” *Experiments in Fluids*, vol. 36, no. 3, pp. 455–462, 2004.

[20] G. R. Hong, G. Pedrizzetti, G. Tonti, P. Li, Z. Wei, J. K. Kim, A. Baweja, S. Liu, N. Chung, H. Houle, J. Narula, and M. A. Vannan, “Characterization and Quantification of Vortex Flow in the Human Left Ventricle by Contrast Echocardiography Using Vector Particle Image Velocimetry,” *JACC: Cardiovascular Imaging*, vol. 1, no. 6, pp. 705–717, 2008.

[21] M. Markl, A. Frydrychowicz, S. Kozerke, M. Hope, and O. Wieben, “4D Flow MRI,” vol. 1036, pp. 1015–1036, 2012.

[22] P. Dyverfeldt, M. Bissell, A. J. Barker, A. F. Bolger, C.-J. Carlhäll, T. Ebbers, C. J. Francios, A. Frydrychowicz, J. Geiger, D. Giese, M. D. Hope, P. J. Kilner, S. Kozerke, S. Myerson, S. Neubauer, O. Wieben, and M. Markl, "4D flow cardiovascular magnetic resonance consensus statement," *Journal of Cardiovascular Magnetic Resonance*, vol. 17, no. 1, p. 72, 2015.

[23] C. Chnafa, S. Mendez, and F. Nicoud, "Image-Based Simulations Show Important Flow Fluctuations in a Normal Left Ventricle: What Could be the Implications?," *Annals of Biomedical Engineering*, vol. 44, no. 11, pp. 3346–3358, 2016.

[24] M. Kanski, P. M. Arvidsson, J. Töger, R. Borgquist, E. Heiberg, M. Carlsson, and H. Arheden, "Left ventricular fluid kinetic energy time curves in heart failure from cardiovascular magnetic resonance 4D flow data," *Journal of Cardiovascular Magnetic Resonance*, vol. 17, no. 1, pp. 1–10, 2015.

[25] J. Eriksson, A. F. Bolger, T. Ebbers, and C. Carlhäll, "Assessment of left ventricular hemodynamic forces in healthy subjects and patients with dilated cardiomyopathy using 4D flow MRI," *Physiological Reports*, vol. 4, no. 3, p. e12685, 2016.

[26] P. M. Arvidsson, S. J. Kovács, J. Töger, R. Borgquist, E. Heiberg, M. Carlsson, and H. Arheden, "Vortex ring behavior provides the epigenetic blueprint for the human heart," *Scientific Reports*, vol. 6, pp. 1–9, 2016.

[27] M. S. Elbaz, R. J. van der Geest, E. E. Calkoen, A. de Roos, B. P. Lelieveldt, A. A. Roest, and J. J. Westenberg, "Assessment of viscous energy loss and the association with three-dimensional vortex ring formation in left ventricular inflow: In vivo evaluation using four-dimensional flow MRI," *Magnetic Resonance in Medicine*, vol. 77, no. 2, pp. 794–805, 2017.

[28] A. Kheradvar, R. Assadi, A. Falahatpisheh, and P. P. Sengupta, "Assessment of transmitral vortex formation in patients with diastolic dysfunction," *Journal of the American Society of Echocardiography*, vol. 25, no. 2, pp. 220–227, 2012.

[29] G. Pedrizzetti, G. La Canna, O. Alfieri, and G. Tonti, "The vortexâĂŤan early predictor of cardiovascular outcome?," *Nature Reviews Cardiology*, vol. 11, no. 9, pp. 545–553, 2014.

[30] I. C. Kim, G. R. Hong, G. Pedrizzetti, C. Y. Shim, S. M. Kang, and N. Chung, "Usefulness of Left Ventricular Vortex Flow Analysis for Predicting Clinical Outcomes in Patients with Chronic Heart Failure: A Quantitative Vorticity Imaging Study Using Contrast Echocardiography," *Ultrasound in Medicine and Biology*, no. July, 2018.

[31] H. Zhang, J. Zhang, X. Zhu, L. Chen, L. Liu, Y. Duan, M. Yu, X. Zhou, T. Zhu, M. Zhu, and H. Li, "The left ventricular intracavitary vortex during the isovolumic contraction period as detected by vector flow mapping," *Echocardiography*, vol. 29, no. 5, pp. 579–587, 2012.

[32] D. R. Muñoz, J. L. M. Mur, C. Fernández-Golfín, D. C. B. Filho, A. G. Gõmez, S. F. Santos, C. L. Rivera, L. M. R. Díaz, E. C. Rojo, and J. L. Z. Gõmez, "Left ventricular vortices as observed by vector flow mapping: Main determinants and their relation to left ventricular filling," *Echocardiography*, vol. 32, no. 1, pp. 96–105, 2015.

[33] M. Dal Ferro, D. Stolfo, V. De Paris, P. Lesizza, R. Korcova, D. Collia, G. Tonti, G. Sinagra, and G. Pedrizzetti, "Cardiac fluid dynamics meets deformation imaging," *Cardiovascular Ultrasound*, vol. 16, no. 1, pp. 1–10, 2018.

Chapter 3

In vivo Intracardiac Vector Flow Imaging Using Phased Array Transducers for Pediatric Cardiology

Solveig Fadnes[1], Morten Smedsrud Wigen[1], Siri Ann Nyrnes[1,2],
and Lasse Løvstakken[1]
[1] Dept. of Circulation and Medical Imaging, NTNU, Norway
[2] Dept. of Pediatrics, St. Olav's University Hospital, Trondheim, Norway

Two-dimensional blood speckle tracking (ST) has shown promise for measuring complex flow patterns in neonatal hearts using linear arrays and high-frame-rate plane wave imaging. For general pediatric applications, however, the need for phased array probes emerges due to the limited intercostal acoustic window available. In this work, a clinically approved real-time duplex imaging setup with phased array probes was used to investigate the potential of blood speckle tracking for 2-D vector flow imaging of children with congenital heart disease.
To investigate transmit beam pattern and tracking accuracy, straight tubes with parabolic flow were simulated at three depths (4.5, 7 and 9.5 cm). Due to the small aperture available, diffraction effects could be observed when approaching 10 cm, which limited the number of parallel receive beams that could be utilized. Moving to (slightly) diverging beams was shown to solve this issue at the expense of a loss in signal-to-noise ratio.
To achieve consistent estimates, a forward-backward tracking scheme was introduced to avoid measurement bias occurring due to tracking kernel averaging artifacts at flow domain boundaries.
Promising results were observed for depths $< \mathbf{10}$ cm in two pediatric patients, where complex cardiac flow patterns could be estimated and visualized. As a loss in penetration compared to color flow imaging is expected, a larger clinical study is needed to establish the clinical feasibility of this approach.

3.1 Introduction

In pediatric cardiology, ultrasound Doppler imaging is a highly useful tool for detecting abnormal blood flow patterns related to pathology. Abnormalities or diseases of the heart have a prevalence of 8 out of 1000 live births [1]. Intracardiac flow in pediatric patients with congenital heart disease can be complex due to septal defects, valvular abnormalities, arterial or venous anomalies, and hypoplastic, hypertrophic or dilated cardiac chambers. Further, surgical treatment may lead to changes in flow that is not fully mapped or understood, and which may be related to both short and long term outcomes.

Color flow imaging (CFI) is the conventional method to measure blood flow velocity patterns in a 2- or 3-D region, where velocities are color-coded and visualized together with the B-mode image. For blood velocity quantification, spectral Doppler methods are commonly used where the full spectrum of blood velocities from a specific point or line in the ultrasound image is displayed. However, these Doppler-based methods only measure the blood velocity component along the ultrasound beam axis and cannot capture the 3-D nature of the blood flow. Interpretation of the color flow images is thus required to comprehend the true flow patterns, which is challenging for complex (secondary) flow patterns. These limitations may lead to missed or false diagnoses [2, 3]. Methods for improved blood velocity estimation, quantification and visualization in 2- or 3-D would decrease the need of interpretation when evaluating the cardiac anatomy and function, and could potentially introduce new clinical markers for diagnosis and follow up [4].

One approach to obtain the 2-D or 3-D vector flow information is to utilize blood speckle tracking (ST), where the movement of the blood speckle is tracked from frame to frame, providing an estimate of the blood velocity vector [5]. When combined with high-frame-rate imaging techniques such as plane wave imaging, it was shown in [6] that angle-independent cardiac blood velocity information could be achieved using a linear array probe. Using a linear array probe for cardiac applications is first of all feasible when imaging newborns. However, the pediatric patient group includes a broad spectrum of patients from the smallest premature baby up to adult size. Thus, for pediatric cardiology in general, phased array probes are today the preferred standard probes to image through the intercostal space. Feasibility for 2-D vector flow maps from phased array imaging has previously been shown for simulations and experimental setup of a newborn heart model [7], and *in vivo* in adults [8]. In both cases non-compounded diverging beams and blood speckle tracking was used.

While imaging using broad transmit and parallel receive beams can benefit from a much higher frame rate than conventional focused imaging, the loss in signal-to-noise ratio (SNR) and penetration depth can be a limiting factor, leading to a trade-off with frame rate. Sufficient removal of the strong tissue echo is also more challenging, due to the increased side-lobe and clutter level compared to focused imaging. Further, the small aperture of phased array probes may influence the accuracy of the speckle tracking velocity estimates, due to diffraction focusing effects and the depth-dependent image resolution. To increase SNR and improve blood velocity estimation, contrast agents can be injected into the patient's bloodstream and tracked as in echo-PIV [4, 9, 10]. Contrast agents are, however, neither desired in a daily routine examination nor currently approved in pediatric cardiology.

Our aim in this study was to develop and investigate blood speckle tracking methods based on phased array imaging for pediatric cardiology without the use of contrast agents. A clinically approved imaging setup was implemented for phased array probes, utilizing broad pulses to acquire real-time color flow data at high data acquisition rates, as also described in [11]. Two pediatric patients (one newborn and one 11-year-old) were included in the study. To investigate the possible penetration depths with our clinically approved setup, the pressure fields for unfocused, deeply focused and defocused (diverging) waves were measured in a water-tank setup. In addition, the accuracy of the velocity estimator as a function of depth and steering angles was also investigated in simulated straight tubes with parabolic flow.

3.2 Methods

3.2.1 *In vivo* acquisition

A real-time duplex imaging setup based on broad transmit pulses was set up on a GE Vivid E9 scanner with a dedicated research software (GE Vingmed, Horten, Norway). For the color flow acquisition the transmit pulses were deeply focused (30 cm) to insonify a broad sector for each transmit, and a multi-line acquisition (MLA) with 16 parallel receive beams was used. This both increases overall frame rate, and also enables speckle tracking on a large coherent region acquired at the Doppler pulse repetition frequency (PRF). Fully plane (unfocused) or diverging (negative focus) transmissions were not available for clinical testing. The acquisition was clinically approved for the GE 9L linear array probe and two phased array pediatric probes (GE 6S and 12S). With 16 parallel receive lines per transmit beam, several (3-9) transmissions were needed to get the desired region-of-interest (ROI). For the B-mode images, conventional focused transmit beams were used to obtain sufficient image quality. The resulting duplex frame rate was 40-80 frames-per-second (fps), depending on the Doppler packet size (8-22), image depth (<10 cm) and ROI width.

IQ-data from the color flow acquisition were stored after real-time beamforming on the scanner. The data were further processed off-line to generate vector flow maps of the blood flow as described in Sec. 3.2.5. The imaging sequences were clinically approved before the study started and were within the guidelines from the US Food and Drug Administration (FDA). The image acquisition parameters for the *in vivo* recordings are listed in Table 3.1.

Two patients were imaged using both the 9L linear array and the 6S phased array probe. Patient 1 was born with a pulmonary valve (PV) stenosis and was 10 days old and weighed 3080 g at the time of the ultrasound recordings. Patient 2 was 11 years old (35.6 kg and 149.8 cm tall) at the time of the recordings. This patient had a dilated cardiomyopathy (DCM) of unknown cause and an ejection fraction of only 20%. Written informed consents were obtained from the parents of the children before examination and the study was approved by the Norwegian Regional Committee for Medical and Health Research Ethics.

3.2.2 Straight tube simulations

To investigate the accuracy of the velocity estimator using the clinically approved *in vivo* setup, Field II [12, 13] was used to simulate a parabolic straight tube flow for an

Table 3.1: *In vivo* acquisition parameters

Patient 1 (PV stenosis)	9L	6S
Pulse center frequency [MHz]	5	4.5
PRF [kHz]	10	9
Packet size	16	22
V_{Nyquist} [m/s]	0.82	0.77
No. of tx beams	7	5
Tracking kernel size [mm^2]	1x1	
Spatial Gaussian smoothing [mm^2]	5x5	
Temporal smoothing [ms]	40	

Patient 2 (DCM)	9L	6S
Pulse center frequency [MHz]	4.5	3.7
PRF [kHz]	6	5
Packet size	8	16
V_{Nyquist} [m/s]	0.51	0.53
No. of tx beams	12	8
Tracking kernel size [mm^2]	1.5x1.5	
Spatial Gaussian smoothing [mm^2]	7x7	
Temporal smoothing [ms]	40	

imaging sequence with 7 deeply focused (30 cm) transmit pulses covering an opening angle of 60°, using a similar pediatric phased array probe. The pulse center frequency was 3.3 MHz, the PRF was 3 kHz and the Doppler packet size was 16. The straight tubes were horizontally placed at three depths (4.5, 7 and 9.5 cm) and had a constant parabolic flow with a maximum velocity of 1 m/s. To evaluate the expected mean and standard deviation of the velocity estimator, 20 realizations of the Doppler frame were simulated. Both accuracy as a function of depth and steering angle was investigated. The simulation parameters are listed in Table 3.2.

While the deeply focused setup was used due to approved safety measurements, it could be beneficial with deeper or slightly diverging beams to maintain a wide and more uniform beam at deeper distances. The straight tube simulations were further used to simulate speckle patterns under the different acquisition schemes, followed by a speckle tracking performance comparison.

3.2.3 Beam profile measurements

The Onda AIMS III scanning system (Onda Corporation, USA) was used with the Onda HMB-0200 membrane hydrophone to measure pressure fields for the GE 6S probe. The clinically approved setup with a deep (30cm) focus was compared with fully unfocused and diverging beams. These transmit beam profiles were used to investigate

Table 3.2: Straight tube simulation parameters

Transducer type	Phased array
Aperture size [cm]	1.44
Azimuth focus [cm]	-9, 30
Elevation focus [cm]	5
Pulse center frequency [MHz]	3.3
No. of tx beams	1, 7
PRF [kHz]	3
Packet size	16
No. of frames	20
SNR	30
Straight tube radius [cm]	0.75
Straight tube tilt [°]	0
Straight tube depths [cm]	4.5, 7, 9.5
Straight tube $V_{\max}$ [m/s]	1
Tracking kernel size [mm^2]	1x1

the beam width and uniformity versus depth, as well as the relative penetration. Further, the receive beam sampling can be seen relative to beam profile uniformity. No transmit or receive apodization was used. For all sequences the surface temperature was the limiting factor, and the same aperture, and thus also transmit voltage, was used for all cases.

3.2.4 Clutter filtering

The IQ packet data from the *in vivo* color flow acquisitions were high-pass filtered to attenuate the strong clutter signal before blood velocity estimation. For speckle tracking velocity estimation, time-invariant clutter filters are preferred to avoid speckle image decorrelation due to the filter itself. However, for increasing packet sizes (> 16) polynomial regression filters may also be used as the decorrelation becomes negligible [14]. In this work, a 4th order finite-impulse-response (FIR) filter with -3 dB cut-off velocity of $v_{co} = 1/3 \cdot V_{\text{Nyquist}}$ was used for packet sizes 8-16. For packet size 22, a 5th order polynomial regression filter could be utilized (-3 dB cut-off velocity of $v_{co} = 0.22 \cdot V_{\text{Nyquist}}$).

3.2.5 Blood speckle tracking

In blood speckle tracking, the correlation between speckle and blood movement is utilized to obtain an angle-independent velocity estimate of the blood velocity [5]. Pattern matching techniques on the radio frequency (RF) or envelope data are used to find the speckle displacement from frame to frame, where normalized cross correlation (NXC) is commonly used as a reference. There are, however, alternative speed enhancing alternatives such as sum-of-squared-differences (SSD) and sum-of-absolute-differences (SAD) giving similar results [5, 14]. Spatial interpolation before tracking may be needed to obtain the desired velocity resolution, depending on the original sampling grid. Tracking on RF data generally has a better accuracy in the axial direction than envelope tracking, as the phase information is taken into account, however, the high sampling rate needed for the RF data quickly increases the amount of data which must be processed.

In our pursue for a real-time implementation, a GPU-optimized speckle tracking algorithm was developed. IQ data from the color flow acquisition in our duplex setup were first linearly interpolated laterally using a constant variance output grid [15]. Hardware accelerated linear interpolation on the GPU was used to further increase our velocity resolution without increasing the memory load. SSD was used as the pattern matching method on the envelope data between subsequent frames in the Doppler packet. The resulting SSD matrices were averaged over the Doppler packet and the minimum in the averaged SSD matrix determined the initial blood speckle displacement. Parabolic sub-sample fitting on the each estimates' SSD matrix gave the final non-discrete velocity estimate. The GPU implementation is running close to real-time on commodity hardware.

3.2.6 Forward-backward tracking

As reported in the literature [7, 16], artifacts can occur using speckle tracking in the transition between signals with different characteristics, i.e. velocity gradients, blood-to-noise, blood-to-clutter. The artifacts are observed as bias either towards or away from these regions. To overcome this, a forward-backward tracking approach is introduced. Where forward tracking (FT) finds the best match for a spatial region from one frame to the next in time and backward tracking (BT) finds the best match from the second frame to the previous, the forward-backward tracking (FBT) is the average of the FT and the BT estimates. The concept is that the FT and BT estimates can both contain a bias, but in opposite directions, which cancels out when averaged. The cost of the method is the processing time which is almost doubled per tracking point.

A general expression for the sum-of-squared-differences at the given coordinates u,v, can be written as follows,x

$$\begin{aligned} SSD(u,v,n,\Delta_{\text{lag}}) = \sum_{x,y} (&IQ_{\text{env}}(x,y,n) - \\ &IQ_{\text{env}}(x+u,y+v,n+\Delta_{\text{lag}}))^2, \end{aligned} \tag{3.1}$$

where IQ_{env} is the envelope of an IQ data frame, with a packet acquisition represented in the last dimension. The sum over x and y represents the spatial region of a search kernel. Further, the FT and BT methods are given by

$$SSD_{\text{FT}}(u,v) = \frac{1}{N-1}\sum_{i=0}^{N-2} SSD(u,v,i,1) \tag{3.2}$$

$$SSD_{\mathrm{BT}}(u,v) = \frac{1}{N-1}\sum_{i=0}^{N-2} SSD(u,v,i+1,-1), \tag{3.3}$$

where the conventional FT method uses the positive lag and the BT changes the reference frame with the search frame. The SSD matrices are averaged over the packet size, N.

The position of the minimum of the SSD functions relative to the center is used as the expected discrete shift, as described in 3.4 where * denotes either FT or BT.

$$[\Delta_{*x}, \Delta_{*z}] = \mathrm{argmin}_{u,v}(SSD_*) \tag{3.4}$$

To further get the sub-pixel shift, parabolic minimum fitting of the SSD function is used for each dimension separately. Equation 3.5 describes the procedure where the SSD index is relative to the found minimum from 3.4 in the direction of the sub-pixel shift to calculate.

$$\delta_* = \frac{SSD_*(-1) - SSD_*(+1)}{2(SSD_*(-1) - 2SSD_*(0) + SSD_*(+1))} \tag{3.5}$$

The final velocity estimates for FT and BT are given by 3.6, and for the FBT method by 3.7. Note the negative sign in 3.6 for BT.

$$\begin{aligned} \vec{V}_{\mathrm{FT}} &= \frac{[\Delta_{\mathrm{FT}x} + \delta_{\mathrm{FT}x}, \Delta_{FTz} + \delta_{\mathrm{FT}z}]}{\mathrm{PRF}} \\ \vec{V}_{\mathrm{BT}} &= -\frac{[\Delta_{\mathrm{BT}x} + \delta_{\mathrm{BT}x}, \Delta_{\mathrm{BT}z} + \delta_{\mathrm{BT}z}]}{\mathrm{PRF}} \end{aligned} \tag{3.6}$$

$$\vec{V}_{\mathrm{FBT}} = (\vec{V}_{\mathrm{FT}} + \vec{V}_{\mathrm{BT}})/2; \tag{3.7}$$

The raw tracking estimates can have high variance, in particular the lateral velocity component. Spatial and temporal smoothing is utilized to lower variance for better impression of the flow fields. See details in Table 3.1.

3.3 Results

3.3.1 Forward-backward tracking

Investigations of the forward-backward tracking method were done for two simplified simulation setups. The simulated data were generated using the FUSK simulation tool [17], which assumes a spatially invariant point-spread-function (PSF), but simulates realistic IQ-data very rapidly. Results are shown in Fig. 3.1 and 3.2. Fig. 3.1 shows simulated moving blood signal at 50 cm/s with a weak, close to stationary, neighboring signal at 0.1 cm/s. The slowly-moving signal is dominated by noise after clutter filtering. Fig. 3.2 shows the same signals, however with a lower SNR and a stronger stationary signal resulting in a stationary region dominated by decorrelation due to clutter filtration and the conflicting signals. The specifics are found in Table 3.3 and Fig. 3.3. An observation from both results is the transitional region between the

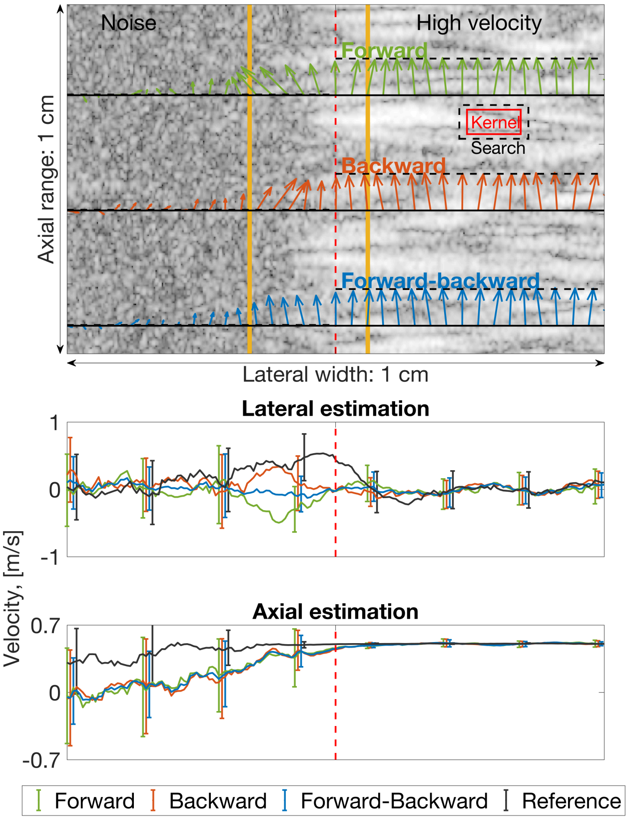

Figure 3.1: Tracking performance under a simulated noise-to-flow condition. The lower panels show the estimated velocities mean and standard deviation in the lateral direction for the lateral and axial components respectively. A bias towards noise is observed outside the flow region for the forward tracking estimates.

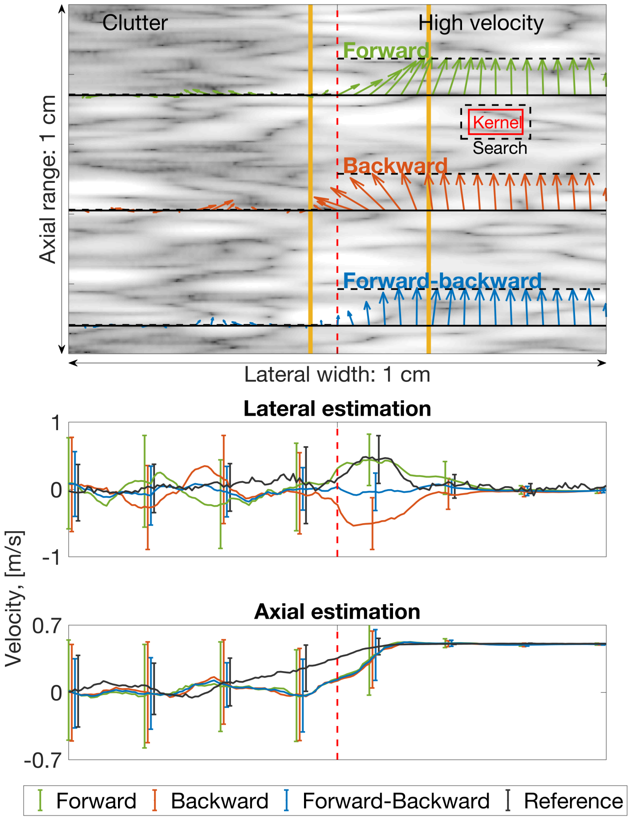

Figure 3.2: Tracking performance under a simulated clutter-to-flow condition. The lower panels show the estimated velocities mean and standard deviation in the lateral direction for the lateral and axial components respectively. A bias towards flow is observed inside the flow region for the forward tracking estimates.

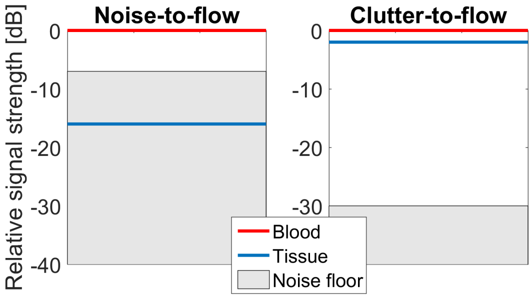

Figure 3.3: Relative signal strengths after clutter filtering for the two scenarios.

Table 3.3: FUSK simulations, forward-backward tracking.

Flow RMSE (x/z), [cm/s]	Noise-to-flow	Clutter-to-flow
Forward tracking	27.4/4.39	33.1/19.0
Backward tracking	26.1/4.77	34.9/18.6
Forw.-back. tracking	22.6/3.82	17.6/17.6
Reference tracking	31.2/0.95	33.2/6.53

signals, due to the PSF and the tracking kernel, resulting in a gradual change in the tracking estimates from one region to the other. In both cases we observe an opposite lateral bias in the separated forward and backward estimates and a magnitude bias on the axial component. The extent of the bias depends on the scenario, but in both cases the FBT approach significantly reduces the error. In the noise and flow signal scenario, Fig. 3.1, the bias is first observed outside the signal border, where we see a gradual bias towards the noise. We still see an improvement of the estimates inside the flow region with a decrease of 17% and 13% in RMS-error, compared to FT, for the lateral and axial components respectively. For the clutter and flow signal scenario, the bias occurs also inside the flow-region. In this case the FBT approach reduced the RMS-error with 47% and 6.6% for the two components respectively. For comparison, the tracking was also done using RF-data and normalized cross correlation as a reference. The lateral bias was comparable between RF NXC and our method in the clutter-to-flow scenario in Fig. 3.2, but in the poor SNR scenario in Fig. 3.1, RF tracking can be observed to performed worse for the lateral velocity estimation.

A comparison of the difference between forward and forward-backward tracking *in vivo* is shown in Fig. 3.4. While the conventional FT method is occluded by a bias towards the surrounding wall, the FBT is not. The vortex appearing in the pulmonary artery of patient 1 with a pulmonary valve stenosis, is in this case only visible when using forward-backward tracking.

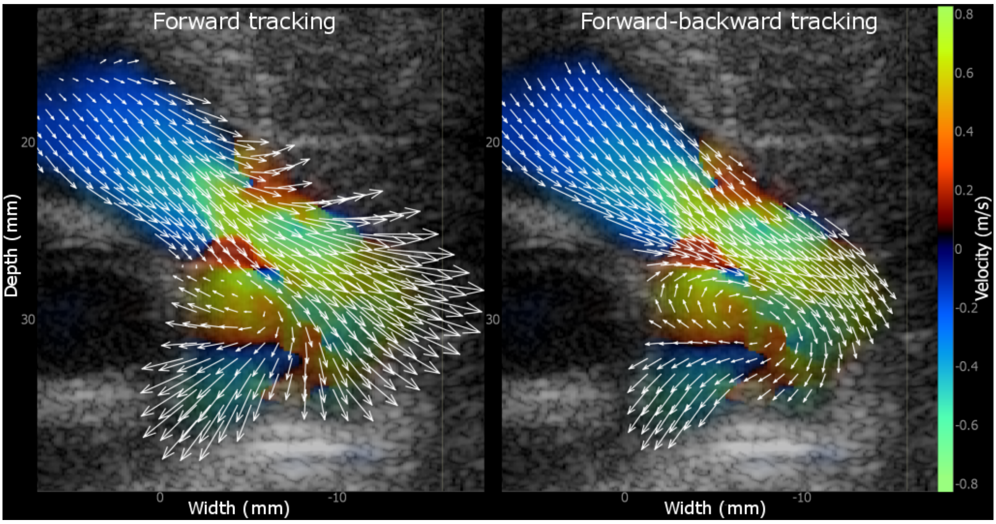

Figure 3.4: Comparison of forward and forward-backward tracking in an *in vivo* example of flow in the pulmonary artery of a newborn (patient 1). The effect of biased velocity estimates is greatly reduced in the image to the right.

3.3.2 Beam profile comparison

Measured lateral beam profiles for the 6S phased array probe for deeply focused (30 cm), unfocused and defocused (focus located 9 cm behind the transducer) transmit beams are shown to the right in Fig. 3.5 for five depths. The five depths are indicated with horizontal lines to the left in the figure and the 16 receive lines are shown as dashed lines. The deeply focused and unfocused beams are similar close to the transducer, but in depth the beam focused at 30 cm is more narrow. At 9 cm the difference between the center and edge of the beam is about 9 dB for the deeply focused compare to 6 dB for the unfocused beam. The slightly diverging beam is still approximately plane at this depth, but the beam intensity lies about 3-6 dB below the two others.

As can be observed, the 16 receive lines span a substantially non-uniform lateral beam profile for deeper regions for the deeply focused beam. A lower accuracy is expected for these regions, and only the inner receive lines should ideally be used in this case. Moving to (slightly) diverging beams this is not an issue, but the uniformity comes at the cost of 3-6 dB loss in SNR. If supported by the system, a higher number of parallel receive lines could then also be used.

3.3.3 Straight tube simulations

Firstly, the accuracy of the tracking estimates over the MLA group was investigated. The straight tube was placed at 9.5 cm depth and two acquisition schemes were simulated; a single deeply focused and a single slightly diverging transmit beams with packet size 16 for 20 frames. The root-mean-square (RMS) error was calculated

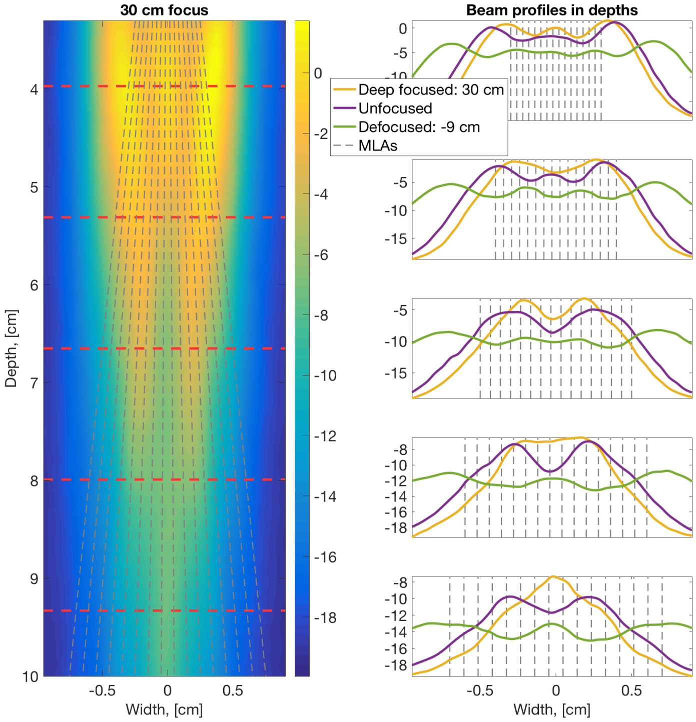

Figure 3.5: Measured beam profiles for the 6S phased array probe for deeply focused (30 cm), unfocused, defocused (focus located 9 cm behind transducer) transmit beams. To the left is an image of the transmit beam focused at 30 cm. The five depths for the lateral beam profiles shown to the right are indicated with horizontal lines. The receive lines are shown as dashed lines.

Table 3.4: Estimated velocity at tube centre line for different depths and steering angles

Steering angle [°]	-30	-20	-10	0
Expected $\|V\|$ [m/s]	1.0	1.0	1.0	1.0
$\|V\|$@45mm [m/s]	0.98 ± 0.06	0.97 ± 0.06	0.98 ± 0.06	0.98 ± 0.04
$\|V\|$@70mm [m/s]	0.96 ± 0.12	1.01 ± 0.09	1.04 ± 0.09	1.05 ± 0.06
$\|V\|$@95mm [m/s]	0.91 ± 0.19	0.90 ± 0.19	0.92 ± 0.14	0.93 ± 0.11

Steering angle [°]	10	20	30
Expected $\|V\|$ [m/s]	1.0	1.0	1.0
$\|V\|$@45mm [m/s]	0.99 ± 0.04	0.97 ± 0.06	0.98 ± 0.07
$\|V\|$@70mm [m/s]	1.03 ± 0.10	1.02 ± 0.10	0.94 ± 0.13
$\|V\|$@95mm [m/s]	0.96 ± 0.12	0.88 ± 0.17	0.85 ± 0.21

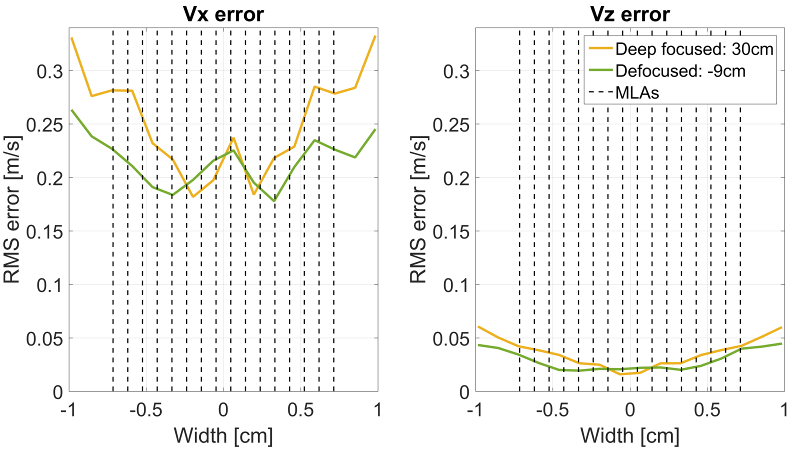

Figure 3.6: Mean root-mean-square (RMS) error over 20 simulated straight tubes at 9.5 cm depth. Left: RMS error for the estimated V_x-component. Right: RMS error for the estimated V_z-component. The extent of the 16 receive lines (MLAs) are shown with vertical dashed lines.

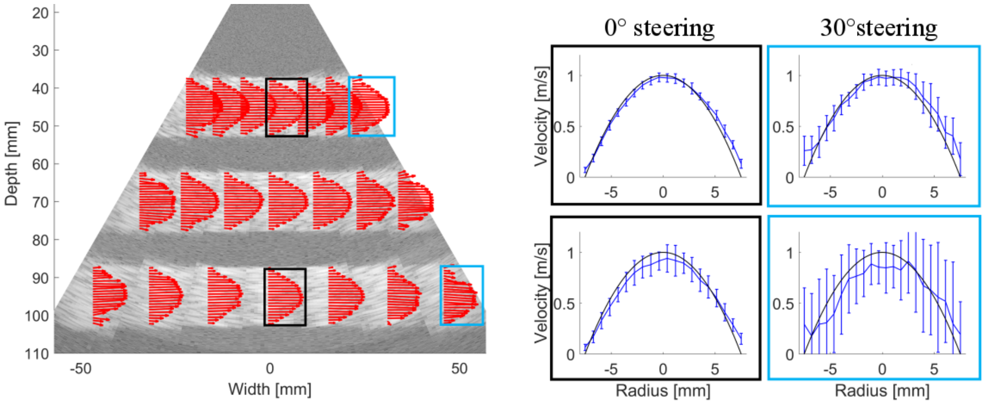

Figure 3.7: Left: Speckle tracking velocity profiles from straight tube simulations for three different depths. Right: Four profiles (middle and far right for depth 4.5 cm and 9.5 cm) shown with standard deviation and the reference velocity (black line).

for both velocity components over the radius of the tube and averaged over the 20 simulated frames and the results are shown in Fig. 3.6. As expected from the beam profiles at depth 9.5 cm in Fig. 3.5, the mean RMS error over the 20 Doppler frames for the deeply focused beam increased when moving outward from the center of the beam, especially for the V_x component. The mean RMS error for the diverging beam did not increase as much over the MLA group. For the V_x-component, both the deeply focused and the diverging beam got a small RMS error increase at the beam center.

Secondly, the accuracy of the tracking estimates when considering imaging depth and steering angle was investigated. Simulated straight tubes were placed at three depths (4.5, 7 and 9.5 cm) and seven deeply focused transmit beams were used to cover an opening angle of 60°. To the left in Fig. 3.7, the estimated velocity profiles for the three tubes are shown. The eight middle beams for each MLA group were averaged before the mean of the 20 simulated Doppler frames results in the final velocity profile. The middle transmit beam gave good results for all three depths, but as the beam was steered out, the velocity profile was clearly degraded in depth. To investigate more closely, four of the velocity profiles (from the middle and far right of depth 4.5 and 9.5 cm) are shown to the right in Fig. 3.7. The black lines indicate the reference velocity and the estimated mean velocity profiles are shown with the standard deviation for the 20 simulated Doppler frames. The standard deviation increases with depth and steering angle. For depth 9.5 cm, the highest steering angle (30°) results in high standard deviations of 20-50 cm/s and an underestimation of the highest velocities.

Table 3.4 gives the estimated velocity at the tube centre for the three depths and all seven steering angles. The reference velocity for all estimates are 1 m/s. For depth 4.5 cm, the maximum velocity is slightly underestimated and with a standard deviation for all steering angles <7 cm/s. At 7 cm, the highest steering angle (±30°) deviates from the rest (which are slightly overestimated) with an underestimation of 4-6 cm/s and a standard deviation of 12-13 cm/s. For the deepest tube, a steering angle of 20°and above gives underestimations of 9-15 cm/s and standard deviations of about 20 cm/s.

3.3.4 Validation of velocity estimates

In Fig. 3.8 the speckle tracking velocity estimates in a small ROI are validated towards a conventional pulsed-wave (PW) Doppler recording from a corresponding ROI. The ST velocity estimates are averaged in the ROI (black square in the image in the left panel) and projected on to the PW acquisition beam axis. The resulting ST velocity trace is plotted on top of the PW Doppler spectrum in the right panel. The velocities in the ROI exceed the Nyquist velocity (0.5 m/s for the color flow acquisition) for the highest velocities, but, as can be observed, the ST velocity estimates still have a good correspondence with the PW Doppler spectrum. A small difference in heart rate is observed between the recordings.

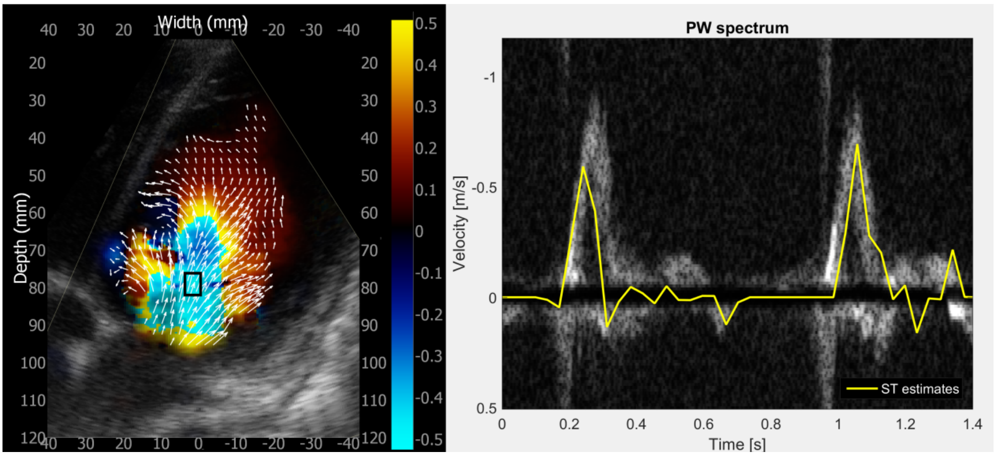

Figure 3.8: Validation of speckle tracking (ST) estimates. Left: Vector flow map overlaid color flow image of the left ventricle of patient 2 (dilated cardiomyopathy). Right: Pulsed-wave (PW) Doppler spectrum acquired from a separate recording. The yellow line represents the ST velocity trace from a corresponding ROI (black square in the left image). The ST velocities have been projected on to the PW acquisition beam for comparison.

3.3.5 *In vivo* results

In Fig. 3.9, patient 1, a newborn with a pulmonary stenosis, is imaged with both the 9L linear array and the 6S phased array probe. The images display the right ventricular outflow tract, the pulmonary valve and the main pulmonary artery branching into the left and right pulmonary artery. The 9L probe clearly provides images of higher resolution compared to the 6S probe, by inspecting the B-mode speckle. The flow field characteristics are, however, similar, displaying the vortex forming in the dilated pulmonary artery distal to the valve.

Fig. 3.10 shows the 9L and 6S images for patient 2, an 11-year-old with dilated cardiomyopathy. Both images are from the parasternal long-axis view where the left atrium, the left ventricle and the left ventricular outflow tract are usually seen. However, a much smaller field-of-view is obtained with the linear array to the left than with the phased array to the right. In this case it was not possible to image the whole region-of-interest due to the narrow image view with the linear array. To the right we can see two vortices forming behind the mitral valve leaflets as the ventricle is filled.

3.4 Discussion

Phased array probes have been tested for the purpose of achieving detailed cardiac flow images of pediatric patients with 2-D blood speckle tracking. We have previously reported that linear arrays can be used to image neonatal hearts as we can image

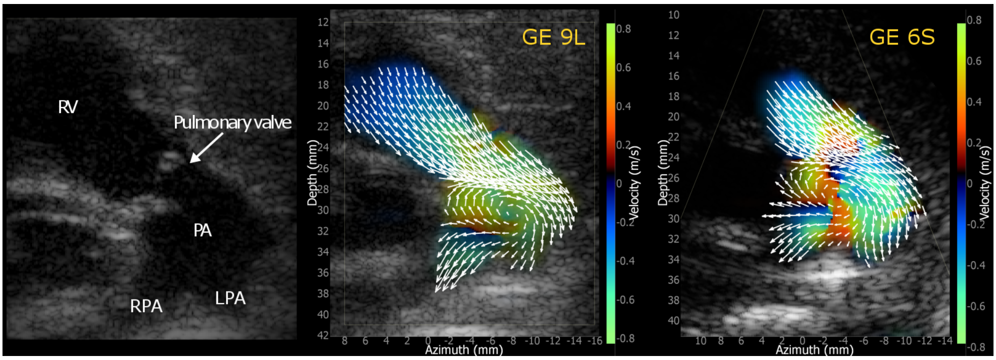

Figure 3.9: A ten-days-old newborn with a pulmonary valve stenosis imaged with both the GE 9L linear array and the GE 6S phased array. RV = right ventricle, PA = pulmonary artery, LPA/RPA = left/right pulmonary artery branch. The speckle tracking velocity estimates are shown as arrows overlaid the color flow image. The large vortex forming in the main PA is seen in both recordings.

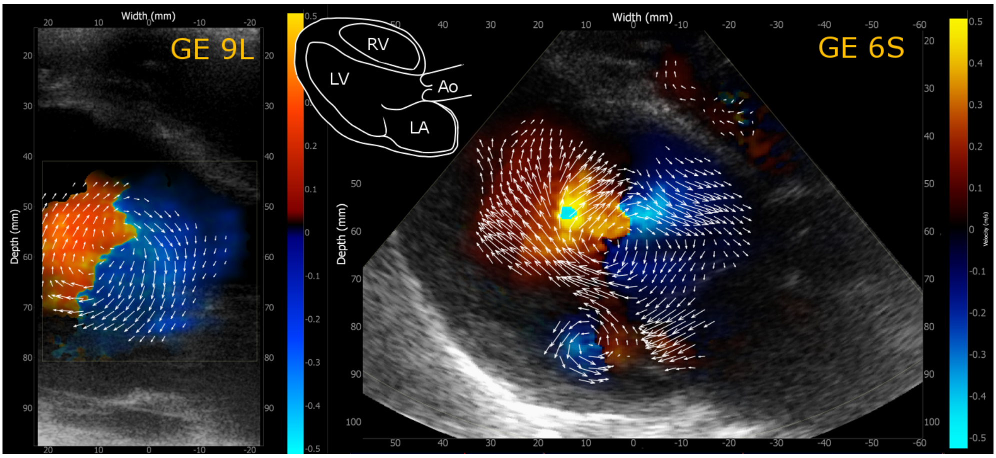

Figure 3.10: An 11-year-old child with dilated cardiomyopathy imaged with both the GE 9L linear array and the GE 6S phased array. LA = left atrium, LV = left ventricle, RV = right ventricle, Ao = aorta. The field-of-view obtained with the linear array is limited. In the phased array-image, two vortices are forming behind the mitral valve leaflets.

straight through the ribs [6], however, the standard pediatric probes are phased array probes and the aim here was to further develop our methods for these probes which are more appropriate when imaging older children.

To improve the speckle tracking velocity estimation, a forward-backward tracking approach was introduced which efficiently reduced bias occurring towards the edges of the flow domain, as seen in Fig. 3.4. In the simple simulations of pure axial motion in Fig. 3.1 and 3.2, it was observed two different bias effects depending on the interfering signals. The direction of the lateral bias was related to the signal sources in the tracking kernel. If the tracking kernel partly contained noise, the lateral bias was towards the noise region for forward tracking. If the tracking kernel contained both decorrelated and correlated signal, the lateral bias pointed towards the correlated (high velocity) region for forward tracking. In both cases, backward tracking gave a bias in the opposite direction, which resulted in the forward-backward averaging removing the bias. For comparison, normalized cross correlation on RF data was performed as a reference method towards our method with SSD envelope tracking. In the lateral direction, RF and envelope tracking are in general comparable, and the lateral bias was present in both simulations. RF tracking was observed to be more susceptible to noise resulting in a lateral bias covering a larger region in the noise-to-flow scenario in Fig. 3.1. Nevertheless, RF tracking has a higher accuracy and lower variance in the axial direction [14].

The drawback of forward-backward tracking was the increased tracking time (tracking both in forward and backward direction), but with the GPU-optimized tracking code the tracking times were still close to real-time (some seconds per cardiac cycle for a high-end GPU), providing bedside applicability. As speckle tracking results are dependent on spatiotemporal averaging, the FBT approach is especially useful when the blood domain is small. With larger domains, as in the heart lumen, this effect can be defeated by trimming the tracking domain before smoothing. However, this is not necessarily straight forward, and the bias may still be included in the averaging window and occlude important flow features as seen in Fig. 3.4.

In our clinical approved real-time imaging setup, we were limited to a 30 cm focus depth and 16 parallel receive lines. Several transmissions were needed to cover the desired ROI which, together with the B-mode acquisition, decreases the total frame rate. Due to diffraction effects, the width of the plane wavefront are reduced in depth as seen in Fig. 3.5, and thus several plane waves would be needed to cover the ROI regardless of the limited number of receive lines. When the image depths exceed 8 cm, the amplitude of both the unfocused and the deeply focused beam falls off when getting closer to the diffraction focus. The loss in SNR on the flanks results in poorer tracking performance on the edges of the MLA groups in depth as seen in Fig. 3.6. The peak observed at the beam center for the V_x-component in Fig. 3.6 can arise from the higher variance in the lateral tracking component compared to the axial tracking component, and in the beam center only the lateral tracking component contributes to the V_x-component.

For diverging wave transmissions, a larger ROI could be covered with only one or a few transmissions. However, for phased-arrays the lower pressure versus depth as seen in Fig. 3.5 would result in a reduced SNR and penetration. It is, unfortunately, not straight forward to utilize coherent compounding to retain this SNR due to the high Doppler PRF needed in this clinical context. However, the increased frame rate could be utilized to increase packet size and thus improve clutter filtering and blood flow detection.

The spatial resolution is poorer with the general pediatric phased array compared with a linear array due to the smaller aperture and lower frequency range. The phased array operation also results in a highly depth-dependent lateral resolution, which degrades the lateral tracking quality increasingly for larger depths and steering angles as seen in Fig. 3.7. It could, in this setting, be beneficial to use a depth dependent tracking kernel which was not used in this work.

Despite the current drawbacks, our experience and preliminary validation towards spectral Doppler in Fig. 3.8 and comparisons with linear array imaging in Fig. 3.9 and 3.10 show promising results. In the patients we have imaged (image depths < 10 cm), vortex formation in the cardiac chambers could be mapped, in addition to a qualitative impression of the primary and secondary blood flow patterns.

3.5 Conclusion

Pediatric phased array probes utilizing broad (deeply focused) pulses and blood speckle tracking were used to image complex flow patterns in two pediatric patients with congenital heart disease. Forward-backward tracking proved important to alleviate a tracking bias occurring at the edges of the flow domain. While promising results were demonstrated for image depths < 10 cm, limitations in penetration are expected compared to conventional color flow imaging, and a larger feasibility study is needed to map the true clinical potential of the approach.

References

[1] D. van der Linde, E. E. M. Konings, M. a. Slager, M. Witsenburg, W. a. Helbing, J. J. M. Takkenberg, and J. W. Roos-Hesselink, "Birth prevalence of congenital heart disease worldwide: a systematic review and meta-analysis.," *Journal of the American College of Cardiology*, vol. 58, pp. 2241–7, nov 2011.

[2] O. J. Benavidez, K. Gauvreau, K. J. Jenkins, and T. Geva, "Diagnostic errors in pediatric echocardiography: development of taxonomy and identification of risk factors.," *Circulation*, vol. 117, pp. 2995–3001, jun 2008.

[3] M. S. Chew and J. Poelaert, "Accuracy and repeatability of pediatric cardiac output measurement using Doppler: 20-year review of the literature.," *Intensive care medicine*, vol. 29, no. 11, pp. 1889–94, 2003.

[4] G. Pedrizzetti, G. La Canna, O. Alfieri, and G. Tonti, "The vortex–an early predictor of cardiovascular outcome?," *Nature reviews. Cardiology*, vol. 11, no. 9, pp. 545–53, 2014.

[5] L. N. Bohs, B. J. Geiman, M. E. Anderson, S. C. Gebhart, and G. E. Trahey, "Speckle tracking for multi-dimensional flow estimation," *Ultrasonics*, vol. 38, no. 1-8, pp. 369–375, 2000.

[6] S. Fadnes, S. A. Nyrnes, H. Torp, and L. Lovstakken, "Shunt flow evaluation in congenital heart disease based on two-dimensional speckle tracking," vol. 40, no. 10, pp. 2379–2391, 2014.

[7] J. Van Cauwenberge, L. Lovstakken, S. Fadnes, A. Rodriguez-Molares, J. Vierendeels, P. Segers, and A. Swillens, "Assessing the performance of ultrafast vector flow imaging in the neonatal heart via multiphysics modeling and in-vitro experiments," *IEEE Transactions on Ultrasonics, Ferroelectrics, and Frequency Control*, vol. 3010, no. c, pp. 1–1, 2016.

[8] H. Takahashi, H. Hasegawa, and H. Kanai, "Echo speckle imaging of blood particles with high-frame-rate echocardiography," *Japanese Journal of Applied Physics*, vol. 53, no. 5S, pp. 07KF08– 1–7, 2014.

[9] G. R. Hong, G. Pedrizzetti, G. Tonti, P. Li, Z. Wei, J. K. Kim, A. Baweja, S. Liu, N. Chung, H. Houle, J. Narula, and M. A. Vannan, "Characterization

and quantification of vortex flow in the human left ventricle by contrast echocardiography using vector particle image velocimetry," *JACC Cardiovasc Imaging*, vol. 1, no. 6, pp. 705–717, 2008.

[10] H. Gao, N. Bijnens, D. Coisne, M. Lugiez, M. Rutten, and J. D'Hooge, "2-D left ventricular flow estimation by combining speckle tracking with Navier-Stokes-based regularization: an in silico, in vitro and in vivo study," *Ultrasound Med Biol*, vol. 41, no. 1, pp. 99–113, 2015.

[11] S. Fadnes, S. A. Nyrnes, M. Wigen, E. Tegnander, and L. Lovstakken, "Detailed flow visualization in fetal and neonatal hearts using 2-D speckle tracking," in *2016 IEEE International Ultrasonics Symposium Proceedings*, pp. 8–11, 2016.

[12] J. A. Jensen and N. B. Svendsen, "Calculation of Pressure Fields from Arbitrarily Shaped, Apodized, and Excited Ultrasound Trandsducers," *IEEE Transactions on Ultrasonics, Ferroelectrics and Frequency Control*, vol. 39, no. 2, pp. 262–267, 1992.

[13] J. A. Jensen, "Field : A Program for Simulating Ultrasound Systems," *Medical & Biological Engineering*, vol. 34, pp. 351–353, 1996.

[14] S. Fadnes, S. Bjaerum, H. Torp, and L. Lovstakken, "Clutter filtering influence on blood velocity estimation using speckle tracking," 2015.

[15] O. Salvado and D. L. Wilson, "Removal of local and biased global maxima in intensity-based registration," *Medical Image Analysis*, vol. 11, no. 2, pp. 183–196, 2007.

[16] S. Fadnes, S. Nyrnes, A. Swillens, H. Torp, and L. Lovstakken, "Shunt quantification in congenital heart disease based on two-dimensional speckle tracking," *IEEE International Ultrasonics Symposium, IUS*, pp. 1877–1880, 2012.

[17] T. Hergum, S. Langeland, E. W. Remme, and H. Torp, "Fast ultrasound imaging simulation in K-space," *IEEE Transactions on Ultrasonics, Ferroelectrics, and Frequency Control*, vol. 56, no. 6, pp. 1159–1167, 2009.

Chapter 4

4D Intracardiac Ultrasound Vector Flow Imaging - Feasibility and Comparison to Phase-Contrast MRI

Morten Smedsrud Wigen[1], Solveig Fadnes[1], Alfonso Rodriguez-Molares[1],
Tore Bjåstad [1,2], Marius Eriksen[3], Knut Haakon Stensæth[3],
Asbjørn Støylen[1], and Lasse Løvstakken[1]
[1] Department of Circulation and Medical Imaging, NTNU, Norway
[2] GE Vingmed, Horten, Norway
[3] Dept. of Radiology and Nuclear Medicine, St. Olavs Hospital, Norway

In vivo characterization of intracardiac blood velocity vector fields may provide new clinical information, but is currently not available for bedside evaluation. In this work, 4D vector flow imaging for intracardiac flow assessment is demonstrated using a clinical ultrasound (US) system and a matrix array transducer, without the use of contrast agent.

Two acquisition schemes were developed, one for full volumetric coverage of the left ventricle at 50 volumes per second (vps), and a 3D thick-slice setup with continuous frame acquisition (4000 vps), both utilizing ECG-gating. The 3D vector velocity estimates were obtained using a novel method combining phase and envelope information.

In vitro validation in a rotating tissue-mimicking phantom revealed velocity estimates in compliance with the ground truth, with a linear regression slope of 0.80, 0.77, and 1.03 for the x, y and z velocity components, and standard deviations of 2.53, 3.19, and 0.95 cm/s, respectively.

In vivo measurements in a healthy left ventricle showed good agreement with PC-MRI.

Quantitative analysis of energy loss (EL) and kinetic energy (KE) further showed similar trends, with peak KE at 1.5 and 2.4 mJ during systole and 3.6 and 3.1 mJ for diastole for US and PC-MRI. Similar for EL, $0.15 - 0.2$ and 0.7 mW was found during systole, and 0.6 and 0.7 mW during diastole, for US and PC-MRI respectively. Overall, a potential for ultrasound as a future modality for 4D cardiac vector flow imaging was demonstrated, which will be further evaluated in clinical studies.

4.1 Introduction

Bedside measurement of detailed three-dimensional intracardiac blood velocity fields in the adult heart is currently unavailable. However, as demonstrated using phase-contrast MRI [1], this information may provide valuable pathophysiological and clinical information when linked to volume flow, energy loss, vortex formation characteristics, pressure gradient maps, and particle residence times, for both myocardial and valvular pathologies [2, 3].

Ultrasound vector flow imaging (VFI) is a methodology where both the angle and magnitude of blood flow velocities are estimated. This is an advancement from traditional Doppler-based measurements, which only measure the velocity component along the direction of the transmitted ultrasound beam, giving the measurements an unfortunate beam-to-flow angle dependency. For Doppler-based approaches alone, interpretation is therefore needed to understand the true blood flow trajectories.

Several VFI approaches have been demonstrated: *vector Doppler* (VD), where multiple ultrasound pulses are transmitted/received with different incident angles [4]; *transverse oscillations* (TO) which applies a lateral modulation on the received signal to estimate both lateral and axial motion [5, 6]; *vector flow mapping*, a model-based reconstruction approach combining Doppler measurements with an underlying blood model and wall measurements [7]; *echo particle image velocimetry (echo-PIV)*, where optical PIV tracking methods are used on contrast-enhanced ultrasound images [8]; and *blood speckle tracking*, which directly tracks the blood speckle pattern between frames [9]. A thorough overview is presented in the papers [10, 11].

Many VFI methods have been applied in and adapted to both vascular and cardiac imaging. Vascular applications use high frequency linear probes due to the relatively wide and shallow field-of-view, with wide apertures beneficial for VFI. Cardiac phased-array probes with small foot prints and lower frequencies are designed to fit between the ribs, and requires both deep and broad acquisition, which decreases the lateral imaging bandwidth, and thus increases the challenge for achieving accurate vector flow imaging.

Some 2D VFI methods have reached clinical scanners in recent years; GE's *blood speckle imaging* (BSI) is based on blood speckle tracking and used in pediatric cardiology; Hitatchi-Aloka offers a *vector flow mapping* approach and is targeting adult echocardiography; BK's *vector flow imaging* and Mindray's *V-flow* are targeting vascular applications based on transverse oscillations and vector-Doppler, respectively.

VFI in 3D has been demonstrated in the research community for vascular applications [12, 13] using vector-Doppler and TO. For cardiac imaging, 3D VFI has been demonstrated using reconstruction based on multiple 3D cardiac views on pediatric patients [14] and multi-planar reconstruction using contrast agents [15]. There are, however, no current methods enabling VFI from a routine 3D cardiac acquisition, which is a motivation for the methodology used in the presented work.

We introduce a method for direct estimation of 3D blood velocities in the adult left ventricle from a single ultrasound acquisition without the use of contrast agents. The method is based on a 3D plane wave color flow imaging (CFI) setup using a clinical 2D matrix array probe and a modified clinical scanner. Two 3D acquisition schemes

Figure 4.1: The acquisition and processing pipeline. ECG-gated CFI and B-mode acquisitions are handled by the scanner and demodulated and beamformed in real-time, before stored for further offline data processing. Preview of the stitched CFI and B-mode data is also available during acquisition. See section 5.2 for further description.

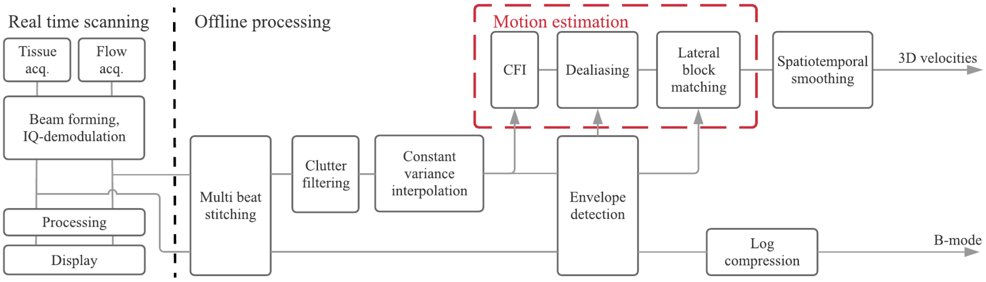

are developed and evaluated, and a new hybrid velocity estimator combining phase and envelope information is described.

The method is validated *in vitro* using a rotating phantom and *in vivo* by comparing 4D ultrasound vector flow velocity fields with the gold-standard for vector flow measurements: phase-contrast MRI.

4.2 Methods

4.2.1 Data acquisition

In state-of-the-art 3D color flow imaging (CFI), multi-beat acquisitions are typically used to maintain adequate frame rates comparable to conventional 2D acquisitions. ECG-gating is utilized to separate a full volume into multiple sub-volumes acquired for each heart cycle, which are stitched together retrospectively under the assumption of a steady heart rate. To compensate for minor heart rate variations, linear stretching of the velocity estimates was applied for the diastolic phase of the cardiac cycle for the time traces.

Two-dimensional matrix array transducers enables the possibility to steer in both azimuth and elevation direction, and hence acquire data from a 3D volume. These probes can have 1024-4096 elements, which today exceeds the number of channels on high-end systems. Subaperture beamforming (SAP) solves this issue by performing partial in-probe beamforming to reduce the number of channels coming from the transducer (to 192 system channels in this work), with a subsequent beamforming stage in the system. The SAP approach results in a larger perceived pitch after the channel reduction, in the second beamforming stage, when conventional receive beamforming is applied on the scanner. This limits the maximum opening angle on receive to avoid grating lobes [16].

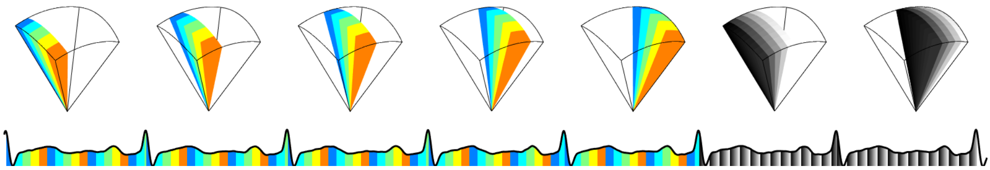

(a) Multi-beat 3D volume (US3D-volume)

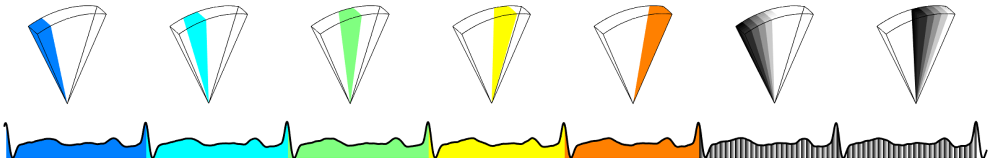

(b) Multi-beat continuous 3D slice (US3D-slice)

Figure 4.2: Illustration of the two multi-beat acquisition setups, both acquiring flow data for five heart beats (colors) and B-mode for two heart beats (gray). The 3D volume acquisition enables full 3D view, while the 3D slice gives a continuous flow acquisition with 3D velocity estimates in one plane.

In this work, two multi-beat acquisition schemes were developed and implemented on a modified GE Vivid E95 ultrasound scanner (GE Vingmed, Horten, Norway) for the GE 4V-D matrix array transducer, as illustrated in Fig. 4.2. For both acquisitions data are recorded over seven heart cycles, where two are used for B-mode and five for flow.

1. Multi-beat 3D volume acquisition (US3D-volume): Acquired data covers the whole left ventricular chamber. A packet-based acquisition was used for flow estimation.

2. Multi-beat 3D continuous slice acquisition (US3D-slice): A single 3D slice is acquired, where one transmit direction is used per heart beat resulting in a continuous frame acquisition for each subvolume.

Broad beams (plane waves) were used on transmission, with a $\sim$ $10^\circ \times 10^\circ$ opening angle on receive, and beamformed real-time on the scanner with a 12×10 multiple line acquisition (MLA). Live preview of the stitched CFI and B-mode data was available during acquisition. The in-phase and quadrature (IQ) data were also stored for further off-line processing and vector flow estimation, along with B-mode data and ECG traces. The full pipeline of data acquisition and processing for 3D VFI is shown in Fig. 5.2 and further described in the next subsections. See Table 4.3 for further details on transmit and receive parameters.

4.2.2 Filtering and preprocessing

The acquired IQ-data is clutter filtered to suppress stationary tissue signals before blood motion estimation. A polynomial-regression (polyreg) clutter filter was used, where an adaptive filter order selection was implemented by using the average tissue-Doppler velocity in each frame weighted with the voxel envelope intensity, which was linearly related to a filter order cut-off velocity.

IQ-interpolation was performed to double the lateral image sampling prior to envelope detection and CFI. To ensure the same statistics of interpolated samples, constant-variance resampling was employed [17]. Further, linear interpolation was performed on the envelope data during block matching, using fast GPU texture interpolation in the parallel implementation of the algorithm.

4.2.3 3D block matching

A 3D block matching procedure calculates a 3D similarity function between the envelope data frames, e.g. sum-of-squared-differences (SSD) sum-of-absolute-differences (SAD) or normalized-cross-correlation (NCC), exemplified here using SSD:

$$\begin{aligned} &SSD_{\theta,\gamma,r}(\theta_s,\gamma_s,r_s,f,\Delta_{\mathrm{lag}}) = \\ &\sum_{\theta_k,\gamma_k,r_k}^{K_{\mathrm{dims}}} [|IQ|(\theta+\theta_k,\gamma+\gamma_k,r+r_k,f) - \\ &|IQ|(\theta+\theta_k+\theta_s,\gamma+\gamma_k+\gamma_s,r+r_k+r_s,f+\Delta_{\mathrm{lag}})]^2, \end{aligned} \tag{4.1}$$

where θ, γ, r are the spatial coordinates of a velocity estimate in the imaging volume and f is the frame number. The variables θ_k, γ_k, r_k iterates over the kernel dimensions, K_{dims}, centered at the spatial positions in the discrete search region defined by θ_s, γ_s, r_s. The search grid spacing and size defines the velocity resolution and the maximum velocit y, $V_{\mathrm{res},V_{\max}}$, that can be measured from the discrete similarity matrix of dimensions $N_{\theta_s} \times N_{\gamma_s} \times N_{r_s}$. The density of the search grid defines the V_{res}, while the extent defines the $V_{\max}$. The discrete shift estimate is given by the best match as follows

$$[\Delta_\theta, \Delta_\gamma, \Delta_r] = \mathrm{argmin}(SSD). \tag{4.2}$$

For subsample estimation, $\delta_\theta, \delta_\gamma, \delta_r$, parabolic fitting of the SSD function can be further applied, before the shifts are converted to velocities according to

$$\vec{V}_{\theta,\gamma,r} = [v_\theta, v_\gamma, v_r] = [\frac{\Delta_\theta+\delta_\theta, \Delta_\gamma+\delta_\gamma, \Delta_r+\delta_r}{PRF}], \tag{4.3}$$

where PRF is the pulse repetition frequency.

To maintain a constant $V_{\mathrm{res}}/V_{\max}$ at all depths r, a position dependent tracking grid resolution was used following

$$\Delta_{\theta_s,\gamma_s} = \frac{V_{\mathrm{res}}}{r \cdot PRF}. \tag{4.4}$$

The tracking kernels were adapted to the depth-dependent spatial resolution obtained with phased-array probes. A depth limit, r_{lim}, is defined, to where the initial kernel size, $K_{\text{widths},0}$ is kept constant. For deeper tracking coordinates, the kernel size is linearly increased in the lateral directions as follows

$$K_{\text{width}} = K_{\text{width},0} \cdot \max(1, \frac{r}{r_{lim}}). \tag{4.5}$$

Due to the rectangular shape of the probe, this depth limit is found separately for the azimuth and elevation directions. The kernel resolution in beamspace is further calculated using

$$\Delta_{\theta_k,\gamma_k} = \frac{K_{\text{width}}}{r \cdot K_{\text{dims},\theta_k,\gamma_k}}. \tag{4.6}$$

As described in [18], a forward-backward approach can be used to reduce variance and cancel spatial biases, at the cost of processing time. The method was utilized with a modification where the average between the forward and backward tracking is applied on the similarity matrix as follows

$$SSD_{FW} = SSD_{\theta,\gamma,r}(\theta_s, \gamma_s, r_s, f, 1) \tag{4.7}$$

$$SSD_{BW} = SSD_{\theta,\gamma,r}(\theta_s, \gamma_s, r_s, f+1, -1) \tag{4.8}$$

$$SSD_{FB}(\theta_s, \gamma_s, r_s, n) = (SSD_{FW} + SSD_{BW}^T). \tag{4.9}$$

In our implementation, tracking was performed in spherical beam space, given by (4.3), and was further scan converted to cartesian coordinates.

4.2.4 Hybrid velocity estimation

A hybrid velocity estimator was developed to exploit the phase-information in the IQ data. The proposed method combines Doppler estimation for the radial velocity component with block-matching both for dealiasing and for the lateral velocity estimation separately. This was done to decrease the radial velocity variance [19] and reduce processing time compared to full 3D block-matching (see 4.2.6). The following steps describes the hybrid velocity estimator, with more details in Table 4.1 and basic principles illustrated in Fig. 4.3.

1. CFI + dealiasing: Color flow images were calculated using the autocorrelation method (ACM) [20] according to

$$\begin{aligned} V_{\text{ACM}} = & \frac{V_{\text{Nyq}}}{\pi \cdot (N_p - 1)} \cdot \\ & \angle \sum_{f=1}^{N_p-1} IQ(\ldots, f)^* \cdot IQ(\ldots, f+1), \end{aligned} \tag{4.10}$$

   where f is the frame number in the packet (Doppler ensemble) and N_p is the packet size. The Nyquist velocity is defined by

$$V_{\text{Nyq}} = \frac{c_0 \cdot PRF}{4 \cdot f_0}, \tag{4.11}$$

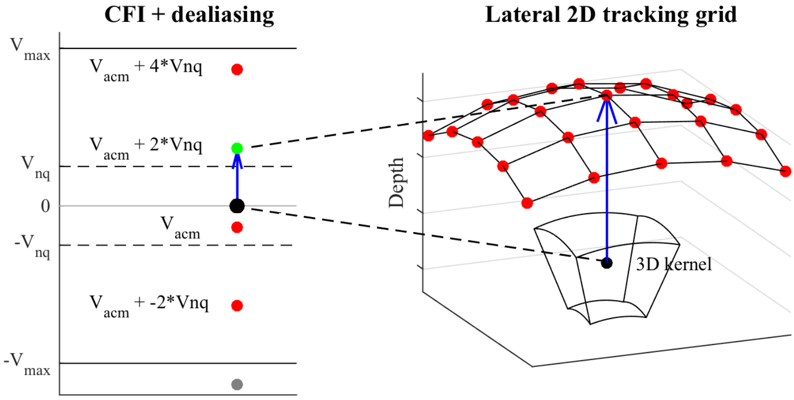

Figure 4.3: A 3D kernel is used for block-matching-based dealiasing, where the final radial estimate is used to establish the search grid for the lateral component. The lateral block matching is then performed with a 3D kernel in beamspace.

where c_0 is the speed of sound in blood and f_0 the pulse center frequency. This gives a potentially aliased radial velocity estimate, V_{ACM}. A 3D extension of the 1D aliasing correction algorithm described in [21] was used, where the spatial correlation at discrete positions corresponding to aliased velocities is calculated, and the best match used to select the dealiased estimate. The number of aliased candidates are given by

$$N_{\text{candidates}} = \lceil \frac{V_{\max}}{V_{\mathrm{Nyq}}} \rceil, \tag{4.12}$$

where the corresponding candidates' velocities are given by

$$\begin{aligned} V_i = V_{\mathrm{ACM}} - \operatorname{sign}(V_{\mathrm{ACM}})(-1)^i \cdot 2V_{\mathrm{Nyq}} \lfloor \frac{i}{2} \rfloor, \\ i = [1, N_{\text{cand.}}]. \end{aligned} \tag{4.13}$$

These velocities are used to determine the position for further calculation of the spatial correlations using

$$\begin{aligned} V_{r,f} = \operatorname{argmin}_{V_i}(SSD(0, 0, \frac{V_i}{PRF}, f)), \\ f = [1, \mathrm{N_p} - 1]. \end{aligned} \tag{4.14}$$

The best match follows from (4.2), and the *mode* over the packet size, N_p, determines the final radial estimate, V_r:

$$V_r = \operatorname{Mode}(V_{r,f})_{\mathrm{N_p}}. \tag{4.15}$$

2. Lateral block matching: By using the radial velocity estimate from CFI, the block matching reduces to a shifted 2D search with a 3D kernel to estimate the lateral velocity components:

$$\begin{aligned}[\Delta_\theta, \Delta_\gamma] = \text{argmin}_{\theta_s,\gamma_s}(SSD(\theta_s, \gamma_s, \frac{V_r}{PRF}, f)),\\ f = [1, \mathrm{N_p} - 1].\end{aligned} \tag{4.16}$$

3. Subsampling is further applied in the lateral directions as described in Sec. 4.2.3.

4.2.5 Spatiotemporal smoothing

A median filter is first applied in time to reduce outliers before Gaussian spatial smoothing, defined in Tab. 4.1, to reduce variance. This was also used to fill in gaps of invalid measurements in the MLA transitions. To reduce processing time for smoothing a truncated Gaussian kernel was used, with a window length equal to one standard deviation.

$K_{\text{size},0}$ in x, y, z, [mm]	$1, 1, 1$
Kernel depth limit, [cm]	5
Kernel size for dealiasing, [mm]	$7 \cdot K_{\text{size}}$
Kernel dimensions in x, y, z, [px]	$5, 5, 5$
Block matching $V_{\text{res}}, V_{\text{max}}$, [m/s]	0.4, 2.0
Matching criteria	SSD
Sub sampling	Parabolic fitting
Gaussian window std in x, y, z, [mm]	$8, 8, 8$
Gaussian window std in time, [ms]	80
Truncated Gaussian window length, [std]	1

Table 4.1: Tracking setup

4.2.6 Implementation and computation time

The full 3D block matching procedure described in Sec. 4.2.3 would give calculations according to

$$N_{\text{3D}} = N_{\text{kernel}} \cdot N_{\theta_s} \cdot N_{\gamma_s} \cdot N_{r_s}, \tag{4.17}$$

where N_{kernel} is the kernel dimensions, while $N_{\theta_s}, N_{\gamma_s}, N_{r_s}$ are the dimensions of the search grid, given by $1 + 2 \times \lceil V_{\text{max}}/V_{\text{res}} \rceil$. In comparison, the number of calculations needed by the proposed hybrid method is given by

$$N_{\text{hybrid}} = N_{\text{kernel}} \cdot (N_{\theta_s} \cdot N_{\gamma_s} + N_{\text{cand.}}), \tag{4.18}$$

where $N_{\text{cand.}}$ are the number of aliased candidates found in (4.12). By replacing the radial search with the proposed CFI + dealiasing approach, we get a reduction in number of calculations given by

$$\frac{N_{\text{3D}}}{N_{\text{hybrid}}} = \frac{N_{\theta_s} \cdot N_{\gamma_s} \cdot N_{r_s}}{N_{\theta_s} \cdot N_{\gamma_s} + N_{\text{cand.}}}. \tag{4.19}$$

For the setup described in Sec. 4.2.1, $V_{\max}/V_{\text{Nyq}} = 3$, and $N_{\theta_s} = N_{\gamma_s} = N_{r_s} = 5$, a theoretical computational reduction factor of ~ 5 should therefore be achieved. The same tracking kernel size is then used for both dealiasing and lateral tracking. In practice, however, it was found beneficial using an increased kernel size for the dealiasing step.

The hybrid motion estimation algorithm was implemented in CUDA and ran on an NVIDIA Titan V GPU. The actual processing time for the US3D-volume setup was from $\sim 3 - 15$ seconds per frame (packet size 14), depending on the dealiasing kernel size and density. In comparison, a full 3D block matching approach would take ~ 30 seconds per frame for a typical setup.

4.2.7 Calculation of global integrated parameters

Integration of energy loss and kinetic energy was used as global measurements for comparison between the full volumetric acquisitions. From the Navier-Stokes equations, under the assumption of blood being a Newtonian fluid, the viscous dissipation function can be calculated according to

$$\Phi = \frac{\mu}{2}\sum_{i=1}^{3}\sum_{j=1}^{3}[(\frac{\partial v_i}{\partial j} + \frac{\partial v_j}{\partial i}) - \frac{2}{3}(\nabla \cdot \vec{v})\delta(i-j)]^2, \tag{4.20}$$

which is the energy loss per volume unit, where $\vec{v}$ is the three-dimensional velocity vector, δ is the Dirac delta function, and $\mu = 0.004\ \text{Pa} \cdot \text{s}$ is the coefficient of viscosity for blood. To get a measure of energy loss for a given frame, the viscous dissipation for all voxels, vx, in a segmented ventricle region can be integrated using

$$EL(t) = \sum_{vx=1}^{N} \Phi_{vx}(t)dV,\ [W], \tag{4.21}$$

where dV is the voxel volume. The total kinetic energy can be integrated from the velocity amplitudes in the same region of interest according to

$$KE(t) = \frac{\rho}{2}\sum_{vx=1}^{N} ||V_{vx}(t)||^2 dV,\ [J] \tag{4.22}$$

where $\rho = 1.025\ \frac{\text{kg}}{\text{m}^3}$ is the density of blood.

4.3 Validation

4.3.1 *In vitro* validation

For *in vitro* validation, an experimental setup with a tissue-mimicking rotating phantom was developed. An agar based phantom casted as a cylinder was attached to a stepper motor, setup with 1 m/s as maximum velocity at the edge of the phantom. The phantom was inserted into a water chamber and imaged through a silicone window. Care was taken to ensure the same speed of sound in the agar and liquid, as well as in the system beamforming algorithm. This was done to avoid geometric distortion in the positions and bias in the estimated velocities. The cylinder center was placed at 7 cm depth from the transducer. From the relation between the angular velocity and radius of the phantom, an analytic ground truth was calculated.

4.3.2 *In vivo* validation

A Siemens Avanto 1.5 Tesla MRI scanner, with software version SyngoB19, was used for *in vivo* validation. Velocity data was acquired with a phase-contrast four-point method [22], using a velocity encoding limit of 1.0 m/s. The magnitude frames where inverted, for anatomic reference images, for closer similarity with ultrasound B-mode where the heart walls appear the brightest. Acquisition was done slice-by-slice with periods of breath-holding, for 15 minutes in total. See Table 4.2 for further details.

Magnetic field strength, [Tesla]	1.5
Acquisition mode	2D, slice-by-slice
Slice orientation	Long axis view
Acq. matrix (phase, freq.),	256/88
Acq. resolution, [mm]	4.01, 2.82
Number of slices	17
Slice thickness, [mm]	6
# Phase encoding steps	90
V_{enc}, $[\frac{m}{s}]$	1.0
Mean heart rate[1], [bpm]	63
Heart rate min/max[2], [bpm]	58/74
Echo time, [ms]	4.32
Repetition time, [ms]	146
Flip angle	30°

Table 4.2: PC-MRI setup

4.3.3 *In vivo* feasibility

The *in vivo* example, with an associated PC-MRI acquisition, is from a healthy 28-year-old male volunteer, acquired by a cardiologist. The recordings are standard apical views showing the left ventricle (LV), the left ventricular outflow tract (LVOT) and parts of left atrium (LA). Details regarding the setup is found in Table 4.3. An additional recording was acquired from another healthy volunteer (25-year-old male), without corresponding PC-MRI data, where supplementary materials are available in the supplementary files /multimedia tab.

Transmit	
Center frequency, [MHz]	3.0
Sample volume, [mm]	1.0
Focus	Unfocused
Apodization	Rectangular
PRF, [Hz]	4-4500
Packet size (US3D-volume)	14

Receive	
Apodization	Rectangular
Opening angle (θ, γ)	$(8^\circ - 10^\circ) \times (8^\circ - 10^\circ)$
No. MLAs (θ, γ)	12×10
# heart cycles	7: 2 B-mode + 5 CFI
Frame rate, [frames/s] (US3D-volume, US3D-slice)	50, PRF

Table 4.3: Ultrasound setup

4.4 Results

4.4.1 Dealiasing

The dealiasing method was evaluated quantitatively in terms of bias and variance *in vitro* using the rotating phantom, and qualitatively *in vivo* by careful inspection of the results before and after aliasing correction. In Fig. 4.4, time-averaged color flow images and corresponding standard deviation from the rotating phantom are shown before and after aliasing correction. Aliasing is clearly present before correction, also leading to a large increase in standard deviation in this region. Note, the MLA-borders are visible as white indicating unavailable data, which are filled in later in the smoothing procedure. The dealiased results show that the method works well under ideal conditions in the *in vitro* setup, reconstructing the true velocities and lowering the standard deviation.

In Fig. 4.5, *in vivo* images from a healthy left ventricle is shown for frames in both systole and diastole where aliasing is present. The aliasing correction provided visually accurate results throughout the cardiac cycle, with only minor deviations. Note that no smoothing was applied in the figure to represent the estimates as they are used for further lateral tracking.

4.4.2 *In vitro* results

The velocity estimates from the *in vitro* setup were used to analyze the bias and standard deviation over all acquired frames, including spatiotemporal smoothing. The rotating phantom was imaged from two views, *in-plane* and *through-plane* with the continuous 3D slice setup. In-plane, a full disk cross section was imaged, assuming a zero elevation component. These results are shown in the top row scatter plots in

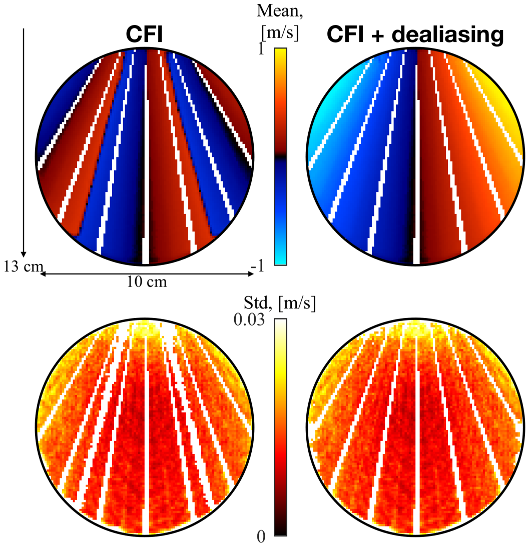

Figure 4.4: CFI with and without dealiasing for the rotating phantom. Expected values in the top panel and corresponding variance in the lower panel. MLA transitions visible as white stripes indicating unavailable data.

Fig. 4.6. The probe was rotated 90° to investigate the performance in the through-plane (elevation) direction. These results are given in the bottom row in Fig. 4.6. Here, all azimuth and radial components are assumed to be zero. The linear regression analysis revealed a slope and standard deviation of 0.8 and 2.53 cm/s for the in plane x-direction, 1.03 and 0.95 cm/s for the in plane z-direction, and 0.77 and 3.19 cm/s for the through plane y-direction.

The smoothing parameters for the rotating phantom data were $7\,\text{mm}^3$ and 70 ms for a frame rate of 50 vps, equivalent to $7 \times 7 \times 7$ voxels in space and 4 frames in time. The tracking output is consistent with the ground truth, but an underestimation can be observed for higher lateral velocities, in particular in the elevation direction (y-direction). This becomes most apparent at velocities $> 50\,\text{cm/s}$. The assumed stationary components also have some influence, probably due to misalignment of the imaging plane, and estimator bias/variance.

4.4.3 *In vivo* results

For the US3D-volume acquisition 5×5 subregions were acquired in order to cover the left ventricle. A measurement frame rate of 50 vps, including 1150 *tracking* frames (vps × packetsize), was then achieved. For US3D-slice a vps equal to PRF (4000-

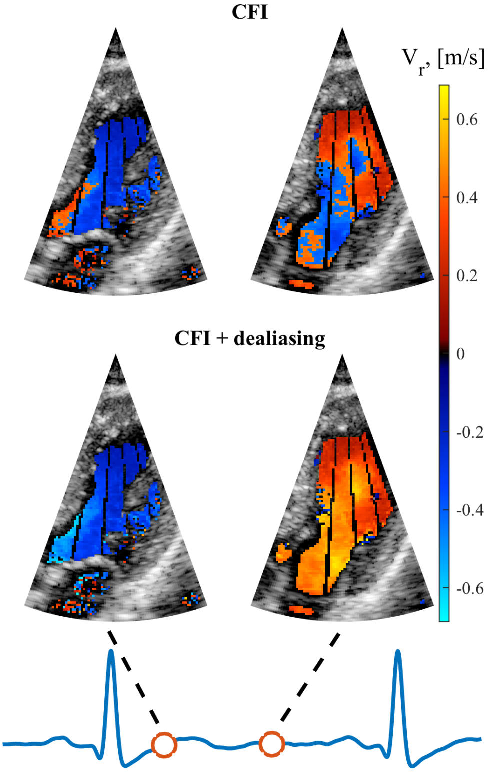

Figure 4.5: CFI with and without dealiasing for *in vivo* data, at two time points corresponding to systole and diastole, respectively. The data are presented without smoothing, hence the present MLA transitions (black stripes in this case).

4500 Hz), was obtained, by using 5 × 1 subregions over 5 heart beats for CFI. [3]. For both acquisitions each subregion consisted of 12x10 = 120 image lines which were beamformed in parallel.

The US3D-volume acquisition and the PC-MRI data was sliced to get an arbitrary view of the heart. The US3D-slice, however, was recorded for one view at the time. Fig. 4.7 shows the acquired velocity field for a selection of three views: apical long axis (ALAX), apical four chamber (A4C) and apical two chamber (A2C). The first is shown at two time points. The slices are manually registered, some differences in orientation is probably present.

In the ALAX view, both acquisitions show similar outflow velocities in systole.

---

[3] Speckle tracking is always performed between frames at PRF rate. With packet acquisition the average over the packet is used as one tracking frame. With continuous acquisition vps = *tracking* vps = PRF.

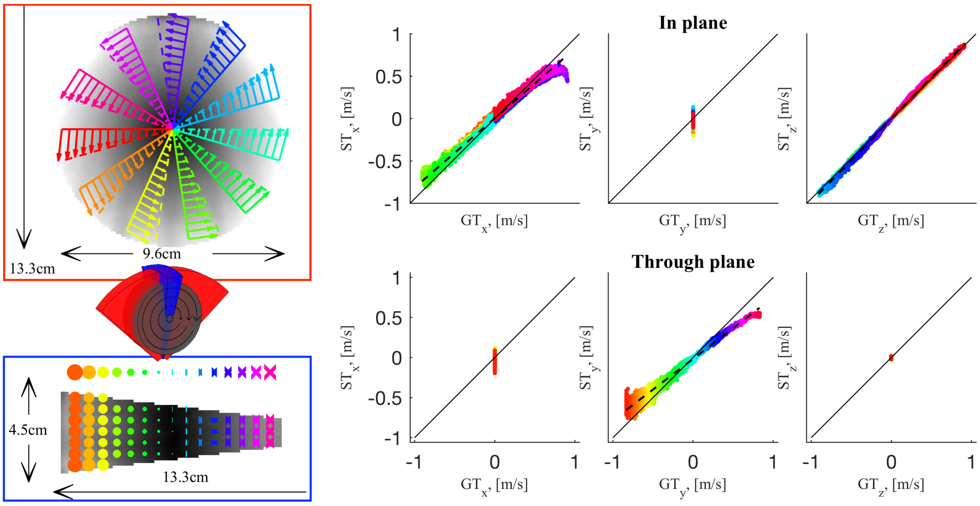

Figure 4.6: *In vitro* validation of the tracking method with a rotating phantom. Two 3D slice acquisitions were obtained, one *in-plane* illustrated in red and one *through-plane* illustrated in blue. The scatter plots to the right show the correlation between the estimated x, y and z velocities and the ground truth of the rotating phantom. The in-plane acquisition velocity was expected to only lie in the x and z direction. The probe was rotated 90° for the through-plane acquisition giving only the velocity component in the y direction.

The US3D-slice and PC-MRI showed good correspondence, where the velocity vectors qualitatively follow the left ventricular outflow tract (LVOT). The US3D-volume setup showed similar velocity field characteristics with increasing magnitude toward the aorta, however did not capture the same flow direction in the LVOT for this particular example. Such artifacts are further discussed in Sec. 4.5.

During diastole, the ALAX view is dominated by vortex formation and flow behind the mitral valve towards the left ventricular outflow tract. In the US3D-volume, swirling flow is also observed at the left side of the valve.

In the A4C view during diastole the inflow through the mitral valve is captured. The flow fields appear similar between US3D-volume and PC-MRI, where both show a tilted inflow towards the right, with a small swirling flow pattern on the right side behind the mitral valve leaflet.

The A2C view is dominated by low velocity flow moving towards the apex in the central parts of the lumen before a clock-wise vortex is forming close the apex. These features are present in all recordings with similar magnitudes.

An additional comparison with a 25-year-old male volunteer, without corresponding PC-MRI validation, is found in the supplementary Fig.1 (available in the supplementary files /multimedia tab). The comparison are based on the same views as in Fig. 4.7 from one volumetric acquisition.

The continuous US3D-slice acquisition enables the calculation of the Doppler

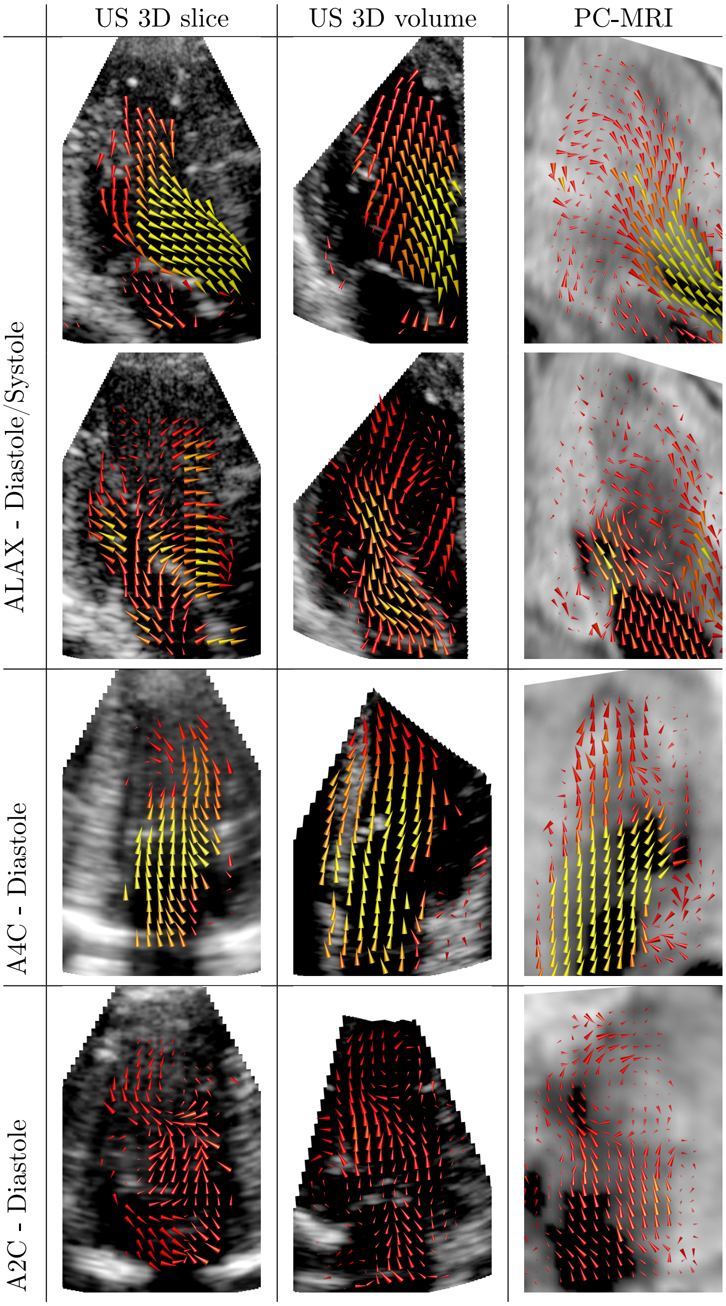

Figure 4.7: US 3D slice and volume and PC-MRI compared for a selection of views. Separate acquisitions were required for each US 3D slice view, while a single acquisition was sufficient for the US 3D volume acquisition as the desired views could be sliced from the full volume. The PC-MRI acquisition was acquired slice-by-slice in the long axis orientation.

spectrum anywhere in the image, which in this context also works as an additional reference measurement when carefully angle-corrected. In Fig. 4.8 two velocity traces are shown from the aortic outlet and the mitral inlet, as well as two global integrated energy plots for energy loss and kinetic energy, for both ultrasound setups and PC-MRI compared to the corresponding Doppler spectrum from the US3D-slice acquisition. Linear stretching of the time traces in the diastolic phase was applied, from manual definition of the time of aortic valve closure. The location of the sample volumes are marked in the reference images to the left in the figure. The lines at the sample volume locations show the angles used for angle correction of the Doppler spectra, and was kept constant throughout the cardiac cycle. The angle correction was only applied in-plane in the image. To compare the velocity magnitude traces with the Doppler spectra, a sign value was added corresponding to the ventricular long-axis. The plotted squares on the reference images correspond to the smoothing region. For PC-MRI this corresponds to the non-interpolated image voxel dimensions (see Table 4.2). The smoothing window in time is plotted in the top trace plot. For calculation of the global integrated energy calculations, the PC-MRI data was averaged with a 3x3x3 moving average filter, due to noise sensitivity of gradient based methods as energy loss. The spectra give a good indication of other interfering signals in the ultrasound data, such as remaining tissue clutter signal.

For the mitral inflow scenario in Fig. 4.8, the velocity traces reaches a positive peak of $\sim 50 - 70\,\mathrm{cm/s}$ during diastole. In the systolic phase all traces have negative shifts, with a lower peak of $\sim 20\,\mathrm{cm/s}$ for PC-MRI and US 3D volume, and $\sim 30\,\mathrm{cm/s}$ for US3D slice. Throughout the cycle, PC-MRI appears with more slowly varying velocity changes, and also less detailed due to lower temporal resolution and averaging effects. Due to the original differences in heart rate between the recordings, the different phases in the cardiac cycle are not completely aligned. The trends corresponds well with the Doppler spectrum, however, with differences in magnitude. The maximum velocity in the filling during the a-wave is lower for PC-MRI than both US 3D slice and volume, $23\,\mathrm{cm/s}$, $55\,\mathrm{cm/s}$ and $28\,\mathrm{cm/s}$, respectively. Likely, the view difference is the main cause of this underestimation.

The aortic outflow velocity traces in Fig. 4.8 show good correspondence between the US acquisitions and PC-MRI velocity estimation, although with some deviations in magnitude. Both US 3D slice and PC-MRI are in compliance with the Doppler spectrum for the peak negative velocity during systole at $\sim 76 - 78$ cm/s, while US 3D volume yielded ~ -59 cm/s. Again, the PC-MRI curve shows less dynamics compared to the US traces throughout the cardiac cycle. The different curves reaches a positive velocity peak during diastole with varying magnitudes, and end up at a low negative velocity between $\sim 10 - 20$ cm/s before the a-wave.

The global integrated kinetic energy plot (KE) shows magnitudes between 0 and $4\,\mathrm{mJ}$ for both modalities. However, deviations in magnitudes are observed when comparing the individual timepoints, especially in the systolic phase where US is dominated by lower kinetic energy values, with peak values of 1.5 mJ and 2.4 mJ, for US and PC-MRI, respectively. In diastole the deviations are seemingly mainly due to differences in the cardiac phase offsets, where the plots reaches a maximum of 3.6 mJ and 3.1 mJ respectively. Both plots ends diastole at ~ 0.5 mJ.

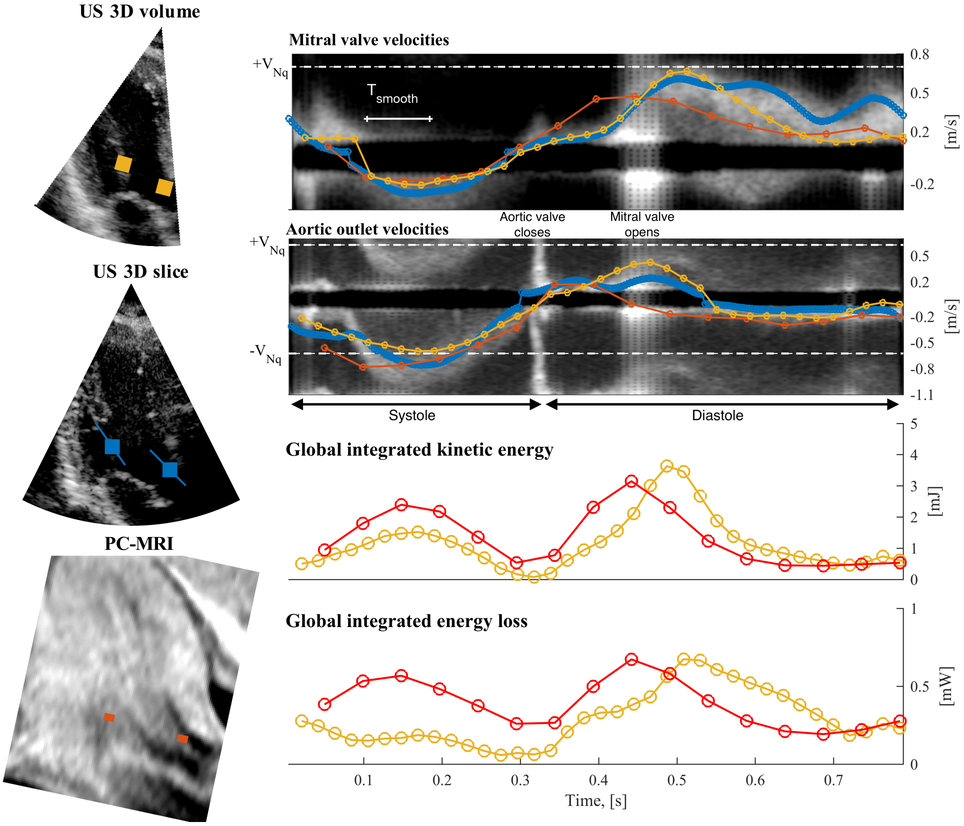

Figure 4.8: The top two plots show velocity trace magnitudes for ultrasound VFI and PC-MRI, on top of the corresponding Doppler spectra from the same ultrasound acquisition (US3D-slice). The trace sign corresponds to the long-axis up/down direction. The bottom two plots show integrated global energy estimates for the volumetric acquisitions (PC-MRI in red and US3D-volume in yellow). To compensate for differences in heart rate, the time traces are aligned by linearly stretching the diastolic phase.

The global integrated energy loss (EL) plot shows some of the same tendencies as the KE plot, while here the deviation in the systolic phase is more prominent. In systole US shows values between $0.15 - 0.2$ mW and lacks a dominant peak value, while PC-MRI reaches a maximum of 0.6 mW. In diastolic phase both plots reaches a maximum of ~ 0.7 mW, but also here the plots are shifted relative to each other.

The comparison of the energy plots in the supplementary Fig. 2 (available in the supplementary files /multimedia tab) show that the two volunteers had synchronized traces. The two had similar heart rates (76 and 78 bpm for subject 1 and 2) resulting in no needed reinterpolation. Deviation of 1 mJ and 0.2 mW for KE and EL was present in the systolic phase, while the amplitudes had smaller deviations during diastole.

Fig. 4.9 shows 3D flow path lines from three parts of the cardiac cycle: diastole, diastasis and systole, respectively. The data were acquired with the US3D-volume acquisition over seven heart beats. The first frame is showing inflow from the left atrium through the mitral valve. Swirling flow patterns are observed in the lumen and behind the posterior mitral leaflet. In the second frame a larger vortex formation in the central lumen can be observed in the diastasis. The last frame shows outflow towards the aorta. A full length movie is available in the supplementary files /multimedia tab.

Figure 4.9: The figure shows a 3D rendering of the flow path lines in three parts of the cardiac cycle corresponding to diastole, diastasis and systole, respectively. A full length movie is available in the supplementary files /multimedia tab.

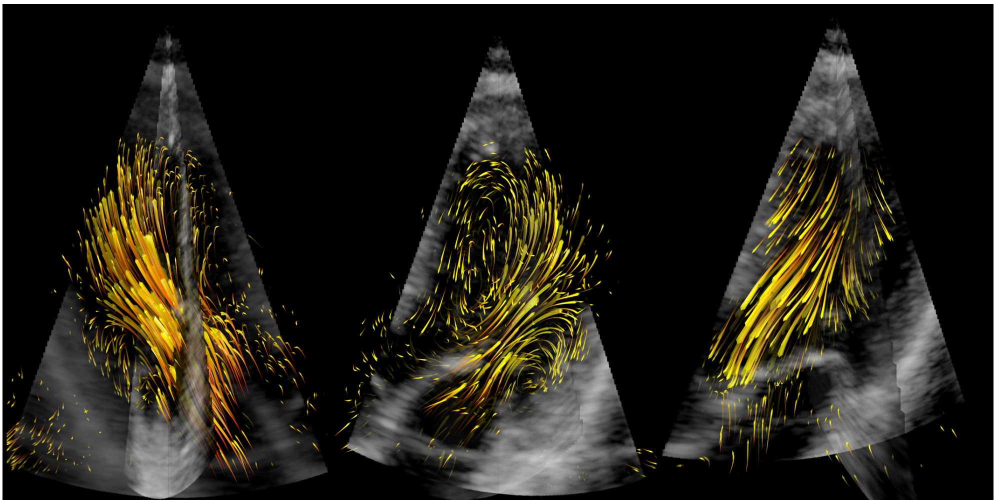

4.5 Discussion

In this work, we implemented and validated two acquisition setups for 4D vector flow imaging using a modified clinical system and a 2D matrix array transducer. Further, a blood velocity estimator was proposed, combining Doppler estimation of the radial velocity component with lateral 2D block matching. *In vitro* validation was done using a rotating tissue-mimicking phantom, while *in vivo* application from a healthy volunteer was demonstrated and compared to 4D phase-contrast MRI measurements.

Color flow imaging in 3D requires a high number of pulse emissions which substantially increases the frame acquisition time. While it was possible to obtain a real-time color flow frame rate of 10 vps for a 40° × 40° volume in our setup, this is typically too restricted for clinical use. By gating over multiple beats we could increase both the volume size and frame rate to achieve 50 vps. This requires a steady heart beat and sometimes breath-hold. In our multi-beat setup, we used seven heart beats to acquire one heart cycle: five for CFI and two for B-mode as illustrated in Fig. 4.2. Gating over even more cycles could further increase the frame rate, but would be impractical in a clinical setting.

Both the slice and volume acquisitions developed provided real-time color flow imaging while recording. The modified scanner allowed for IQ-data storage giving us the opportunity for offline data processing and 3D vector flow estimation. The processing scheme thus enable bedside acquisition, while offline processing is currently needed for velocity estimation. Central for the acquisition setups was the use of broader transmit beams and parallel beamforming to increase the acquisition rate and enable tracking of blood speckle. In our work, plane waves were used, providing a depth coverage of about 12 cm, which proved sufficient for ventricular flows as seen in Fig. 4.9 and 4.7. Diverging waves could in principle be used to cover a wider sector for each emission, but we were limited by the subaperture beamforming capabilities in the clinical matrix array transducer [16].

The proposed hybrid velocity estimator has several advancements compared to conventional block matching. Firstly, the autocorrelation method was used to exploit the phase information when estimating the radial velocity component, which increases precision and lower computational demands. Secondly, the 3D tracking kernel size (for 2D lateral block-matching) was linearly increasing with depth to compensate for the depth-dependent lateral resolution. Thirdly, the forward-backward tracking scheme described in Sec. 4.2.3 was used to minimize bias effects reported when using blood speckle tracking [18].

Normalized cross-correlation of RF data is an alternative to the autocorrelation method, but is substantially more computational demanding, especially in 3D. The autocorrelation approach with added block matching, however, approximates the full cross-correlation, and demonstrated robustness when using 3D kernels for dealiasing. To ensure robust results, the size of the dealiasing tracking kernels was chosen larger than for lateral tracking on the expense of processing time. Dealiasing of the flow signal proved to work robustly on both *in vitro* and *in vivo* data sets. This has also been reported in a similar 2D implementation [23]. Sufficient clutter suppression was important in this context. Combined with lateral 2D tracking, the 3D estimator showed strong agreement with the known velocity field in the rotating phantom setup in Fig. 4.6. Some underestimation was observed for higher velocity magnitudes, in particular for the lateral components. The elevation velocity estimates had a somewhat larger underestimation than in azimuth, probably caused by a reduced resolution due to the non-quadratic probe aperture. Alternative approaches combining Doppler velocity and lateral estimators have been described for tissue applications [24–26]. These methods are, however, not dependent on dealiasing.

The blood motion is sampled at the Doppler PRF (3-5kHz), and the displacement is thus very small between frames. Even for pathological jet flow the lateral displacement is subresolution for an adult cardiac imaging setup, considering $\sim 1 - 3$ mm lateral resolution depending on depth. Accurate results will thus depend highly on the subsample estimator. In this work simple parabolic fitting was used, and more sophisticated subsample interpolation techniques or optical flow approaches could improve results. Further, using higher tracking lags could improve results for lower velocities, although in the end limited by decorrelation. These aspects are focus for further work.

By restricting the 3D volume to a thick slice we could acquire continuous data from each sub-volume as illustrated in Fig. 4.2b. Continuous data improves clutter filtering and post-processing options, and adds flexibility for quantitative analysis including spectral Doppler calculation. Compared to the angle-corrected Doppler spectra, our hybrid velocity estimator and PC-MRI measurements showed good agreement throughout the cardiac cycle when also considering the difference in heart rate. However, some deviation in magnitude, especially during inflow was observed across the recordings. This could be caused by differences in the manually placed trace location, heart rate differences, averaging effects, clutter influence and signal loss due to clutter filtering. Also, in general, comparing with Doppler spectrum requires good angle correction which was only applied in-plane and kept constant through the cycle.

Global integrated parameters, such as EL and KE, have the advantage over local velocity traces of being less sensitive to registration errors when comparing multiple acquisitions. However, sources of error can still be related to differences in segmentation, which in this work was based on CFI masking based on tissue and blood detection for US, and fitting of an ellipsoid for the left ventricle for PC-MRI. Although deviations between the modalities (mainly in the systole) were present, both US and PC-MRI show EL and KE values within same order of magnitude which has been presented in the literature for 4D flow using PC-MRI [3]. The larger deviations between the modalities, where the ultrasound data seem to underestimated compared to PC-MRI, could be due to signal drop-outs (discussed in the next paragraph) and the methods limitation to estimate mean velocities affected by noise and clutter. Also, these parameters, specially energy loss, was found sensitive to spatial smoothing. Further validation is needed for these parameters to prove useful in a clinical setting.

Clutter filtering is a major challenge for ultrasound flow imaging. Attenuated blood signal leads to signal drop-outs observed throughout the cardiac cycle, while insufficient clutter filtering leads to artifacts and measurement bias [18] during filling and to underestimation during systole, as observed in Fig. 4.8. Adaptive spatio-temporal clutter filtering has shown potential for better blood signal recovery and should be further investigated in this context [27]. Alternatively, contrast agents could be utilized to enhance the blood signal and improve tissue signal suppression [28]. Another interesting approach to improve 4D flow estimation is more sophisticated post-processing of the data by including model-based regularization to smooth estimates, fill inn drop-out regions and correct tracking errors [14, 29].

The high temporal resolution obtained with ultrasound compared to PC-MRI is an advantage when imaging rapidly varying flow. The gating and averaging over many more heart cycles in PC-MRI results in very smooth and less dynamic velocity curves compared to ultrasound. The underestimation seen in the inflow from the a-wave for PC-MRI in Fig. 4.8 could be due to fluctuations in gating caused by variations in heart rate which ranged from 58 and 74 bpm, as reported in Table 4.2.

The slice-by-slice comparison in Fig. 4.7 showed comparable flow features in all views and time points, but some acquisition dependent differences were present. These observed differences are believed to be caused by the same factors as mentioned in the trace comparison, but in this context specially: differences in view orientation which were manually aligned, spatiotemporal averaging effects for the different acquisitions, and signal drop-outs in regions with low flow velocities due to clutter filtering. The latter can also cause drop-outs for high velocities, e.g. the aortic outlet, where the signal can be aliased into the stop band at $2 \times V_{\mathrm{Nyq}}$. The comparison with the other healthy volunteer in the supplementary Fig. 1 (available in the supplementary files /multimedia tab) showed both similarity and deviations in the flow fields, but comparable trends were found for all views. The variations can be both due to the same deviations found between US and PC-MRI, but different flow fields can also be present in different subjects.

The 3D volume acquisition enabled a 3D rendering of the flow fields, for instance by using short pathlines as shown in Fig. 4.9. Such intuitive visualizations could help reveal the 3D complexity of flow fields not obtainable from 2D imaging. In addition, as demonstrated in Fig. 4.7, arbitrary 2D views can be extracted for detailed flow analysis. Moving towards a 3D through-plane velocity measurement could also have valuable applications as demonstrated in PC-MRI. For instance for volume flow calculations which should be further investigated. The US 3D slice acquisition scheme could then be a useful acquisition scheme. Further, extracting other quantitative parameters as vortex formation characteristics, pressure gradient maps, and particle residence times has not been investigated in this work, but are used in the PC-MRI community today, and we believe they can be extracted from ultrasound 4D VFI.

While an initial demonstration and validation of 4D vector flow imaging using ultrasound has been shown, it is important to underline that ultrasound is a highly patient dependent imaging modality and further studies are needed to investigate the general feasibility for the presented method. If successful, we hope the method will provide useful information to aid in the understanding of cardiac patho-physiology, and eventually used in the diagnosis of diseased hearts, such as for hearts showing early signs of diastolic dysfunction (e.g. increased stiffness) or for dilated hearts with danger of thrombus formation.

4.6 Conclusions

In vivo intra-cardiac 4D ultrasound vector flow imaging was demonstrated, and showed good correspondence when compared to PC-MRI using both quantitative and qualitative analysis. The 4D ultrasound data was acquired non-invasively and without the use of contrast agents, using a modified clinical system providing real-time color flow imaging during acquisition. An optimized hybrid 3D velocity estimator combining dealiased Doppler estimation with lateral blood speckle tracking rendered the processing pipeline bedside applicable. While demonstrating the potential of 4D ultrasound vector flow imaging, clinical feasibility requires further evaluation.

References

[1] P. P. Sengupta, G. Pedrizzetti, P. J. Kilner, A. Kheradvar, T. Ebbers, G. Tonti, A. G. Fraser, and J. Narula, “Emerging trends in CV flow visualization,” *JACC Cardiovasc Imaging*, vol. 5, no. 3, pp. 305–316, 2012.

[2] P. Dyverfeldt, M. Bissell, A. J. Barker, A. F. Bolger, C.-J. Carlhäll, T. Ebbers, C. J. Francios, A. Frydrychowicz, J. Geiger, D. Giese, M. D. Hope, P. J. Kilner, S. Kozerke, S. Myerson, S. Neubauer, O. Wieben, and M. Markl, “4D flow cardiovascular magnetic resonance consensus statement,” *Journal of Cardiovascular Magnetic Resonance*, vol. 17, no. 1, p. 72, 2015.

[3] M. S. Elbaz, R. J. van der Geest, E. E. Calkoen, A. de Roos, B. P. Lelieveldt, A. A. Roest, and J. J. Westenberg, “Assessment of viscous energy loss and the association with three-dimensional vortex ring formation in left ventricular inflow: In vivo evaluation using four-dimensional flow MRI,” *Magnetic Resonance in Medicine*, vol. 77, no. 2, pp. 794–805, 2017.

[4] B. Dunmire, K. W. Beach, K. H. Labs, M. Plett, and D. E. Strandness, “Cross-beam vector Doppler ultrasound for angle-independent velocity measurements,” *Ultrasound in Medicine and Biology*, vol. 26, no. 8, pp. 1213–1235, 2000.

[5] J. A. Jensen and P. Munk, “A new method for estimation of velocity vectors,” *IEEE Transactions on Ultrasonics, Ferroelectrics, and Frequency Control*, vol. 45, no. 3, pp. 837–851, 1998.

[6] J. a. Jensen, “A new estimator for vector velocity estimation.,” *IEEE transactions on ultrasonics, ferroelectrics, and frequency control*, vol. 48, no. 4, pp. 886–894, 2001.

[7] K. C. Assi, E. Gay, C. Chnafa, S. Mendez, F. Nicoud, J. F. Abascal, P. Lantelme, F. Tournoux, and D. Garcia, “Intraventricular vector flow mapping - A Doppler-based regularized problem with automatic model selection,” *Physics in Medicine and Biology*, vol. 62, no. 17, pp. 7131–7147, 2017.

[8] C. Poelma, “Ultrasound Imaging Velocimetry: a review,” *Experiments in Fluids*, vol. 58, no. 1, pp. 1–28, 2017.

[9] L. N. Bohs, B. J. Geiman, M. E. Anderson, S. C. Gebhart, and G. E. Trahey, “Speckle tracking for multi-dimensional flow estimation,” *Ultrasonics*, vol. 38, no. 1-8, pp. 369–375, 2000.

[10] J. Jensen, S. Nikolov, A. C. H. Yu, and D. Garcia, “Ultrasound Vector Flow Imaging: II: Parallel Systems,” *IEEE Transactions on Ultrasonics, Ferroelectrics, and Frequency Control*, vol. 3010, no. c, pp. 1–1, 2016.

[11] J. A. Jensen, S. I. Nikolov, A. C. Yu, and D. Garcia, “Ultrasound Vector Flow Imaging-Part II: Parallel Systems,” *IEEE Transactions on Ultrasonics, Ferroelectrics, and Frequency Control*, vol. 63, no. 11, pp. 1722–1732, 2016.

[12] M. Correia, J. Provost, M. Tanter, and M. Pernot, “4D ultrafast ultrasound flow imaging: In vivo quantification of arterial volumetric flow rate in a single heartbeat,” *Physics in Medicine and Biology*, vol. 61, no. 23, pp. L48–L61, 2016.

[13] S. Holbek, K. L. Hansen, H. Bouzari, C. Ewertsen, M. B. Stuart, C. Thomsen, M. B. Nielsen, and J. A. Jensen, “Common Carotid Artery Flow Measured by 3-D Ultrasonic Vector Flow Imaging and Validated with Magnetic Resonance Imaging,” *Ultrasound in Medicine and Biology*, vol. 43, no. 10, pp. 2213–2220, 2017.

[14] A. Gomez, A. De Vecchi, M. Jantsch, W. Shi, K. Pushparajah, J. M. Simpson, N. P. Smith, D. Rueckert, T. Schaeffter, G. P. Penney, A. de Vecchi, M. Jantsch, W. Shi, K. Pushparajah, J. M. Simpson, N. P. Smith, D. Rueckert, T. Schaeffter, and G. P. Penney, “4D Blood Flow Reconstruction Over the Entire Ventricle From Wall Motion and Blood Velocity Derived From Ultrasound Data,” *IEEE Transactions on Medical Imaging*, vol. 34, no. 11, pp. 2298–2308, 2015.

[15] P. P. Sengupta, G. Pedrizetti, and J. Narula, “Multiplanar visualization of blood flow using echocardiographic particle imaging velocimetry,” *JACC: Cardiovascular Imaging*, vol. 5, no. 5, pp. 566–569, 2012.

[16] P. Santos, G. Haugen, L. Løvstakken, E. Samset, and J. D’hooge, “Diverging Wave Volumetric Imaging Using Subaperture Beamforming,” *Ultrason. Ferroelectr. Freq. Control. IEEE Trans.*, vol. 63, no. 12, pp. 2114–2124, 2016.

[17] O. Salvado and D. L. Wilson, “Removal of local and biased global maxima in intensity-based registration,” *Medical Image Analysis*, vol. 11, no. 2, pp. 183–196, 2007.

[18] S. Fadnes, M. Wigen, S. A. Nyrnes, and L. Lovstakken, “In vivo intracardiac vector flow imaging using phased array transducers for pediatric cardiology,” *IEEE Transactions on Ultrasonics, Ferroelectrics, and Frequency Control*, vol. 64, no. 9, pp. 1318 – 1326, 2017.

[19] S. Fadnes, I. K. Ekroll, S. A. Nyrnes, H. Torp, and L. Lovstakken, “Robust angle-independent blood velocity estimation based on dual-angle plane wave imaging,”

IEEE Transactions on Ultrasonics, Ferroelectrics, and Frequency Control, vol. 62, no. 10, pp. 1757–1767, 2015.

[20] C. Kasai, K. Namekawa, A. Koyano, and R. Omoto, "Real-Time Two-Dimensional Blood Flow Imaging Using an Autocorrelation Technique," *IEEE Transactions on Sonics and Ultrasonics*, vol. 32, no. 3, pp. 458–464, 1985.

[21] X. Lai, H. Torp, and K. Kristoffersen, "An extended autocorrelation method for estimation of blood velocity," 1997.

[22] M. Markl, A. Frydrychowicz, S. Kozerke, M. Hope, and O. Wieben, "4D Flow MRI," vol. 1036, pp. 1015–1036, 2012.

[23] I. Ekroll, J. Avdal, A. Swillens, H. Torp, and L. Lovstakken, "An extended least squares method for aliasing-resistant vector velocity estimation," 2016.

[24] A. R. Porras, M. Alessandrini, M. De Craene, N. Duchateau, M. Sitges, B. H. Bijnens, H. Delingette, M. Sermesant, J. D'Hooge, A. F. Frangi, and G. Piella, "Improved myocardial motion estimation combining tissue doppler and B-mode echocardiographic images," *IEEE Transactions on Medical Imaging*, vol. 33, no. 11, pp. 2098–2106, 2014.

[25] J. Poree, M. Baudet, F. Tournoux, G. Cloutier, and D. Garcia, "A Dual Tissue-Doppler Optical-Flow Method for Speckle Tracking Echocardiography at High-Frame-Rate," *IEEE Transactions on Medical Imaging*, vol. XX, no. X, pp. 1–11, 2018.

[26] V. Tavakoli, N. Bhatia, R. A. Longaker, M. F. Stoddard, and A. A. Amini, "Tissue doppler imaging optical flow (TDIOF): A combined b-mode and tissue doppler approach for cardiac motion estimation in echocardiographic images," *IEEE Transactions on Biomedical Engineering*, vol. 61, no. 8, pp. 2264–2277, 2014.

[27] C. Demené, T. Deffieux, M. Pernot, B. F. Osmanski, V. Biran, J. L. Gennisson, L. A. Sieu, A. Bergel, S. Franqui, J. M. Correas, I. Cohen, O. Baud, and M. Tanter, "Spatiotemporal Clutter Filtering of Ultrafast Ultrasound Data Highly Increases Doppler and fUltrasound Sensitivity," *IEEE Transactions on Medical Imaging*, vol. 34, no. 11, pp. 2271–2285, 2015.

[28] C. Tremblay-Darveau, R. Williams, P. S. Sheeran, L. Milot, M. Bruce, and P. N. Burns, "Concepts and Tradeoffs in Velocity Estimation with Plane-Wave Contrast-Enhanced Doppler," *IEEE Transactions on Ultrasonics, Ferroelectrics, and Frequency Control*, vol. 63, no. 11, pp. 1890–1905, 2016.

[29] T. Grønli, E. Smistad, S. A. Nyrnes, A. Gomez, and L. Lovstakken, "Reconstruction of in vivo flow velocity fields based on a rapid ultrasound image segmentation and B-spline regularization framework," *IEEE International Ultrasonics Symposium, IUS*, vol. 2016-Novem, pp. 1–4, 2016.

Chapter 5

Ultra-high frame rate cardiac imaging for simultaneous quantification of tissue and flow velocities

Morten Smedsrud Wigen[1], Solveig Fadnes[1], Annichen Søyland Daae[1], Sebastien Salles[1], Asbjørn Støylen[1,2], and Lasse Løvstakken[1]
[1] Department of Circulation and Medical Imaging, NTNU, Norway
[2] Dept. of Radiology and Nuclear Medicine, St. Olavs Hospital, Norway

The trade-off between temporal resolution and spatial coverage leads to the use of multiple imaging modes in echocardiography, e.g. M-mode, B-mode, color flow imaging (CFI), and PW-Doppler. This work describes a setup providing all modes simultaneously in a 3D slice, with a time resolution only limited by the pulse repetition frequency (PRF).
Plane wave transmission and ECG-gating was setup on a clinical scanner with a 2D matrix array transducer. By matching the number of transmissions and gating cycles (N=5-6), a continuous acquisition was achieved for each subvolume. The PRF was maximized (3.5-4kHz) to reproduce any pulsed imaging mode. Real-time CFI was available during examination.
Established as well as experimental imaging modes such as vector flow imaging (VFI), mechanical wave mapping (MWM), and intraventricular pressure gradients (IPG) could be calculated from one single multi-gated recording.
Compared with a clinical setup requiring five different recordings, similar spectral and image quality was observed for both tissue and flow information. Further, 3D VFI provided an out-of-plane motion estimate not previously available. The high temporal resolution allowed for MWM of the myocardium, reproducing characteristic waves previously described. Intraventricular pressure drops were calculated, where no significant difference was found for base-to-apex pressure drop trace when reducing frame rate to 100 Hz, while some differences were found when using VFI compared to CFI.
The proposed setup may simplify the acquisition of quantitative information in echocardiography, and provide new possibilities for studying simultaneous tissue and flow phenomena, although currently limited to patients with a steady heartbeat.

5.1 Introduction

Echocardiography can provide dynamic measurements of cardiac blood and tissue velocities, containing both regional and global information useful for diagnosis. The quality of these measurements are highly linked to and limited by the image acquisition setup, which conventionally either provides a single 1D measurement (e.g. pulsed wave (PW) Doppler, spectral tissue Doppler) with full spectral display, an M-mode measurement providing high temporal resolution along a line, or a cine-loop of 2D images of an average measurement (e.g. velocity in color flow and tissue Doppler) with limited frame rate. Conventionally, a trade-off between temporal and spatial coverage and resolution must be made, resulting in multiple modes being setup and acquired during an ultrasound examination. For real-time 3D echocardiography based on 2D matrix array transducers, ECG-gating is further required in order to provide acceptable volume sizes and frame rates.

Recently, a new imaging paradigm was introduced, which uncouples the link between temporal resolution and spatial coverage. By emitting broad unfocused (plane) or defocused (diverging) waves, and further exploit the increased parallel imaging capabilities of high-end ultrasound systems, it is possible to provide larger and even full spatial coverage for both linear and phased-array imaging for each emitted pulse. However, this comes at the expense of reduced penetration and signal-to-noise ratio (SNR) due to the lower pressures emitted. While it is possible to estimate detailed flow and tissue characteristics based on conventional image acquisition methods [1–4], these so-called *ultrafast ultrasound imaging* [5–7] approaches have enabled several new methods for quantifying blood and tissue properties. One example is the use of the increased time resolution and spatial coverage to more easily detect and measure the mechanical wave propagation along the heart walls [6–10], which can be related to myocardial stiffness.

Further, quantitative measurements in echocardiography are most often based on the Doppler principle, providing an angle-dependent, one-dimensional projection of the true blood or tissue displacement. For blood velocity measurements, vector flow imaging (VFI) methods have been enabled, and used to measure 2D and 3D blood velocities in the heart [11–14], demonstrating complex and secondary flow features previously only seen using PC-MRI methods [15].

Finally, *simultaneous* flow and tissue measurements enabled by both high temporal resolution and large spatial coverage could provide new insight and information about the cardiovascular system [16], where examples have been demonstrated for; vascular imaging [17], using multi-angle plane waves; cardiac imaging [18], using fully diverging waves; and on mice [19], using focused imaging with ECG-gating.

In this work, we describe new opportunities made possible using an ultra-high frame rate (UHFR) acquisition setup for 3D cardiac imaging, where simultaneous blood and tissue measurements are possible without frame rate restrictions, while maintaining good image quality. PW-spectra for both tissue and flow can be constructed from any spatial position retrospectively, and color flow images (CFI) and tissue velocity images (TVI) are available at several thousand frames per second, from where spatiotemporal (anatomic) M-modes can be drawn. In addition, angle-independent velocity estimates are obtained using speckle tracking for both flow and tissue. Utilizing either the high temporal resolution, angle-independent velocity estimates or the possibility to combine synchronous measurements from flow and tissue, we believe new cardiac measurement opportunities can be provided.

The UHFR acquisition is enabled using plane waves in combination with ECG-gating. Using a clinically approved 3D probe, a slice thickness was acquired (10 deg.), providing flexibility for view adjustments and estimation of the through-plane velocity components. The new acquisition setup is compared with conventional clinical modes, and used to demonstrate both clinically established as well as experimental measurements.

5.2 Methods

This section describes acquisition, processing and a selection of measurements made possible with the UHFR setup. Fig. 5.1 illustrates the acquisition of 3D thick-slice data, while Fig. 5.2 shows the post-processing possibilities. Relevant parameters for the acquisition setup and post-processing are given in Tables 5.1 and 5.2, respectively.

5.2.1 Data acquisition

For data acquisition, a GE Vivid E95 ultrasound scanner (GE Vingmed, Horten, Norway), with a 4V-D matrix array probe was used. The scanner was running on either the default clinical setup for reference measurements, or with a locally modified, clinically approved, mode for the experimental setup.

The frame rate for an ultrasound acquisition setup is limited by the imaging depth and number of transmit pulses emitted for a chosen scan width, conventionally related to the lateral resolution. Using unfocused beams give larger coverage for each transmitted pulse and hence fewer transmit pulses are needed compared to using focused beams. The consequences of less focused beams are, however, a reduction of image quality and SNR, which inevitably becomes a tradeoff.

Plane waves in combination with ECG-gating was utilized for the presented setup which, compared to using fully diverging waves, give improved SNR at the cost of using multiple heart cycles. One plane wave covers $\sim$ $10^\circ \times 10^\circ$ in azimuth and elevation direction, making N=5-6 beams adequate to cover a full width of an apical cardiac view of the left ventricle, including one or both heart walls.

By distributing the number of transmit directions into an equal number of heart cycles, each subvolume was sampled continuously at the pulse repetition frequency (PRF). Further, the six subvolumes were stitched together. Two consecutive heart beats were used to acquire high quality B-mode volumes at a lower frame rate, $\sim$ 75 frames-per-second (fps). Real-time beamforming and duplex color flow imaging of each subvolume at full frame rate was possible and provided a relevant preview of the data during acquisition. In summary, to acquire a full dataset, a total of seven-eight heart cycles were used, which typically is possible during one breath hold if needed. To compensate for minor variations in heart rate (HR) during the acquisition, the

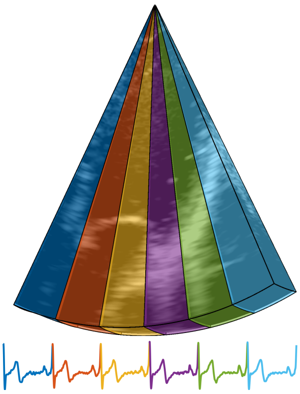

Figure 5.1: Illustration of the thick-slice data acquired with the ultra-high frame rate (UHFR) acquisition. Each color represents one heart cycle and subvolume, where six was needed to build up a full apical view of the left ventricle.

data were time-stretched in the diastolic phase. See Fig. 5.1 for an illustration of the acquired slice and subvolumes.

5.2.2 Post-processing pipeline

The UHFR data were stored as raw in-phase and quadrature (IQ) data for offline generation of all imaging modes, and the complete processing pipeline is illustrated in Fig. 5.2. Relevant parameters for all imaging modes are given in Table 5.1.

Clutter filtering

The first processing step is attenuation of clutter signals originating from reverberation and off-axis structures [20], which contributes to errors and underestimation for both blood and tissue velocity measurements, but in particular for blood velocities due to the low blood signal magnitudes compared to tissue [21]. The separation was achieved by using a high-pass filter (band-pass for TVI data) along the temporal dimension, exploiting the differences in (radial) velocities between flow and tissue, and hence a difference in Doppler frequency shift [21].

With spectral displays, some clutter can be present without degrading the velocity spectrum information, as an operator visually still can distinguish desired from undesired signals. Mean velocity estimators, however, as TVI and CFI, can strongly underestimate velocities when remaining clutter is present. The different modes hence use dedicated clutter filters, and the choice of filter is in the end a trade-off between sensitivity to low velocities and clutter artifacts. Fig. 5.3 shows how the velocity spectrum varies depending on the mode, and how the mean velocities (red curves) are affected by the degree of clutter. It also shows how the UHFR sequence can cover a full spectrum of velocities. By exploiting the continuous frame acquisition achieved in our UHFR setup, we could design clutter filters with improved transition and stop-band

Table 5.1: Transmit/receive parameters for the experimental and reference recordings.

	Experimental	**Reference**				
	UHFR	CFI	TVI	Color M-mode	PW-Doppler flow	PW-Doppler tissue
Center frequency, [MHz]	2.9	2.2	2.5	2.2	2.0	2.6
Sample volume, [mm]	1.0	1.0	1.0	1.0	5.0	6.0
Packet size, [# samples]	continuous	12	3	8		
Pulse repetition frequency, [kHz]	3.5	3.5	1.0	3.5	4.5	1.7
V_{Nq}, [cm/s]	46	61	15	61	87	25
Time resolution, [samples/second]	——— 〃 ———	23	133	278	——— 〃 ———	——— 〃 ———
Sector size - azimuth, elevation	50° × 10°	41° × 0°	65° × 0°			
Imaging depth, [cm]	13	11	12	11	9.1	9.5
# MLAs - azimuth×elevation	12 × 10	n/a	n/a			
# beats for ecg-gating	$7-8$	1	1			
Heart rate, [beats/min]	61 ± 1.0	69	76	71	73	67

Table 5.2: Post processing parameters of the UHFR data

	Experimental						
	VFI	CFWI	CFI	TVI	Color M-mode	PW-Doppler flow	PW-Doppler tissue
Butterworth filter order	8	4	8	4	8	8	4
Filter cut-off	Dynamic	4	13	.5(20)	13	11	.5
Smoothing type	Gaussian	box(s)/Butter.(t)	box	box	-	radial	radial
Spatial smoothing	9, 9, 9 mm	2, 2, 1 px	1, 1, 1 px	3, 3, 1 px	-	5 mm	6 mm
Temporal smoothing	50 msec	7 msec	6 msec	6 msec	6 msec	-	-

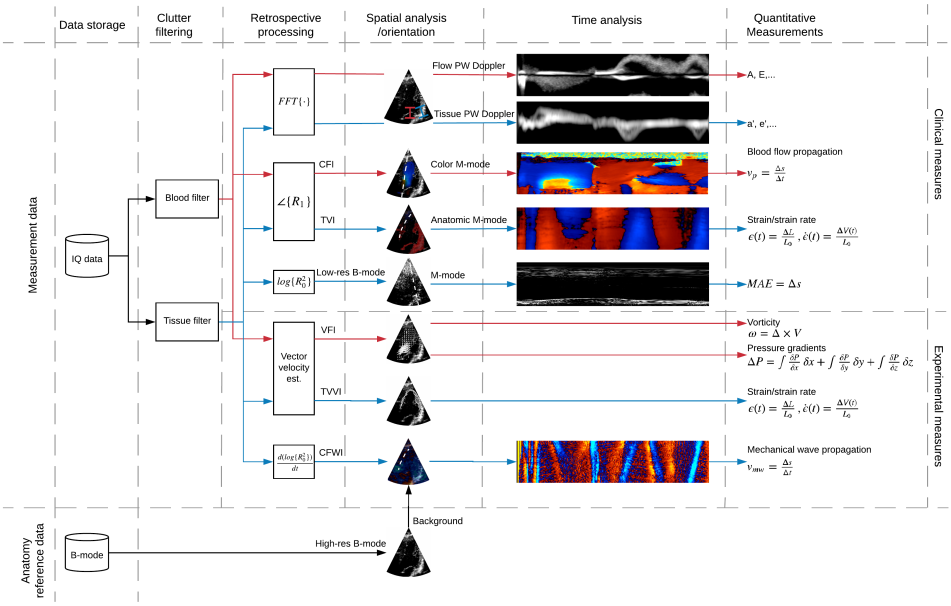

Figure 5.2: The processing pipeline illustrates how one dataset can be used for multiple modes, including 2D images, spatiotemporal images and Doppler spectra, from where different quantitative measurements can be extracted.

characteristics, particularly important for CFI and VFI. In this work, Butterworth filters were adapted and applied for the different modes, further details are provided in Table 5.1. For VFI data, a time varying filter cut-off was applied, adapted to the tissue-velocities of the raw data, as described in [13].

Retrospective processing

With continuous data acquired at a frame rate equal to the PRF (3-5kHz for adult cardiac imaging), PW-Doppler spectra can be calculated at any spatial position for both flow or tissue [22]. This was here done using the Welch approach with a clutter filter and window length suitable for either blood or tissue analysis. Mean velocity estimation was further done by using a sliding window approach, generating CFI or TVI data using the autocorrelation method [23]. Reduced quality B-mode images could also be made from the UHFR data, which was used to generate (anatomical) M-modes at a high temporal resolution. The separate high-resolution B-mode sequence served as anatomic reference images, useful for orientation and placement of (anatomical) M-mode lines and PW sample volumes.

Acceleration maps based on TVI data has been a common way for investigating mechanical wave propagation. A different approach was used in this work, termed

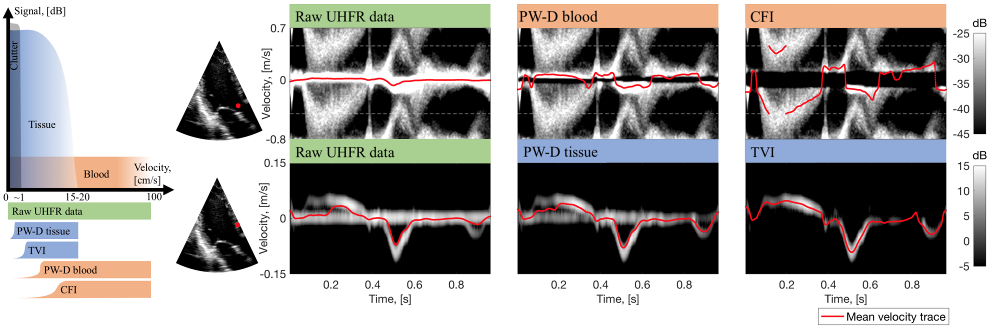

Figure 5.3: Tissue and blood separation. The raw UHFR data are filtered can be used for wither spectral or mean velocity representation, and is filtered accordingly. To extract correct mean estimates(red curves), as used for CFI and TVI, the signals must be filtered harder than what needed for spectral inspection, at the cost of loss of low-velocities.

clutter filter wave imaging (CFWI) [24], which has been shown to be more sensitive for detecting the small wave displacements in the myocardium caused by physiological events.

Doppler-based methods are limited to providing radial velocity estimates, and speckle tracking (ST) was here utilized to also estimate the lateral velocity components [25]. ST is clinically available for measuring tissue displacement from B-mode images [26], but is an experimental approach for estimating the lateral velocity components for blood [27]. Blood speckle tracking (BST) is more challenging due to lower SNR, clutter filter dropouts, and potentially high velocities resulting in rapid speckle decorrelation. BST was recently demonstrated for adult cardiac applications in 3D [13], where Doppler and speckle tracking velocity estimation is combined to reduces variance and computational demands, which was also used in this work. Spatial smoothing was done with a truncated (one std.) Gaussian kernel of dimensions 9 mm^3 and 50 ms, where spatial and temporal smoothing was applied subsequent. Due to the high PRF relative to the tissue motion, a higher lag (10) was used for tissue speckle tracking.

5.2.3 Blood flow measurements

PW-Doppler spectra enables the most accurate quantification of blood velocities using ultrasound. Standard measurements include peak velocities through the left ventricular outflow tract (LVOT) during systole, and through the mitral annulus during diastole. These three peak velocity measurements of blood are denoted as S, E and A, respectively.

From a three-dimensional blood velocity vector field, other hemodynamic properties can be extracted. The Navier-Stokes equation for incompressible fluids describing the bloods behaviour in an environment, and is given by:

$$\frac{\delta\vec{v}}{\delta t} + (\vec{v}\cdot\nabla)\vec{v} - \frac{\mu}{\rho}\nabla^2\vec{v} = -\frac{1}{\rho}\nabla P \tag{5.1}$$

Multiple flow properties can be extracted based on these relations. By integrating the inertia terms (first and second term in (5.1)) along a streamline path,

$$\Delta P = \sum_{i=1}^{3}\int_{path}\frac{\partial P_i}{\partial i}ds, \tag{5.2}$$

where

$$-\frac{\partial P_i}{\partial i} = \rho(\frac{\partial v_i}{\partial t} + v_x\frac{\partial v_i}{\partial x} + v_y\frac{\partial v_i}{\partial y} + v_z\frac{\partial v_i}{\partial z}), \tag{5.3}$$

the pressure difference between a start and end point can be calculated [28]. Intraventricular pressure gradients (IPG) have previously been calculated using color M-mode [3, 29–31], by assuming the flow to follow the scan lines. ΔP can then be approximated from the following relation

$$\Delta P \approx -\rho\int(\frac{\partial v_D}{\partial t} + v_D\cdot\frac{\partial v_D}{\partial s}). \tag{5.4}$$

While the actual streamline of flow will constantly change during a cardiac interval, the integration path was kept constant for the IPG measurements, as in previous work [28, 32].

Other hemodynamic properties, such as vorticity, energy loss and kinetic energy, can further be calculated when a velocity vector field is provided. Fig. 5.2 shows briefly how they can be extracted from the UHFR data. These properties are, however, not investigated further in this work.

5.2.4 Tissue measurements

Peak tissue velocities are used as indices for cardiac function. Peak tissue amplitudes from the basal wall, are measured from spectral tissue-Doppler during systole, the e-wave and the a-wave. These velocities are denoted as S', e' and a'.

The estimation of mechanical wave propagation velocities was calculated from anatomic M-mode lines from the CFWI data, positioned along the cardiac walls. We here used the spatiotemporal peak method [33] from manually chosen time intervals. Due to heart wall motion, the same M-mode line segment cannot be used throughout the cardiac cycle, and was in this work manually drawn for each investigated time interval.

As pointed out in Fig. 5.2 other tissue properties can potentially also be extracted from the same data, e.g. strain, strain rate, and mitral annular excursion (MAPSE).

5.3 Results

The described setup resulted in a frame rate of 3500-4000 volume frames per second, with a slice *thickness* of $\sim$ 10°, covering a full apical view of the left ventricle. The slice thickness allowed some flexibility for view selection, and also through-plane motion estimation. Further details regarding the acquisition setup is found in Table 5.1. Results presented in Fig. 5.4 and 5.7 are from the same subject and recording, while Fig. 5.5 and Fig. 5.6 are of separate subjects.

For quality comparison between the experimental UHFR setup and the conventional clinical setup, a healthy 32-year-old female volunteer was imaged by an experienced medical doctor with both setups. Under the clinical acquisition multiple recordings were acquired: PW-Doppler for tissue and flow, and TVI, CFI and color M-mode. In contrary, all modes were processed from one acquisition using the experimental setup. Fig. 5.4 shows a side-by-side comparison of the two modes, where the left column contains the reference data and each row corresponds to individual recordings, and the right column contains data from the single experimental acquisition. All clinical recordings were acquired before the experimental, resulting in potential deviations in views, trace positions and heart rate (HR) between the modes. The 2D image frames are related to the PW-Doppler axis (white dashed lines), for tissue and flow respectively. However, as the reference modes are acquired separately, this is manually adjusted, in contrast to the results from the experimental setup, where all modes have the same time axis. The same velocity scales, averaging and dynamic ranges are used in the figures. Equal gain and filter cut-offs could, however, not be obtained due to limited available parameters from the clinical setup.

The tissue PW-Doppler spectra reveals the same trends during systole and diastole. In- and out-of-plane motion is most probably causing the variable signal strength seen in the experimental setup. The TVI images, from peak systolic annular velocity, S', and peak velocities during the two filling phases, a' and e', appear comparable in image quality and trends, but the clinical recordings include aliasing due to the lower V_{Nq}.

For the blood PW-Doppler there was an elevated HR of 73 bpm in the reference recording, resulting in higher peak velocities during diastole, compared to the experimental recording with a HR of 61 bpm. The flow patterns seen with CFI shows deviations in imaging view, but both acquisitions capture the same events. Looking at color M-mode, similar flow fields can be observer, however, clutter influence might cause the blue flashes during diastole, which is more present in the experimental data.

Table 5.3 contains peak blood and tissue velocities extracted from the PW-Doppler spectra for the two setups. From where the E/A and E/e' ratio was calculated to be 1.9 and 6.7, respectively, for the reference setup, and 2.8 and 6.2 for the experimental setup.

Fig. 5.5 shows 2D time frames, spatiotemporal maps and spectrograms extracted from a single dataset acquired with the UHFR setup. The dataset was recorded on a 28-year-old healthy male volunteer, by an experienced medical doctor. The two leftmost panels display CFI and TVI data with the in-plane vector velocity estimates drawn on top as white arrows, as acquired from speckle tracking. The temporal frame positions are marked on the ECG-trace on the top right plot, and below spatiotemporal

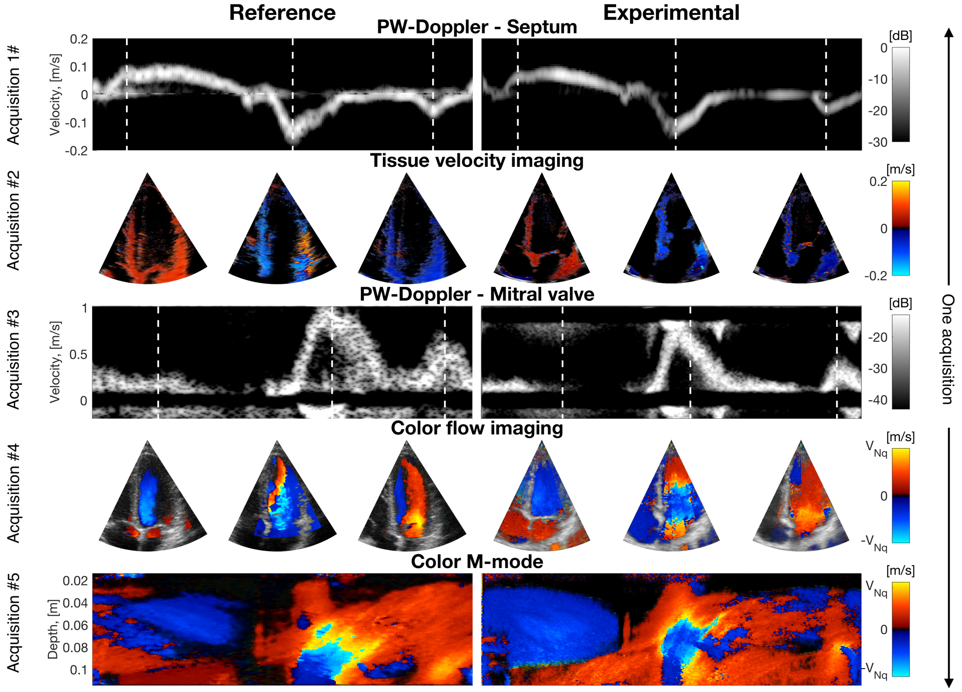

Figure 5.4: Comparison between data acquired with a clinical setup (left) and the experimental setup (right). The clinical data have one recording for each mode, while the experimental modes are all from one single recording.

Table 5.3: Tissue and flow velocities from PW-Doppler.

	S', [m/s]	E, [m/s]	e', [m/s]	A, [m/s]	a', [m/s]	E/A	E/e'
Reference	0.075	0.87	0.13	0.46	0.060	1.9	6.7
Experimental	0.081	0.74	0.12	0.26	0.054	2.8	6.2

images and PW spectra, all with a common temporal axis with the corresponding 2D frames instances plotted as white lines. The first frame shows outflow during systole through the left ventricular outflow tract (LVOT) as the heart contracts. The VFI images show a direction of the flow in accordance with the orientation of the LVOT, not affected by the aliasing seen in the CFI images. The next time frame (2) shows inflow and relaxation of the heart muscle during peak diastole, followed by diastasis (3) with lower velocities. The last frame (4) is from late diastole during the a-wave, showing inflow and expansion of the heart volume.

Pressure drop curves from base to apex in the left ventricle was calculated using three-directional VFI-data from a 65 year-old male volunteer. The two top right plots in Fig. 5.6 show PW-Doppler of tissue and flow, respectively, with the intraventricular

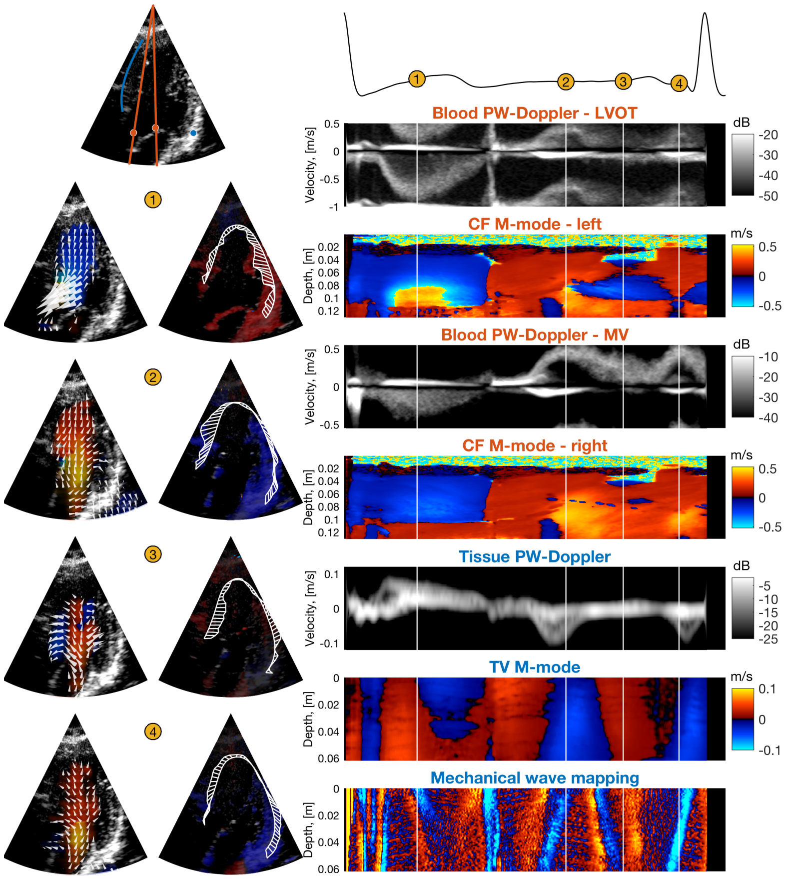

Figure 5.5: Figure showing different modes calculated from one acquisition. The top right image shows locations for the temporal images to the right: red line shows color M-mode position, red dot is the blood PW Doppler. The blue line is for anatomic tissue M-mode and mechanical wave mapping. The blue dot represents the spatial position for tissue PW Doppler. The two leftmost columns shows image data for flow and tissue, respectively, with color/tissue Doppler background and vector velocity estimates drawn as arrows and lines.

pressure gradient (IPG) curves below. The IPG curves from VFI data were calculated with different time resolutions, by decimation, to investigate the effect of frame rate, also with temporal smoothing applied after decimation. The red IPG curve is calculated from Doppler data alone, with the finest time resolution. The bottom 2D-images show corresponding VFI data from the marked time positions (vertical lines), plotted as arrows for qualitative representation of the blood flow. The arrows also supported the choice of integration path for the IPG calculations. The IPG curves show time resolution dependencies up to ~ 100 fps. With finer time resolution, only minor deviations are observed between the curves. Looking at the pressure drop curve with the finest time resolution, using VFI data, reveals a negative pressure drop of ~ -3 mmHg from base to apex, caused by pressure reduction in apex, at the beginning of diastole as the e-wave is initiated during ventricular relaxation. The pressure drop curve is zero about the same time as peak flow is reached, but continues to rise to a maximum of ~ 1 mmHg difference at the end of the e-wave. Further, the pressure difference is gradually equalized through the diastasis, before a negative pressure difference, ~ -1 mmHg, is obtained at the start of atrial contraction, caused by an increase in pressure from the base, as the atrium contracts. Peak pressure drop reaches ~ 4 mmHg right after peak velocity during the a-wave.

Mechanical wave mapping (MWM), processed with the CFWI method, is visualized as an anatomic M-mode from a path along the septum wall, shown in Fig. 5.7. Two temporal segments are here extracted; from mitral valve closure and during atrial systole. While the line segment is manually chosen, the velocity regression lines were automatically calculated based on minimum values within the segment window, as described in [33]. The wave propagation velocity was estimated to be 11.9 and 1.90 m/s, respectively, with R^2 values of 0.77 and 0.70. The bottom two columns show each segment with corresponding 2D-images, where the red circles follow the estimated propagation path and correspond between the M-mode and 2D images.

5.4 Discussion

A 3D acquisition setup with ultra-high frame rate (UHFR), 3500-4000 vps, has been presented, which provided retrospective analysis of the most used imaging modes in echocardiographic examinations, such as blood and tissue PW-Doppler, color flow imaging (CFI) and tissue velocity imaging (TVI) and generation of anatomic M-modes, from a single recording. The UHFR-setup gave similar quality as recordings obtained from a conventional clinical setup for the different modes. The UHFR-setup further enabled new quantification opportunities through more recent and experimental measurements for flow and tissue properties, which depend on higher frame rates than what is available in conventional imaging modes.

As shown in previous work [13], the slice thickness enables quantification of the through-plane velocity component with speckle tracking, and was in this work incorporated in the intraventricular pressure gradient (IPG) calculations. Elevational smoothing was also applied to reduce variance in measurements, see Table 5.2. Other interesting aspects could also have been investigated using these data, such as volume

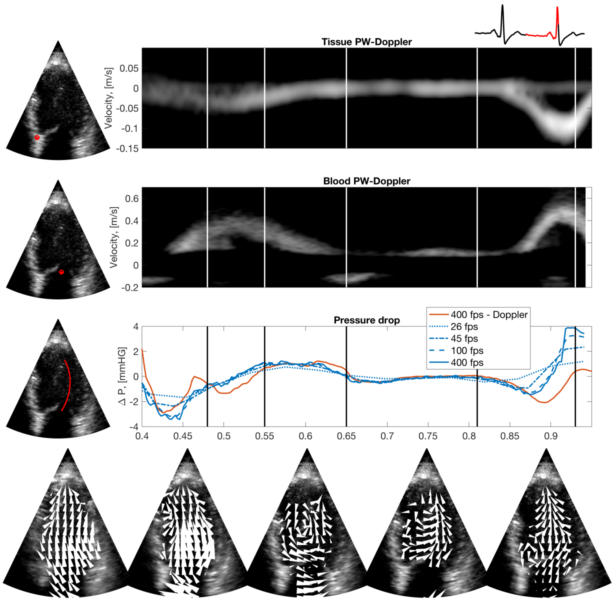

Figure 5.6: Left ventricle diastolic pressure drops (base to apex), calculated from VFI data, in the third plot from the top, in addition to PW spectra from tissue and blood in the top plots. The bottom images show VFI data visualized during different parts of the diastolic phase.

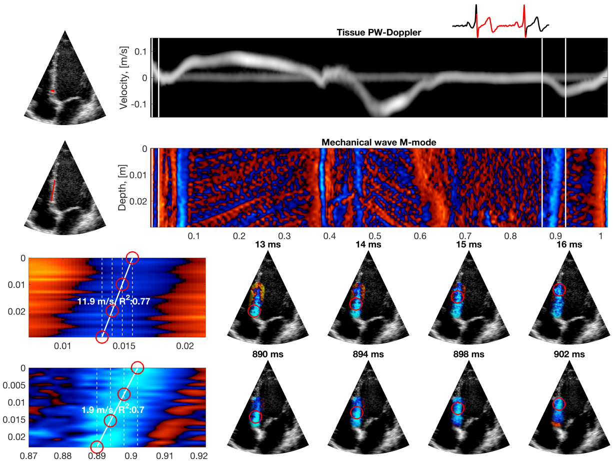

Figure 5.7: Mechanical wave mapping in the septum calculated with the CFWI method. Two parts are emphasized: mitral valve closure and the a-wave, with estimated wave propagation velocities.

flow or cardiac torsion, but is considered further work. The thick slice data also enables smaller adjustments of the imaging view retrospectively, including flexibility for PW-Doppler sample volumes placement in three directions which can be important in practise.

Similar values were obtained for the E/e' with 7.4% deviation from the reference, while for the E/A, a deviation of 47% was found. The large deviation in the E/A value is due to the low a-wave velocity measured in the experimental setup, which here was caused by misalignment with the inflow. This could indicate that extra care must be taken for view alignment for the experimental recordings, or that it is difficult to obtain one view optimal for all modes and measurements.This aspect needs further evaluation. Intraventricular pressure gradient (IPG) estimation using ultrasound, has previously only been estimated using color M-mode [3, 29–31], due to the need of high temporal resolution and that the IPG calculations have approximated the flow to follow the scanline when using Doppler measurements. With the UHFR setup, path selection can be done retrospectively and IPG calculated from the three-directional VFI data. While further validation is needed, this approach could provide a higher accuracy for IPG measurements as less assumptions are made. Fig. 5.6 demonstrates the need for high frame rates for IPG calculations. This has also been reported from PC-MRI [28], however, for PC-MRI a frame rate of 23 fps was found sufficient, whereas in this work we found it beneficial with frame rates as high as > 100 vps to capture all details, though without a comparable reference value. The required temporal resolution for IPG measurement also depends on physiological factors, such as the flow acceleration in our case, where a strong a-wave lead to a high IPG during atrial contraction, normal for elderly subjects.

Mechanical wave mapping in the myocardium was demonstrated in Fig. 5.7. As these waves travel at a fast pace, a fine time resolution is crucial to capture the events ($>$1 kHz). The propagation velocity values measured was within the range of what has been reported previously [9], but the regression R^2 values implies a degree of uncertainty. Mechanical waves originating from the aortic valve closure has previously been used to evaluate myocardial stiffness, and could be observed at ~ 380 ms in the MWM in Fig. 5.7, but was not found suitable for a linear regression fit in the given imaging view.

Using plane waves for the UHFR setup reduces image contrast and increases clutter level, as well as measurement SNR. While the quantification of velocities reveal comparable quality between focused and planar beams, as shown in Fig. 5.4, the image quality of the raw B-mode and M-mode were low, which is why a complementary high resolution B-mode was acquired consecutively. By using broader transmit pulses, the UHFR-setup may thus be more less applicable to patients with challenging imaging conditions (both image contrast and penetration). Blood speckle tracking is in general sensitive to clutter [27] and calculations based on VFI might be particularly limited under such conditions. In general, as VFI relies on clutter filtering in the same way as CFI, drop-out regions will be present. In this context, better measurement regularization schemes might be beneficial to reconstruct dropout regions, and reduce variance and bias. Using contrast agents, might be an alternative approach to reduce, or remove, the negative effects of clutter filtering, and might be necessary on patients with challenging imaging conditions.

As seen in Table 5.1, the different clinical modes have transmit settings such as frequency, sample volume and packet size tuned for the individual modes. Different transmit pulses were not used for the all-in-one acquisition setup used here. However, by using a single broad-band pulse and different receive filter settings this could also be approached [34], and is subject for further work.

ECG-gating was a necessity for the all-in-one setup to achieve high frame rates while maintaining good image quality. By using diverging waves, similar frame rates and spatial coverage can be provided without ECG-gating. This approach has recently been demonstrated for 2D and 3D cardiac imaging and quantification of both tissue and blood velocities [18, 22, 35, 36], and may be more suited for patients with uneven heart beats, ventricular dyssynchrony, or with atrial fibrillation. This was however not currently possible to test using the commercial 2D matrix array transducer due to the in-probe beamforming. However, as image quality degrades and clutter levels increase significantly using single diverging waves, coherent compounding of several transmissions is usually required, and should preferably be implemented using motion compensation [37]. This will however reduce the effective Doppler-PRF which is crucial for blood flow imaging.

With ECG-gating the different subvolumes are further not acquired simultaneously, and there can hence be minor deviations in timing between them. In this work, this is compensated for by linearly stretching the diastolic phase. Despite the compensation, this should be kept in mind when looking at physiological events crossing the different subvolumes. For the MWM the line selection was here chosen within one single subvolume.

While many studies have developed specialized setups for investigation of tissue *or* flow measurements, the thick-slice setup seeks to enable simultaneous measurements. This can for instance be used to investigate the coupling and interaction between myocardial and hemodynamic properties. While this initially will be useful when studying basic cardiac physiology, it may also lead to new clinical information in the future. Current experimental imaging modes such as VFI and MWM can also provide new information in itself. Such as measuring changes or disturbances of the intraventricular vortex or the redistribution of flow forces, which is hypothesized to be a potential driving force for left ventricular remodeling [16]. And provide new markers of tissue stiffness which can be useful in both ischemic heart disease, as well as for quantifying the development of myocardial fibrosis. Finally, when the proper data logistics and workflow is integrated into a clinical scanner, the single-recording approach may become a practical tool that saves time and increases measurement reproducibility in general.

Patient feasibility studies using the proposed setup will be important in this setting to map clinical applicability. This is the subject for further work in the near future.

5.5 Conclusions

A single acquisition setup providing ultra-high frame rates used for both new and conventional cardiac imaging modes has been proposed and demonstrated. New measurements were further enabled by the combination of high temporal resolution and wide spatial coverage. From the examples provided, the proposed setup showed potential for investigation of rapid physiological events using vector flow imaging, myocardial mechanical wave propagation and intraventricular pressure gradients. The acquisition setup also provides a unique opportunity for simultaneous assessment of tissue and blood velocities, which can be used to investigation basic cardiac physiology as well as new clinical markers.

References

[1] D. Garcia, J. C. del Álamo, D. Tanné, R. Yotti, C. Cortina, É. Bertrand, J. C. Antoranz, E. Pérez-David, R. Rieu, F. Fernández-Avilés, and J. Bermejo, “Two-Dimensional Intraventricular Flow Mapping by Digital Processing Conventional Color-Doppler Echocardiography Images,” *IEEE Transactions on Medical Imaging*, vol. 29, pp. 1701–1713, oct 2010.

[2] G. R. Hong, G. Pedrizzetti, G. Tonti, P. Li, Z. Wei, J. K. Kim, A. Baweja, S. Liu, N. Chung, H. Houle, J. Narula, and M. A. Vannan, “Characterization and Quantification of Vortex Flow in the Human Left Ventricle by Contrast Echocardiography Using Vector Particle Image Velocimetry,” *JACC: Cardiovascular Imaging*, vol. 1, no. 6, pp. 705–717, 2008.

[3] J. Bermejo, J. C. Antoranz, R. Yotti, M. Moreno, and M. A. García-Fernández, “Spatio-temporal mapping of intracardiac pressure gradients. A solution to Euler's equation from digital postprocessing of color Doppler M-mode echocardiograms,” *Ultrasound in Medicine and Biology*, vol. 27, no. 5, pp. 621–630, 2001.

[4] H. Kanai and Y. Koiwa, “Myocardial rapid velocity distribution,” *Ultrasound in Medicine and Biology*, vol. 27, no. 4, pp. 481–498, 2001.

[5] M. Cikes, L. Tong, G. R. Sutherland, and J. D'Hooge, “Ultrafast cardiac ultrasound imaging: Technical principles, applications, and clinical benefits,” *JACC: Cardiovascular Imaging*, vol. 7, no. 8, pp. 812–823, 2014.

[6] M. Tanter and M. Fink, “Ultrafast Imaging : a new paradigm in biomedical Ultrasound,” *IEEE Transactions on Ultrasonics, Ferroelectrics and Frequency Control*, vol. 61, no. 1, p. 10, 2014.

[7] B. Brekke, L. C. Nilsen, J. Lund, H. Torp, T. Bjastad, B. H. Amundsen, A. Stoylen, and S. A. Aase, “Ultra-high frame rate tissue doppler imaging,” *Ultrasound in Medicine and Biology*, vol. 40, no. 1, pp. 222–231, 2014.

[8] M. Pernot, K. Fujikura, S. D. Fung-Kee-Fung, and E. E. Konofagou, “ECG-gated, Mechanical and Electromechanical Wave Imaging of Cardiovascular Tissues In Vivo,” *Ultrasound in Medicine and Biology*, vol. 33, no. 7, pp. 1075–1085, 2007.

[9] H. Kanai, “Propagation of Vibration Caused by Electrical Excitation in the Normal Human Heart,” *Ultrasound in Medicine and Biology*, vol. 35, no. 6, pp. 936–948, 2009.

[10] S. Salles, H. Liebgott, D. Garcia, and D. Vray, “Full 3-D transverse oscillations: A method for tissue motion estimation,” 2015.

[11] S. Holbek, K. L. Hansen, N. Fogh, R. Moshavegh, J. B. Olesen, M. B. Nielsen, and J. A. Jensen, “Real-time 2-D Phased Array Vector Flow Imaging,” *IEEE Transactions on Ultrasonics, Ferroelectrics, and Frequency Control*, vol. 65, no. 7, pp. 1205–1213, 2018.

[12] S. Fadnes, S. Nyrnes, M. Wigen, E. Tegnander, and L. Lovstakken, “Detailed flow visualization in fetal and neonatal hearts using 2-D speckle tracking,” in *IEEE International Ultrasonics Symposium, IUS*, vol. 2016-Novem, 2016.

[13] M. S. Wigen, S. Fadnes, A. Rodriguez-Molares, T. Bjastad, M. Eriksen, K. H. Stensaeth, A. Stoylen, and L. Lovstakken, “4D Intracardiac Ultrasound Vector Flow Imaging -Feasibility and Comparison to Phase-Contrast MRI,” *IEEE Transactions on Medical Imaging*, pp. 1–1, 2018.

[14] K. C. Assi, E. Gay, C. Chnafa, S. Mendez, F. Nicoud, J. F. Abascal, P. Lantelme, F. Tournoux, and D. Garcia, “Intraventricular vector flow mapping - A Doppler-based regularized problem with automatic model selection,” *Physics in Medicine and Biology*, vol. 62, no. 17, pp. 7131–7147, 2017.

[15] M. Markl, P. J. Kilner, and T. Ebbers, “Comprehensive 4D velocity mapping of the heart and great vessels by cardiovascular magnetic resonance,” *Journal of Cardiovascular Magnetic Resonance*, vol. 13, no. 1, p. 7, 2011.

[16] M. Dal Ferro, D. Stolfo, V. De Paris, P. Lesizza, R. Korcova, D. Collia, G. Tonti, G. Sinagra, and G. Pedrizzetti, “Cardiac fluid dynamics meets deformation imaging,” *Cardiovascular Ultrasound*, vol. 16, no. 1, pp. 1–10, 2018.

[17] I. K. Ekroll, A. Swillens, P. Segers, T. Dahl, H. Torp, and L. Lovstakken, “Simultaneous quantification of flow and tissue velocities based on multi-angle plane wave imaging,” *IEEE Transactions on Ultrasonics, Ferroelectrics, and Frequency Control*, vol. 60, no. 4, pp. 727–738, 2013.

[18] J. Provost, C. Papadacci, J. E. Arango, M. Imbault, M. Fink, J. L. Gennisson, M. Tanter, and M. Pernot, “3D ultrafast ultrasound imaging in vivo,” *Physics in Medicine and Biology*, vol. 59, no. 19, pp. L1–L13, 2014.

[19] J. Luo and E. E. Konofagou, “Imaging of Wall Motion Coupled With Blood Flow Velocity in the Heart and Vessels in Vivo: A Feasibility Study,” *Ultrasound in Medicine and Biology*, vol. 37, no. 6, pp. 980–995, 2011.

[20] M. A. Lediju, M. J. Pihl, J. J. Dahl, and G. E. Trahey, “Quantitative assessment of the magnitude, impact and spatial extent of ultrasonic clutter,” *Ultrasonic Imaging*, vol. 30, no. 3, pp. 151–168, 2008.

[21] S. Bjaerum, H. Torp, and K. Kirstoffersen, “Clutter filter design for ultrasound color flow imaging,” *Ieee Transactions on Ultrasonics Ferroelectrics and Frequency Control*, vol. 49, no. 2, pp. 204–216, 2002.

[22] B. F. Osmanski, D. Maresca, E. Messas, M. Tanter, and M. Pernot, “Transthoracic ultrafast Doppler imaging of human left ventricular hemodynamic function,” *IEEE Transactions on Ultrasonics, Ferroelectrics, and Frequency Control*, vol. 61, no. 8, pp. 1268–1275, 2014.

[23] C. Kasai, K. Namekawa, A. Koyano, and R. Omoto, “Real-Time Two-Dimensional Blood Flow Imaging Using an Autocorrelation Technique,” *IEEE Transactions on Sonics and Ultrasonics*, vol. 32, no. 3, pp. 458–464, 1985.

[24] S. Salles, S. A. Aase, T. Bjastad, L. Løvstakken, and H. Torp, “Clutter filter wave imaging (CFWI): a new way to visualize and detect mechanical waves propagation,” in *EEE International Ultrasonics Symposium (IUS)*, (Washington, DC), 2017.

[25] L. N. Bohs and G. E. Trahey, “A Novel Method for Angle Independent Ultrasonic Imaging of Blood Flow and Tissue Motion,” *IEEE Transactions on Biomedical Engineering*, vol. 38, no. 3, pp. 280–286, 1991.

[26] T. H. Marwick, Y. Cheuk-Man, and J. P. Sun, *Myocardial Imaging: Tissue Doppler and Speckle Tracking. Oxford.* Oxford, UK: Wiley-Blackwell, 2007.

[27] S. Fadnes, M. Wigen, S. A. Nyrnes, and L. Lovstakken, “In vivo intracardiac vector flow imaging using phased array transducers for pediatric cardiology,” *IEEE Transactions on Ultrasonics, Ferroelectrics, and Frequency Control*, vol. 64, no. 9, pp. 1318 – 1326, 2017.

[28] R. B. Thompson and E. R. McVeigh, “Fast measurement of intracardiac pressure differences with 2D breath-hold phase-contrast MRI,” *Magnetic Resonance in Medicine*, vol. 49, no. 6, pp. 1056–1066, 2003.

[29] N. L. Greenbergl, P. M. Vandervoortz, and J. D. Thomas, “Estimation of Diastolic Intraventricular Pressure Gradients from Color Doppler M-mode Spatiotemporal Velocities: Analytical Euler Equation Solution,” *Computers in Cardiology*, pp. 8–11, 1994.

[30] N. L. Greenberg, P. M. Vandervoort, M. S. Firstenberg, M. J. Garcia, and J. D. Thomas, “Estimation of diastolic intraventricular pressure gradients by Doppler M-mode echocardiography.,” *American journal of physiology. Heart and circulatory physiology*, vol. 280, no. 6, pp. H2507–15, 2001.

[31] R. Yotti, J. Bermejo, M. M. Desco, J. C. Antoranz, J. L. Rojo-Álvarez, C. Cortina, C. Allué, H. Rodríguez-Abella, M. Moreno, and M. A. García-Fernández, “Doppler-derived ejection intraventricular pressure gradients provide a reliable assessment of left ventricular systolic chamber function,” *Circulation*, vol. 112, no. 12, pp. 1771–1779, 2005.

[32] T. Ebbers, L. Wigstrom, A. F. Bolger, J. Engvall, and M. Karlsson, "Estimation of relative cardiovascular pressures using time-resolved three-dimensional phase contrast MRI," *Magnetic Resonance in Medicine*, vol. 45, no. 5, pp. 872–879, 2001.

[33] C. Amador Carrascal, S. Chen, A. Manduca, J. F. Greenleaf, and M. W. Urban, "Improved Shear Wave Group Velocity Estimation Method Based on Spatiotemporal Peak and Thresholding Motion Search," *IEEE Transactions on Ultrasonics, Ferroelectrics, and Frequency Control*, vol. 64, no. 4, pp. 660–668, 2017.

[34] F. Gran, J. Udesen, M. B. Nielsen, and J. A. Jensen, "Coded ultrasound for blood flow estimation using subband processing," *IEEE Transactions on Ultrasonics, Ferroelectrics, and Frequency Control*, vol. 55, no. 10, pp. 2211–2220, 2008.

[35] C. Papadacci, M. Pernot, M. Couade, M. Fink, and M. Tanter, "High-contrast ultrafast imaging of the heart," *IEEE Transactions on Ultrasonics, Ferroelectrics, and Frequency Control*, vol. 61, no. 2, pp. 288–301, 2014.

[36] P. Joos, J. Poree, H. Liebgott, D. Vray, M. Baudet, J. Faurie, F. Tournoux, G. Cloutier, B. Nicolas, and D. Garcia, "High-Frame-Rate Speckle-Tracking Echocardiography," *IEEE Transactions on Ultrasonics, Ferroelectrics, and Frequency Control*, vol. 65, no. 5, pp. 720–728, 2018.

[37] J. Poree, D. Posada, A. Hodzic, F. Tournoux, G. Cloutier, and D. Garcia, "High-Frame-Rate Echocardiography Using Coherent Compounding with Doppler-Based Motion-Compensation," *IEEE Transactions on Medical Imaging*, vol. 35, no. 7, pp. 1647–1657, 2016.